LIMITATIONS FOR DETECTING SMALL-SCALE FAULTS USING THE COHERENCY ANALYSIS OF SEISMIC DATA

A Thesis

by

DAVID BENJAMIN BARNETT

Submitted to the Office of Graduate Studies of
Texas A&M University
in partial fulfillment of the requirements for the degree of

MASTER OF SCIENCE

May 2005

Major Subject: Geophysics

LIMITATIONS FOR DETECTING SMALL-SCALE FAULTS USING THE COHERENCY ANALYSIS OF SEISMIC DATA

A Thesis

by

DAVID BENJAMIN BARNETT

Submitted to Texas A&M University
in partial fulfillment of the requirements
for the degree of

MASTER OF SCIENCE

Approved as to style and content by:

Richard L. Gibson
(Chair of Committee)

Steven Dorobek
(Member)

Akhil Datta-Gupta
(Member)

Richard Carlson
(Head of Department)

May 2005

Major Subject: Geophysics

ABSTRACT

Limitations for Detecting Small-Scale Faults Using the Coherency Analysis of
Seismic Data. (May 2005)
David Benjamin Barnett, B.S., Union College;
M.S., Wright State University
Chair of Advisory Committee: Dr. Richard L. Gibson

Coherency analyzes the trace to trace amplitude similarities recorded by seismic waves. Coherency algorithms have been used to identify the structural or stratigraphic features of an area but the limitations for detecting small-scale features are not known. These limitations become extremely important when interpreting coherency within poorly acquired or processed data sets.

In order to obtain a better understanding of the coherency limitations, various synthetic seismic data sets were created. The sensitivity of the coherency algorithms to variations in wave frequency, signal-to-noise ratio and fault throw was investigated. Correlation between the coherency values of a faulted reflector and the known offset shows that coherency has the ability to detect the presence of various scale features that may be previously thought to be below seismic resolution or difficult to discriminate with conventional interpretation methods.

Coherency values had a smaller standard deviation and were less sensitive to noise when processed with a temporal window length less than one period. A fault could be detected by coherency when the signal-to-noise ratio was >3. A fault could also be detected as long as the throw-to-wavelength ratio was >5% or two-way traveltime-to-period >10%. Therefore, this study suggests that coherency has the ability to detect a fault as long as the frequency of the data imaging that fault has a period no greater than one order of magnitude to the traveltime through the fault and that the signal can easily be distinguished from noise.

Results from application of the coherency analysis were applied to the characterization of a very deep fault and fracture system imaged by a field seismic data set. A series of reverse and strike-slip faults were detected and mapped. Magnitudes of the throws for these faults were not known, but subtle amplitude anomalies in seismic sections confirmed the coherency analysis. The results of this study suggest that coherency has demonstrated an ability to detect features that would normally be overlooked using traditional interpretation methods and has many future implications for poorly imaged seismic areas, such as sub-salt.

To The Boston Red Sox...

ACKNOWLEDGMENTS

I would like to express my sincere gratitude to Dr. Richard Gibson for providing me with guidance and wisdom. His tireless efforts have allowed me to complete my research and have prepared me for the workforce. I would also like to thank Dr. Steven Dorobek for the use of the facilities, guidance and geological knowledge. Also, thank you to Dr. Akhil Datta-Gupta for his aid in understanding the engineering data and his participation on my committee. I appreciate all of the help from the rest of the “Gibson Team;” especially Hung-Liang. If I was not always asking him questions, he probably would have graduated by now.

I am also grateful to Julio Montana at ConocoPhillips for his aid with the Landmark software at A&M which gave me the ability to save, transfer and make my data useful. I would also like to thank Joel Brewer and Max Burton for allowing me the use of the coherency software and Jim Brasher for the use of the field data. Also, thank you to Tony Lupo for “mentoring” me while I was an intern at ConocoPhillips and after as well. I would also like to thank Laura Evins and Paradigm for their coherency class and related efforts.

I would like to thank my family and friends who gave me their support and advice while I was starting, stalling, restarting and finishing my thesis.

Finally this research would not be possible without the unnerving patience, countless encouraging remarks, rides to and from school, meals provided while working, being my “shuzuku” and especially the unwavering love and support from my love, Amber. Thank you for being in my life and keeping my mind clear and driven.

I appreciate everyone that has added to my research and experience here at Texas A&M University. I have enjoyed my time here and will not forget what these past three years have meant to me. Thank you all.

TABLE OF CONTENTS

Page

CHAPTER Page

LIST OF TABLES

TABLE Page

LIST OF FIGURES

FIGURE Page

FIGURE Page

CHAPTER I

INTRODUCTION

A quantitative geophysical analysis of a reservoir can help to optimize the recovery for a given hydrocarbon source. Typically, the integration of core data, production, geological, and geophysical data and well logs are required to complete such an analysis. These data provide detailed information about the reservoir properties and geometrics. Although essential to a quantitative analysis, these data can be expensive to collect and may not exist for a given reservoir. Therefore, understanding the limitations for the available data is essential for accurately modeling the reservoir.

By calculating localized waveform similarity in both the in-line and cross-line directions, we can compute three-dimensional seismic coherence (Bahorich and Farmer, 1995). This coherence cube can then be used to outline seismic discontinuities. The detection of these locally incoherent signals, computed from neighboring traces, helps to outline the structural regime and stratigraphic features of the reservoir. The seismic signal representing a rock on either side of a fault or sedimentary boundary may vary only slightly such that a traditional amplitude time slice may not reveal the feature. Coherency however, tends to indicate lateral discontinuities that might be otherwise overlooked by traditional interpretation methods (Bahorich and Farmer, 1995).

Coherency analyzes seismic reflection data, which record information about the medium through which the waves have propagated. However, the ability to resolve the information recorded by these waves is often difficult to determine. It therefore becomes essential to understand exactly what features are being investigated and at what resolution these features can be imaged.

The use of seismic coherency may be able to detect small-scale variations within the subsurface, such as minor lateral fluctuations, that standard seismic data cannot resolve. Furthermore, the minimum throw at which a fault can be detected is not known. Although large-scale faults (100's of meters of throw) can be detected by

---

This thesis follows the style and format of Geophysics.

seismic waves and traditional interpretation methods, it is more difficult to determine whether information about small-scale faults (10's of meters of throw) such as joints or fractures are real signal or simply noise. Publications to date have not investigated the scale at which faults can be detected but have mentioned that lateral resolution may improve with variations of the original coherency algorithm [(Marfurt et al., 1998) & (Marfurt et al., 1999) & (Gersztenkorn and Marfurt, 1999) & (Marfurt and Lynn, 2000)]. Furthermore, improvements on the vertical resolution of seismic coherency from changes in the signal-to-noise ratio and frequency content have not been investigated.

Several versions of coherency algorithms have been developed for use in seismic reservoir characterization. Specific coherency algorithms are designed for explicit geological settings (e.g., high structural dip) or specific geophysical representations of the data (e.g., low signal-to-noise ratio). Therefore, the minimum offset at which a fault can be detected for each algorithm may vary as the geophysical and geological settings change. The main objective of coherency analysis research is to outline the structural regime and stratigraphic features of the reservoir. This research used two coherency algorithms (Marfurt et al., 1999) to outline the resolution of faults within a controlled synthetic seismic volume. The coherence cube for a 3-D seismic volume of field data was then analyzed using the same technique and compared to the synthetic model results.

ConocoPhillips acquired the seismic data used in this study in 1995. The seismic investigation performed within this study is the first application of the 3-D geophysical data for the Hunton Formation within the study area. The Hunton Formation, which has been under production for many years at the selected oil field, was initially explored using 2-D seismic data. Other available data consist of well logs from seven gas-producing wells and production data. Although there are no core data, some cutting-logs are available.

The driving mechanism for gas production is not known. Cumulative gas and rates of production vary from well to well within the Hunton reservoir. Therefore, it is essential to determine the driving mechanism behind gas production in order to recover the remaining gas in place. The initial investigation of well logs, production and geophysical data suggest that variations within many reservoir parameters are not a critical contributor to gas production. However, it is hypothesized that fracture permeability accounts for the variation of gas production between well locations. Hence, a detailed structural analysis is important to optimize the reservoir's production.

This research used two different coherency algorithms to analyze a set of synthetic data to determine variations of coherence with frequency content, signal-to-noise ratio, and vertical throw. Therefore, the vertical resolution of the coherency algorithms was determined for data with various geophysical properties, allowing for both large-scale and small-scale faults to be accurately mapped. Following the coherency analysis, the structural regime of the Hunton Formation within the field data was investigated to verify the previous results. The data representing the target zone is extremely deep and of inferior quality due to poor processing or acquisition parameters. Therefore, accurate imaging of faults within these geophysical settings provides many implications for other troublesome areas, such as sub-salt targets.

CHAPTER II

REGIONAL GEOLOGY OF THE ANADARKO BASIN

2.1 Location and Structural Boundaries

The Anadarko Basin is one of the deepest sedimentary or structural basin within the North American craton (Johnson, 1989a). It is bounded by the Wichita and Amarillo uplifts to the south, Nemaha uplift to the east and the Cimarron uplift to the west (Figure 2.1). The sedimentary basin, which may contain up to 40,000 feet of Paleozoic rocks in some locations, extends to the ancient shelf margin of the North American Craton in the northern boundary (Blubaugh, 1999). Prior to the onset of major tectonic events in the early Pennsylvanian Period, the area of the Anadarko Basin was part of a broad sea (Johnson, 1989a) containing a calm shelf depositional environment. The passive margin during late-Cambrian to Mississippian time allowed for accumulation of thick carbonate sequences interbedded with shale and sandstone (Figure 2.2). There were also many periods of low sea-level resulting in several prominent unconformities.

Subsequent tectonic events during the Permian resulted in the formation of several deep sedimentary basins (Anadarko, Arkoma and Ardmore Basins). The Anadarko Basin is one of the principal oil and gas producing basins within the North American Craton (Perry, 1987).

2.2 Tectonic History of the Area

The Anadarko Basin has four major periods of development: 1) Precambrian crustal consolidation, 2) Late-Precambrian to Middle-Cambrian aulacogen development, 3) Cambrian through Early-Mississippian development of the southern Oklahoma trough, and 4) Late-Paleozoic tectonism (Perry, 1987). The development of the aulacogen and subsequent tectonism will be the most pertinent to this study.

The earliest stages of rifting are represented by large volumes of igneous intrusions, Early-Cambrian in age. Although this stage of rifting produced a dominant

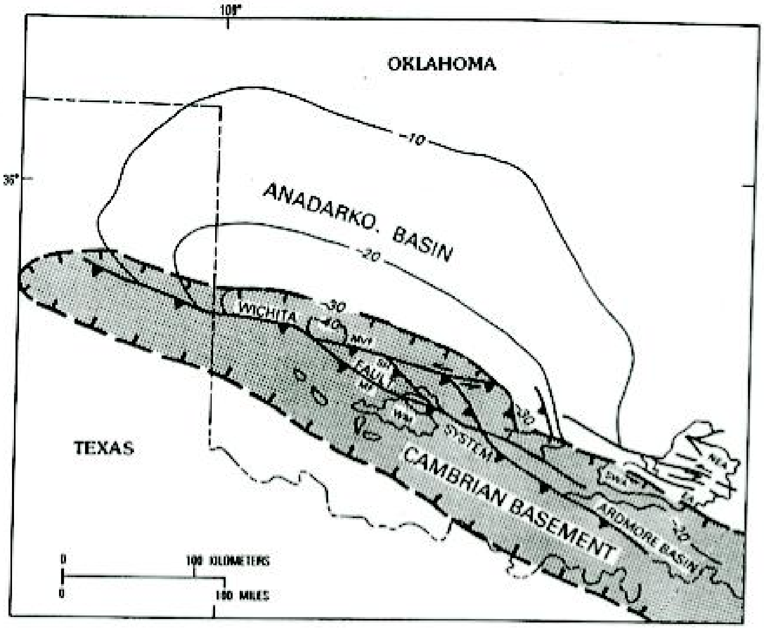

Fig. 2.1. Regional geological map of the present-day Anadarko Basin (Johnson, 1989a).

normal fault system, the rift failed. As a result of the failed rift, the Oklahoma Basin was formed (later to become the Anadarko, Arkoma and Ardmore Basins) signifying the opening of the proto-Atlantic Ocean (Perry, 1987). During the Cambrian to Lower-Devonian Periods, deposition of carbonate sequences occurred over the southern part of the aulacogen.

The basin's basal formation, the Reagan Sandstone, Cambrian in age, represents the beginning of a transgressive sequence. It is overlain by the Lower-Ordovician Arbuckle Group, a series of shallow-water marine limestones and dolomites (Johnson, 1989a). Middle-Upper Ordovician rocks consist of the Simpson Group, a series of sandstones, overlain by the Viola Formation (a limestone sequence) and the Sylvan Shale respectively. These rocks represent a transgressive sequence. Directly overlaying the Sylvan Shale is the Silurian-Devonian Hunton Group. Overlaying the Hunton Group is the organic-rich, Devonian Woodford Shale, which acts as both a source and cap rock for the underlying carbonate reservoir.

The carbonate sequences within the Arbuckle, Viola and Hunton Groups coupled with inter-fingered sandstones and shales of the Reagan, Simpson, Sylvan and Woodford Formations represent paleo-transgressive depositional environments. More than 3 km of sediment were deposited during the Cambrian-Devonian time.

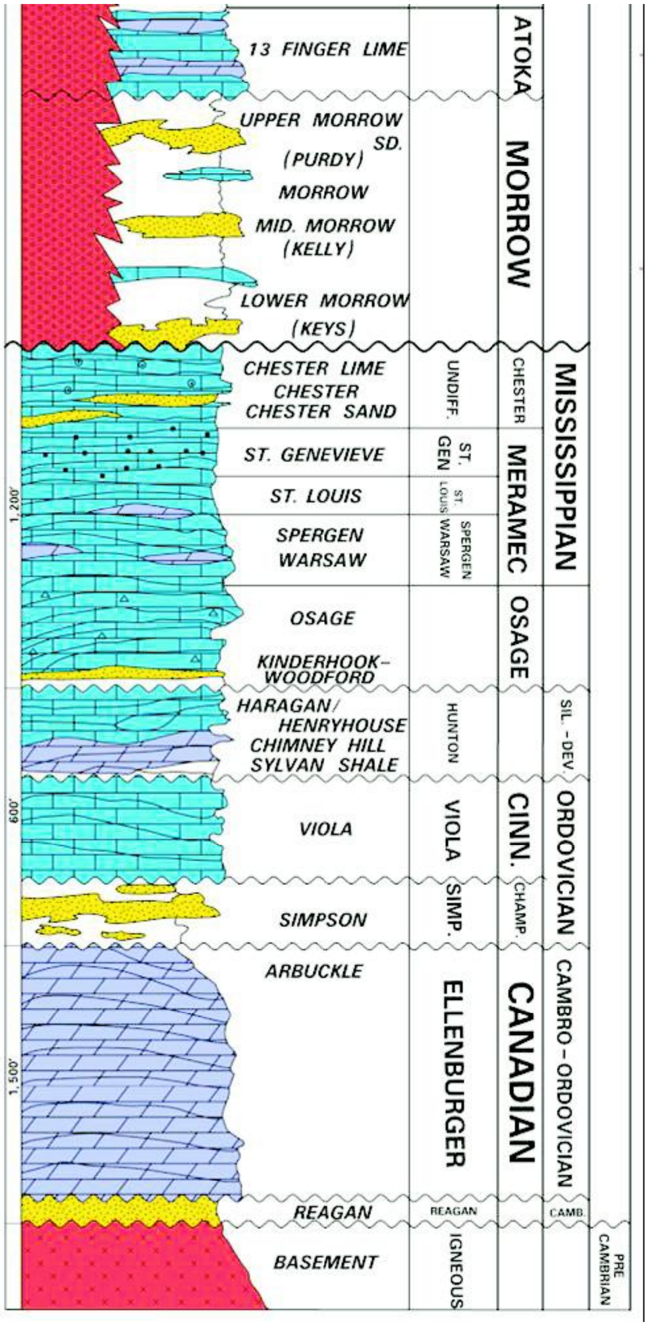

Fig. 2.2. Stratigraphic column for the sediments deposited regionally within the Anadarko Basin (provided by ConocoPhillips Inc.).

During the Devonian Period and throughout the deposition of the Hunton Group, the approaching supercontinent, Gondwanaland forced the passive margin and the carbonate sediments to deepen and form a foreland basin. Throughout the Mississippian, the proto-Anadarko Basin consisted of shallow marine limestones and shales (Johnson, 1989a).

Throughout the Pennsylvanian Period, the approaching landmass forced the aulacogen to uplift and subdivide the Oklahoma Basin into many the basins that are present today (Johnson, 1989a). The collision of the two land-masses uplifted the aulacogen while closing the proto-Atlantic Ocean. It was during this time that the Wichita-Amarillo block uplifted, creating a series of West-Northwest reverse faults (Perry, 1987). By the end of the Devonian Period the carbonate sequence had been extensively faulted and uplifted.

The collision between the North American Craton and Gondwanaland most likely lasted until Early-Permian time while creating predominantly wrench or compressional structural features. Most preset-day faults are typically high-angle with vertical displacement up to 12 km (Johnson, 1989b). The fault patterns vary within the Anadarko Basin but maintain a structural pattern that is concurrent with early Alleghanian orogenic activity in the central Appalachians (Perry, 1987).

2.3 Description of the Hunton Group

Within the Anadarko Basin, the Hunton Group (Figure 2.3) is composed of carbonate strata of Ordovician-Devonian age (Blubaugh, 1999), ranging up to 1300 feet (400 m) in thickness (Morgan, 1982). These strata overlie the Sylvan shale and underlie the Woodford Shale (Amsden, 1975). Although seven main formations make up the Hunton Group, these strata are not preserved everywhere throughout the basin. The Keel, Cochrane, Clarita, Henryhouse, Haragan, Bois dArc, and Frisco Formations (ascending order) are interrupted by two major and many other minor unconformities (Amsden, 1975). The Hunton Group represents an overall shallowing-upward sequence, containing both mudstones and wackestones to packstones and grainstones.

The sequence was most likely deposited within a shallow inland sea during a period of slow transgression caused by the approach of Gondwanaland. The collision of Gondwanaland and the North American Craton caused the Oklahoma Basin to sub-

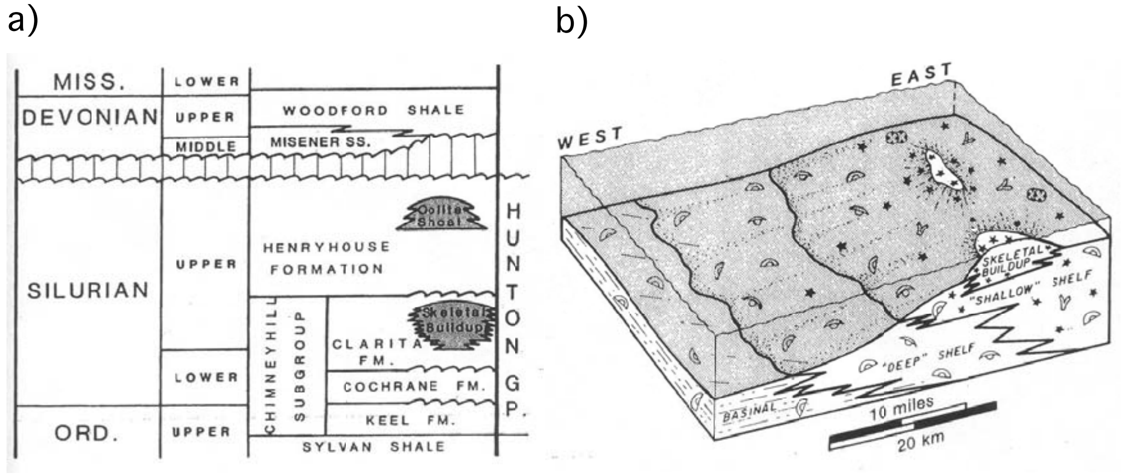

Fig. 2.3. a) Stratigraphic column of the Hunton Group b) Typical depositional setting for the Hunton (Morgan, 1982).

side regionally with isolated uplifted regions (Pippin, 1968). Therefore, stratigraphic sequences were not always preserved due to erosion. The location of the study area for this research is adjacent to such an uplift resulting in an incomplete Hunton Group. Locally, the Hunton contains the Chimney Hill subgroup (Keel, Cochrane, Clarita formations) and the Henryhouse Formation.

2.3.1 Chimney Hill Subgroup

The Chimney Hill Subgroup is mostly composed of three formations: Clarita Formation, Cochrane Formation and the Keel Formation. These formations were deposited primarily on a distally steepened ramp (Morgan, 1982) during a period of regression. The Chimney Hill Subgroup is composed of three main depositional facies: middle shelf, shallow shelf and skeletal buildups.

The Keel Formation is classified as a skeletal wackestone using the Dunham Classification. The skeletal wackestone contains oolites and peloids with both ostracod and trilobite fragments (Morgan, 1982). This formation was most likely deposited within a middle shelf facies, formed in a high energy environment. It also represents the sharp change from the underlying clastic environment to a carbonate setting.

The Keel Formation stratigraphically underlies the Cochrane and Clarita Formations respectively. The Cochrane Formation consists of skeletal packstones. Ostracodes and crinoids are abundant within the skeletal-buildups and are cemented by micrite (Morgan, 1982). This formation was most likely deposited within a shallow shelf, formed in a low-medium energy environment. The Clarita Formation consists of skeletal packstone with local interbedded grainstones. Skeletal-buildups are also abundant. The packstones are dominated by crinoids, arthropods, and extensive dolomitization (Morgan, 1982).

Both the Clarita and Cochrane Formations were deposited within similar environments, however both the lack of abundant micrite within the Clarita Formation and the combination of the packstones, grainstones and skeletal-buildups make it the primary hydrocarbon reservoir rock within the Chimney Hill Subgroup. Porosity varies from 0% to 15% with the highest percentage associated with highly-dolomitized skeletal-buildups (Morgan, 1982).

The presence of dolomite within the matrix of the skeletal-buildups and packstones suggests that the lime mud was replaced. Furthermore, the faunas within the dolomitized and original carbonates are similar, suggesting that dolomitization was a post-depositional, diagenic event (Morgan, 1982). According to core data throughout the Anadarko Basin, dolomitization has not been linked to location within the basin but has been more prevalent in localities with extensive faulting (Amsden, 1975).

The existing porosity network and structural enhancement provided a conduit for the mixing of meteoric and sea waters, thus allowing dolomitization to enhance the original porosity. Four types of porosity are present within the Hunton Group: moldic, vuggy, intercrystalline, and fracture (Blubaugh, 1999). Moldic and intercrystalline porosities are preferential to specific lithologies whereas vuggy and fracture porosities are associated with post-depositional processes. Most porosity within the Hunton Group is vuggy, formed after dolomitization preserved the primary porosity. Locally within the study area, regions of high fracture density correspond to high hydrocarbon production, indicating that the pore network may be dominated by fracture porosity and permeability.

2.3.2 Henryhouse Formation

The Henryhouse Formation contains shallowing-upward shale-carbonate sequences (Al-Shaieb and Puckette, 2001). Most likely deposited within a low-energy sea, the Henryhouse Formation contains many prevalent subaerial exposure surfaces. Therefore, transgression and regression caused lateral migration of the depositional facies to occur along with many periods of erosion.

Although not continuous throughout the Anadarko Basin, the Henryhouse Formation contains three main depositional facies: subtidal, intertidal, and supratidal. These facies are indicative of a shallowing upward trend. The subtidal facies, representing the oldest depositional facies within the Henryhouse Formation, consists of dolomitic mudstone and wackestone (Morgan, 1982). The dominant fauna are brachiopods, trilobites, ostracodes, bryozoans and echinoderms, suggesting a low-medium energy, shallow open-water depositional environment most likely below the wave base (Al-Shaieb and Puckette, 2001).

The intertidal facies, which overlie the subtidal facies, are composed primarily of dolomitized wackestones with significant porosity. The facies also contains some oolitic-grainstone shoals and peloids-rich mudstones. Other components of the facies are oncolites and crinoids (Morgan, 1982). The variety of lithologies within this facies indicates that the depositional environment is not laterally continuous and ranges from a shallow, low-energy lagoon to high-energy oolitic shoals. The compositional make-up of the oolitic shoals makes these facies the most prolific hydrocarbon producer within the Henryhouse Formation.

The supratidal facies, which was last within the sequence, overlie the intertidal facies. The facies was deposited most likely within a restricted shallow environment, such as a tidal flat, either at or near mean high tide (Al-Shaieb and Puckette, 2001). The facies consist of dolomitized mudstones with cryptal algal fabrics. This facies is massive and highly dolomitized with irregular laminations and few fauna or trace fossils present (Morgan, 1982).

The supratidal facies contains low porosity (0-4%) with fine-grained mud and few fossils (Blubaugh, 1999). The subtidal facies contains a diverse fossil assemblage and some hemi-pelagic mud, and has low porosity (0-4%). The intertidal facies however has good porosity ranges (5-10%), provided by an abundance of fossils and coarser grained material (Blubaugh, 1999). Although dolomitization has been linked to porosity (Al-Shaieb and Puckette, 2001), the type of depositional facies also has a strong influence. The presence of bioturbation and burrowing has added to the primary porosity. Regionally, the Henryhouse Formation has been a prolific hydrocarbon producer; however, it has been almost completely eroded away locally within the study area.

2.4 Reservoir Characteristics and Production

Within the study area, the Hunton Group ranges in thickness from 400-700 feet at a depth range of 18,000-24,000 feet below the surface elevation. The region is dominated by a series of high angle reverse faults, with major vertical offsets ranging from 800-1,200 feet and strike-slip faults with major vertical offsets ranging from 100-200 feet. Positioned within the structural regime are 11 hydrocarbon-producing wells (Figure 2.4). The life-span of these wells ranges from two to thirty years while producing more than 460 billion cubic feet of gas for the entire field. Although some wells have been more productive than others, all of the wells fall along the same pressure/formation factor vs. cumulative production curve (Figure 2.5). Therefore, each well is in communication with each other and pumping from the same reservoir.

Relationships of pay thickness, gross thickness, water saturation, porosity (primary) and porosity-feet vs. production (Figure 2.6) did not show a strong correlation between the wells that produced either a large or small quantity of gas. Therefore, the measured reservoir properties do not correspond to production variations. Fracture related properties (porosity and permeability) have been identified as the possible driving mechanism behind production. The most prolific gas-producing well is located on the limb of the structural high and at the intersection of a reverse and strike-slip fault. Therefore, a detailed analysis of the large-scale and small-scale fracture network is applied to gain a better characterization and description of the reservoir in order to maximize the future hydrocarbon production.

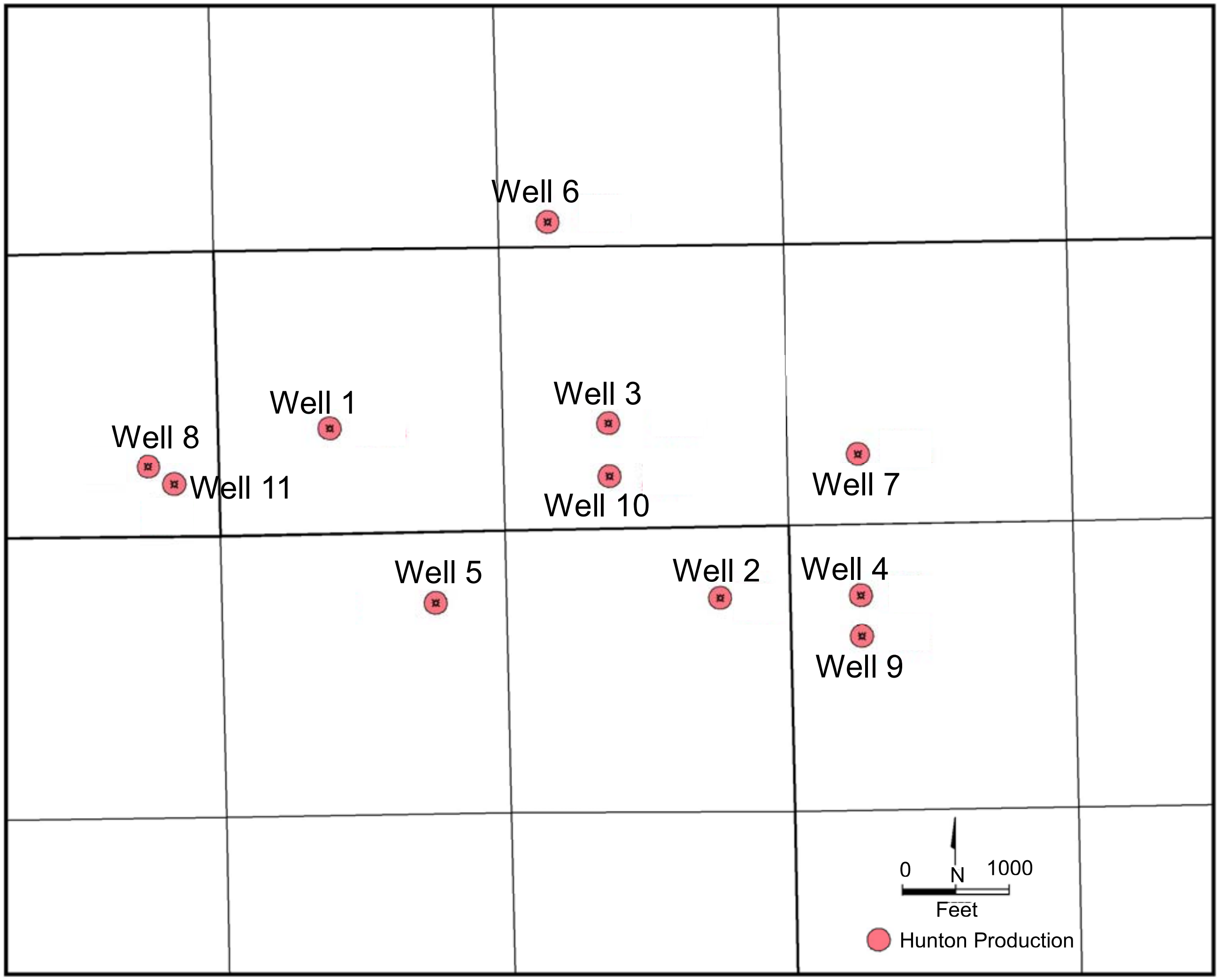

Fig. 2.4. Production map of the study area. The cumulative production and date of last production are labeled next to each well.

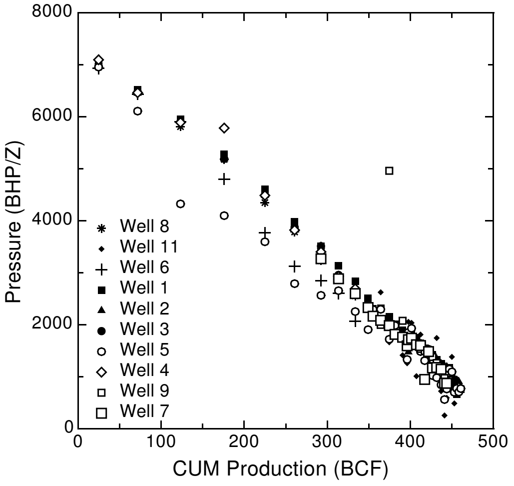

Fig. 2.5. Bottom-hole pressure curve for each well within the same reservoir.

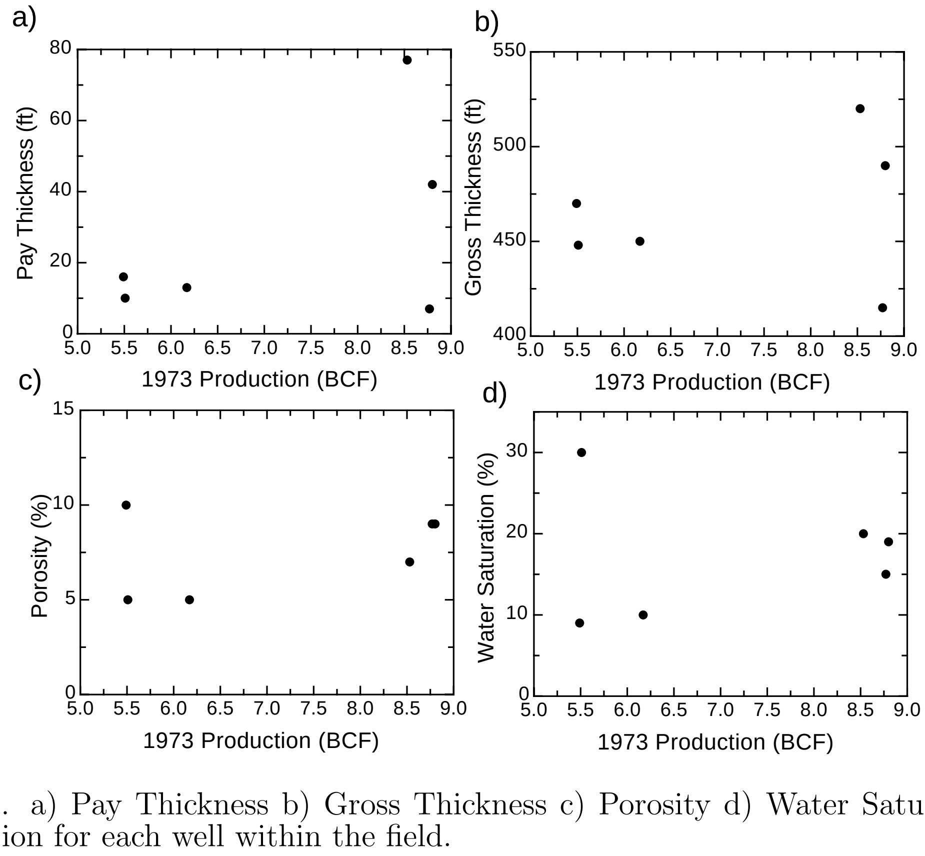

Fig. 2.6. a) Pay Thickness b) Gross Thickness c) Porosity d) Water Saturation vs production for each well within the field.

CHAPTER III

COHERENCY

Many seismic methods and attributes have been used to delineate fractures. Azimuthal velocity analyses (Neves et al., 2003), S/P wave velocity ratios (Li et al., 2003), instantaneous phase (Shen et al., 2002), instantaneous frequency (Shen et al., 2002) and coherency (Bahorich and Farmer, 1995) are all methods currently used to identify fractures. Seismic coherency can extract information about the structural and stratigraphic features recorded within a 3-D seismic data volume without any prior interpretation. Although other seismic attribute applications have been proven to identify faults, the easy detection of faults by seismic coherency without interpretation bias has led to it becoming one of the standard applications by the oil industry for delineating faults. Continuous seismic reflections will produce high coherency values, whereas reflectors containing faults or fractured areas will display low coherency values (Lawrence, 1988).

Incoherent seismic events are strongest when fractures and stratigraphic changes are recorded by seismic waves in the subsurface. Many algorithms have been developed to obtain coherence from such seismic data. The initial coherency algorithm was based on the classical normalized cross-correlation (Bahorich and Farmer, 1995). Advanced methods have used the semblance and more recently, eigenstructures to calculate seismic coherency. Variations of the three major coherency algorithms exist but are used in select situations to reduce interpretive bias or combine other seismic attributes in order to emphasize specific stratigraphic (Peyton et al., 1998), lithologic (Skirius et al., 1999) or fluid changes (Wigger et al., 1997). To date, the semblance and eigenstructure algorithms are the most effective at delineating the structural regime within a seismic volume. Variations in the signal-to-noise ratio, frequency content, and apparent dip of seismic data have led to the continuing research and development of current and new coherency methods.

3.1 Cross-Correlation “C1” Algorithm

The original coherency algorithm (C1) calculates waveform similarities by applying a cross-correlation of three adjacent traces in both the inline and crossline directions (Bahorich and Farmer, 1995). Seismic traces on opposite sides of a fault will generally have a different signature. Therefore, the time-difference between the start time and the time of the maximum value of the cross-correlation is a measure of the time shift across the fault. By comparing three or more traces side by side, a high spatial resolution of lateral changes in geology is illustrated by seismic coherency (Marfurt and Lynn, 2000).

The cross-correlation, ρ_x, at time t between data traces u at positions (x_i, y_i) and (x_{i+1}, y_i) can be expressed as:

$$\rho_x(t, l, x_i, y_i) = \frac{\sum\limits_{\tau=-w}^{w} u(t-\tau, x_i, y_i)u(t-\tau-l, x_{i+1}, y_i)}{\sqrt{\sum\limits_{\tau=-w}^{w} u^2(t-\tau, x_i, y_i) \sum\limits_{\tau=-w}^{w} u^2(t-\tau-l, x_{i+1}, y_i)}} \tag{3.1}$$

where $2w$ is the cross-correlation window length (Marfurt et al., 1998). Equation 3.1 can be varied slightly to work in both the x and y directions. These correlation coefficients can be combined to create a 3-D estimate of coherency ρ_{xy}:

$$\rho_{xy} = \sqrt{[max_l \rho_x(t, l, x_i, y_i)][max_m \rho_y(t, m, x_i, y_i)]} \tag{3.2}$$

where $max_l \rho_x(t, l, x_i, y_i)$ and $max_m \rho_y(t, m, x_i, y_i)$ represent the lags l and m for maximum ρ_x and ρ_y values. These lags approximate apparent time dip per trace (Marfurt et al., 1998). The analysis of only two traces within equation 3.2 limits the accuracy of analyzing these dips. Therefore, coherency will tend to be limited to applications within high signal-to-noise data sets.

The C1 algorithm used a normalized cross-correlation to determine the maximum time lag for a zero-mean seismic signal (Marfurt et al., 1998). To satisfy the assumption that each signal has a zero-mean, the temporal window length must include the entire wavelength. For low frequency data, the temporal window could be hundreds of milliseconds long, possibly mixing stratigraphic boundaries at different depths. Initial coherency outputs were calculated using a two by two covariance matrix; therefore, effectiveness was limited to data sets with a high signal-to-noise ratio. To compensate for the problems with the cross-correlation algorithm, the "C2" coherency algorithm was created to handle more robust measures of coherency, dip, azimuth and noise (Marfurt et al., 1998).

3.2 Semblance "C2" Algorithm

The first coherency algorithm proved successful at identifying lateral discontinuities within the seismic data, however, noisy data proved problematic. The semblance algorithm (C2) allows for a higher percentage of the signal to be analyzed and is therefore better than the C1 algorithm for noisy data. Semblance, defined by Sheriff and Geldart (1995), is the energy of the stack normalized by the mean energy of the components of the stack (Figure 3.1). The semblance algorithm allows for an increased number of traces to be included within the calculation and also allows for a smaller temporal window to be employed. Thus, the semblance coherency improves the vertical and lateral resolution over the original cross-correlation algorithm.

Although superior to the cross-correlation coherency, the semblance algorithm requires initial geological input prior to calculating the coherency. An initial maximum apparent dip, d_{max}, is calculated by the interpreter from the field data and used by the algorithm to compute the coherency (Marfurt et al., 1999).

$$d_{max} \leq \sqrt{p^2 + q^2} \tag{3.3}$$

In equation 3.3, p and q are associated with the local dip and azimuth of a hypothetical planar reflection event. This incorporation of the apparent dip allows for the coherency to be determined along various test dip/azimuth pairs to determine the best-fit dip/azimuth for each set of traces, resulting with a higher lateral and angular resolution. Furthermore, the input data is de-sampled to 1 msec intervals for increased resolution and to protect from aliasing. The semblance coherency C2 can be expressed as:

$$C2(\tau, p, q) = \frac{\sum\limits_{k=-K}^{K} \left\{ \left[\sum\limits_{j=1}^{J} u(\tau + k\Delta t - px_j - qy_j) \right]^2 + \left[\sum\limits_{j=1}^{J} u^H(\tau + k\Delta t - px_j - qy_j) \right]^2 \right\}}{J \sum\limits_{k=-K}^{K} \sum\limits_{j=1}^{J} \{ [u(\tau + k\Delta t - px_j - qy_j)]^2 + [u^H(\tau + k\Delta t - px_j - qy_j)]^2 \}} \tag{3.4}$$

where $2w$ (half height, $K = w/\Delta t$) is the cross-correlation window length; Δt is the sample increment and u^H is the quadrature component of the seismic trace u (Marfurt et al., 1998). This semblance algorithm computes coherency values with

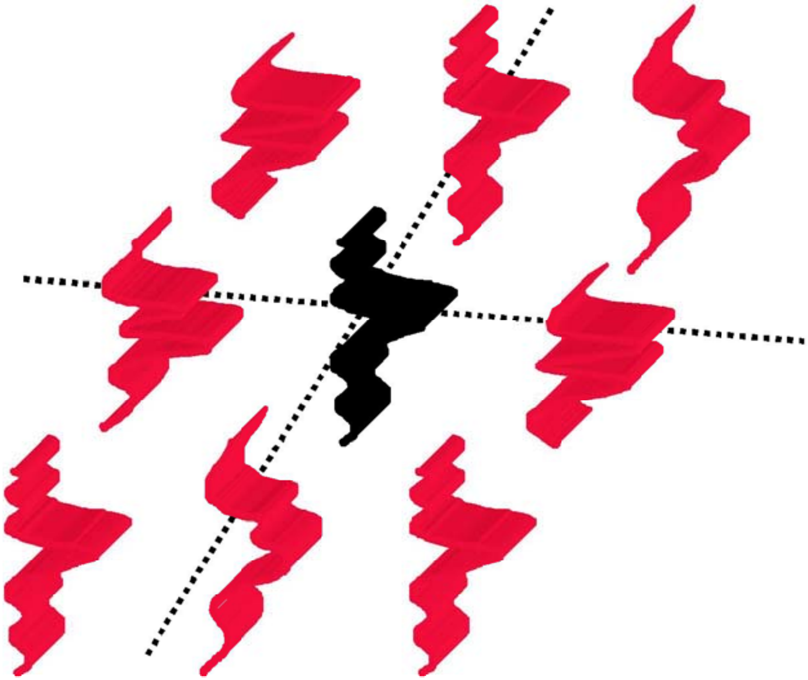

Fig. 3.1. Illustration of traces input into the semblance algorithm. The stack of the energy within the window is divided by the energy of the center trace (provided by Paradigm Geophysical).

increased signal-to-noise ratio and better vertical and lateral resolution than the cross-correlation method. Furthermore, with initial estimates of dip and azimuth, the coherency from the C2 algorithm is computed with a geological advantage over the C1 algorithm's output.

3.3 Eigenstructure "C3" Algorithm

Unlike the C2 coherency algorithm, the C3 algorithm is generated by calculating the eigenstructure of the covariance matrix rather than select dip/azimuth pair from the matrix (Marfurt et al., 1999). The matrix D represents a multichannel time series of the data within the analysis window (Gersztenkorn and Marfurt, 1999):

$$D = \begin{pmatrix} d_{11} & \cdots & d_{1J} \\ \vdots & \ddots & \vdots \\ d_{N1} & \cdots & d_{NJ} \end{pmatrix} \tag{3.5}$$

The argument d_{nj} is the amplitude of the nth sample in the jth trace. The covariance matrix is derived from the time series D and is a sum of the matrices for each time sample within the temporal window (Gersztenkorn and Marfurt, 1999). The covariance matrix C is defined as:

$$C = D^T D \tag{3.6}$$

The C3 algorithm is theoretically superior to the C2 algorithm because it calculates coherency along the eigenstructures for a set of amplitude values cross-plotted sample by sample on a Cartesian coordinate system (Figure 3.2). Figure 3.2 shows the relationship of the covariance matrix to the eigenstructures. Therefore, the cross-plotted amplitude values can be expressed as a set of vectors rather than points, thus limiting the influence of noise or other outlying data points on the coherency calculations. The orientation (eigenvector) and magnitude (eigenvalue) of the major and minor axes of the eigenstructures mathematically describe the covariance matrix and are measures of the geometry and coherency of the input traces (Marfurt et al., 1999). Eigenstructure coherency eliminates noise from the coherency calculation when the signal exceeds the level of additive Gaussian noise (Marfurt et al., 1999).

Noise is typically not Gaussian and therefore can not be completely eliminated from field data. In such situations, the signal-to-noise ratio will tend to have less influence on the eigenstructure coherency because the orientation and magnitude of the dominant vector is a measure of principle direction of the covariance matrix, and is therefore influenced less by the variations due to noise for each cross-plotted amplitude value. The eigenstructure coherence C3 as defined by Gersztenkorn and Marfurt (1999) can be expressed as:

$$C_3(p,q) = \frac{\lambda_1}{\sum\limits_{j=1}^{J} \lambda_j} \tag{3.7}$$

where λ_j is the j_{th} eigenvalue of the covariance matrix C_3.

The difference between the semblance and eigenstructure coherencies can be understood by defining the semblance expression in terms of the covariance matrix (Equation 3.6). Coherence calculations by semblance (in terms of the covariance matrix) uses a normalized, linear combination of all the eigenvectors, u (Equation 3.8) whereas the eigenstructure coherency is associated to the largest eigenvalue of

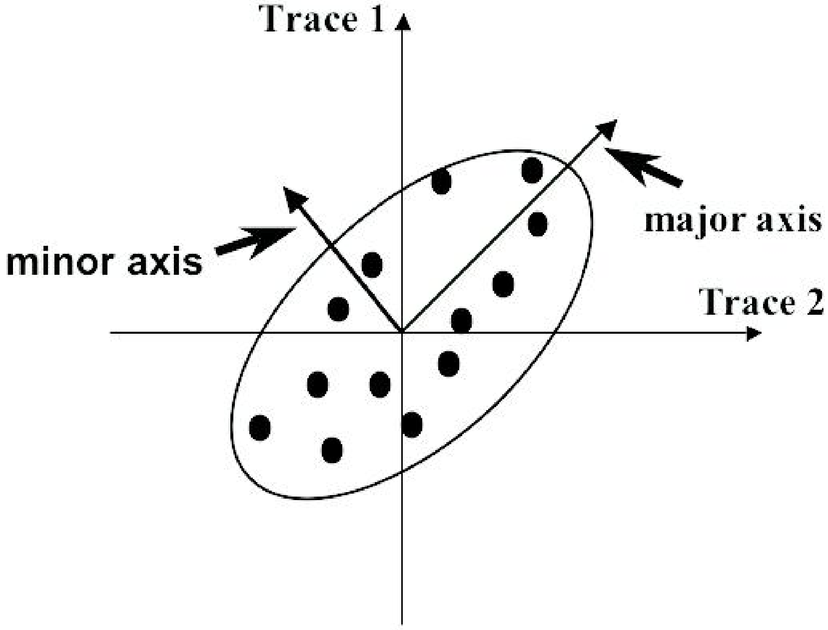

Fig. 3.2. Crossplot on a Cartesian coordinate system of amplitude values at associated times for each input trace within the eigenstructure coherency temporal window (provided by Paradigm Geophysical).

the covariance matrix.

$$u = \frac{1}{\sqrt{J}} \begin{bmatrix} 1 \\ 1 \\ \vdots \\ 1 \end{bmatrix} \tag{3.8}$$

The eigenvector of the covariance matrix will change as the processing window moves throughout the 3-D volume while the semblance vector, u, is normalized and will be static throughout the seismic volume. Therefore, coherence is calculated in different subspaces for the semblance and eigensturcture algorithms (Gersztenkorn and Marfurt, 1999), resulting with a better approximation of the coherency for data sets with low signal-to-noise ratios using the eigenstructure coherency algorithm.

Coherency output is normalized from 0 to 1 with 1 being complete coherence to 0 being complete incoherence. The coherence values are mapped as shades of gray with the darker shades corresponding to locations of low coherence. Linear discontinuities present on both map and vertical sections can be interpreted as faults.

CHAPTER IV

COHERENCY TESTS ON THE SYNTHETIC SEISMIC SECTIONS

The coherency algorithms can be used to identify and map faults of various scales within a seismic volume. It is also important to estimate the resolution of detectable fractures by the coherence algorithms, as this will control the scale to which we can resolve the detailed fracture and fault structures of the reservoir. Therefore, detecting the presence of faults, fractures, joints and the scale to which they can be mapped were investigated. Synthetic seismic models with known geophysical and geological properties were created to determine the sensitivity of coherency to signal-to-noise ratio, frequency content and fault throw.

4.1 Methods

The ability of the coherency algorithms to resolve faults was tested by creating a suite of test models with a specified velocity, density and depth structure. Approximately nine hundred models with a linear and vertical fault penetrating both a strong and a weak reflector were made by adjusting the fault throw, frequency content and signal-to-noise ratio. The variations of these properties were made according to typical geological and geophysical environments.

The geophysical model consisted of five layers separated by four planar reflections with zero dip (Figure 4.1). The uppermost layer at a depth range of 0-2000 m had a Vp, Vs and ρ of 3000 m/s, 1700 m/s and 2.7 gm/cm^3. The second layer at a depth range of 2000-3000 m had a Vp, Vs and ρ of 3300 m/s, 1750 m/s and 2.75 gm/cm^3. The third layer at a depth range of 3000-4000 m had a Vp, Vs and ρ of 3500 m/s, 1800 m/s and 2.8 gm/cm^3. The fourth layer at a depth range of 4000-5000 m had a Vp, Vs and ρ of 3550 m/s, 1850 m/s and 2.85 gm/cm^3. The fifth layer (half-space) had a Vp, Vs and ρ of 3600 m/s, 1900 m/s and 2.9 gm/cm^3. The faults were created within the second and third seismic- interfaces by adjusting the layer depths by 1, 5, 10, 20, 50 and 100 m.

The synthetic seismic data sets were created by copying a zero-offset trace from the five-layer model (Figure 4.2). A second zero-offset trace was created from a

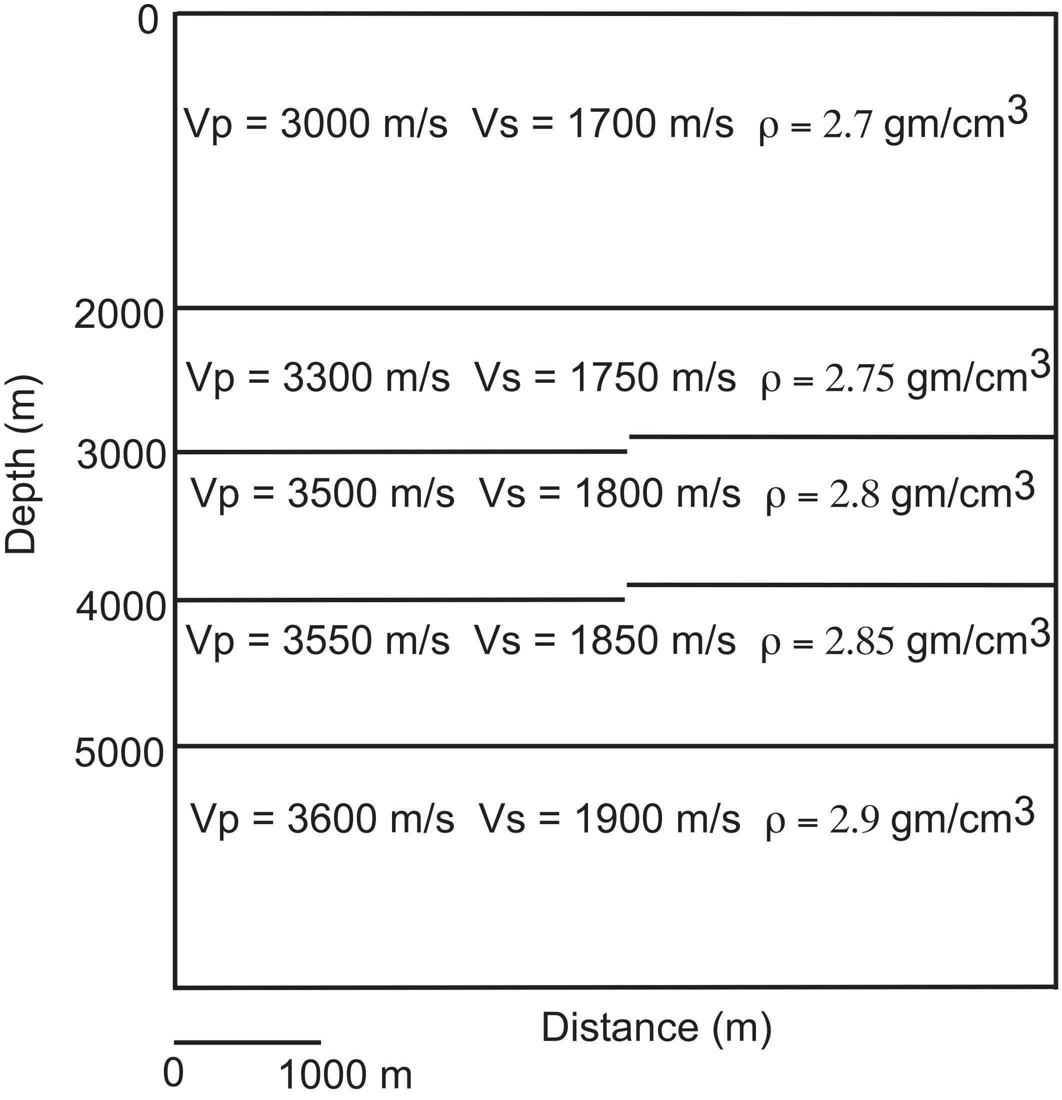

Fig. 4.1. Seismic model used to generate the synthetic models. The models consist of 4 horizontal reflectors with the middle 2 truncated at the center trace locations by a vertical fault.

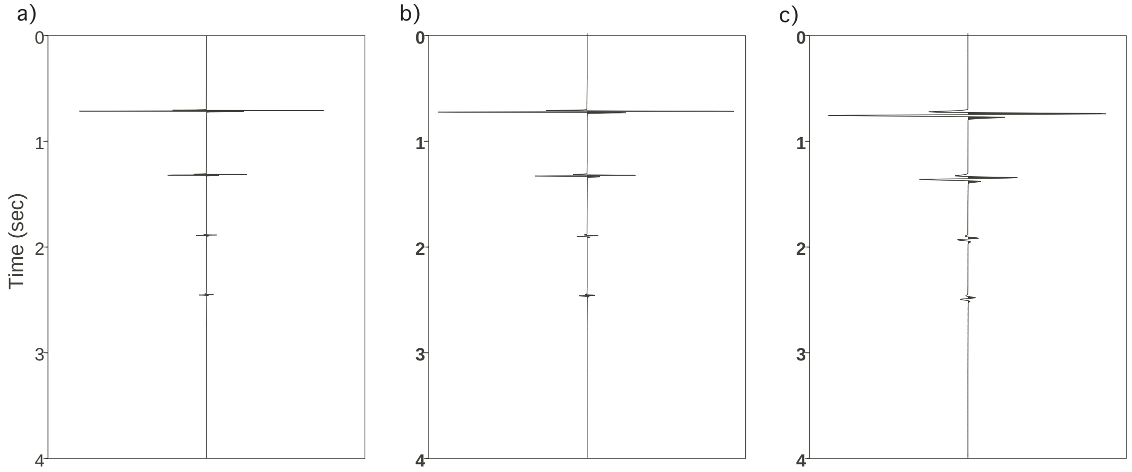

Fig. 4.2. Zero-offset traces generated from an a) 80 Hz b) 50 Hz c) 20 Hz wave that propagated through the seismic model.

geophysically identical model except for variations of the depth to the second and third reflectors. Each trace was copied and merged together into a 2-D line, creating an image of a vertical fault that offset the second and third reflectors. Then this line was copied and merged together to create a 2.5-D synthetic seismic section with a vertical fault. The data sets consist of a 2-D line copied in a third dimension, creating a vertical fault that has a linear orientation. The models are considered to be 2.5-D because the the structure is 2-D, though wave propagation is in principle in 3-D.

The synthetic seismograms were generated for a Ricker wavelet with a center frequency of 20 Hz, 50 Hz, or 80 Hz for each geological model (Figure 4.2). A detailed derivation of the equations used to generate the wavelets is described by Mandal and Mitchel (1986). Furthermore, a signal-to-noise ratio of 10 and 100 (of the highest amplitude reflector) was applied to each model (Figures 4.3 & 4.4). Gaussian noise with a maximum amplitude at either 10% or 1% of the highest amplitude reflector within the model was input into the models. The signal-to-noise ratio for that reflector was either 10 or 100. Other reflectors will have different signal-to-noise ratios due to the variations in the geophysical parameters previously outlined. The resulting signal-to-noise ratios were computed by comparing the maximum additive noise to the amplitude of each reflector and can be found in Table 4.1.

The coherency for each geophysical model was computed using both the semblance and eigenstructure algorithms. Both algorithms required a spatial sampling and temporal window length parameter. For simplicity, the spatial sampling remained

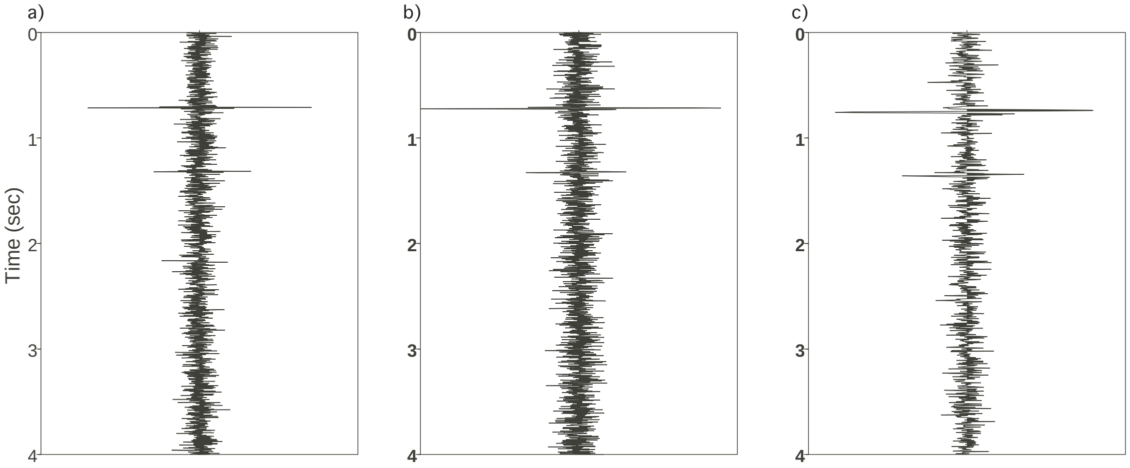

Fig. 4.3. a) 80 Hz zero-offset trace b) 50 Hz zero-offset trace c) 20 Hz zero-offset trace with an input signal-to-noise ratio of 10.

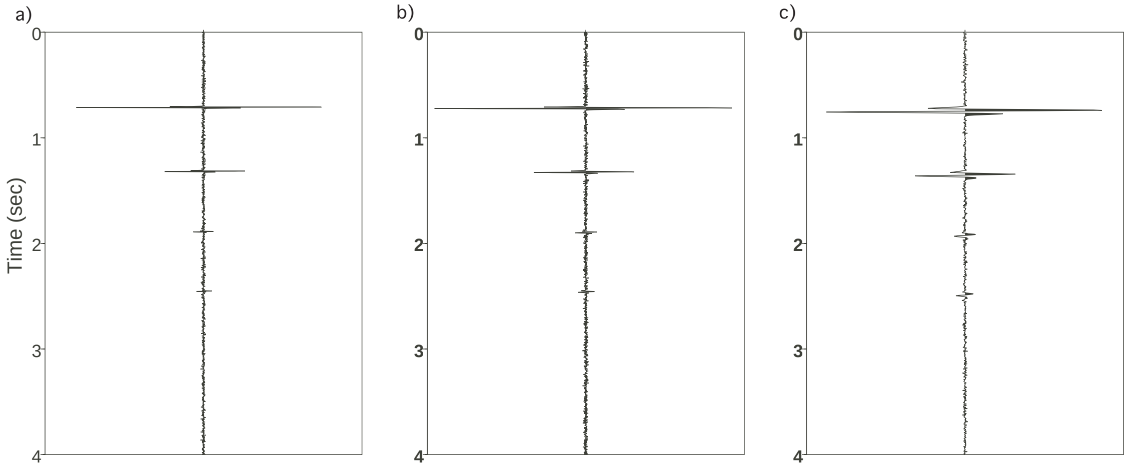

Fig. 4.4. a) 80 Hz zero-offset trace b) 50 Hz zero-offset trace c) 20 Hz zero-offset trace with an input signal-to-noise ratio of 100.

Table 4.1. Estimated signal-to-noise ratios for the strongest amplitude reflector (1), faulted reflectors (2 & 3) and weakest reflector (4). The input noise was either 10% or 1% of the reflector with the strongest amplitude. The resulting ratios are a comparison of the input noise to the reflector amplitude.

Reflector	20 Hz		50 Hz		80 Hz	
1	10	100	10	100	10	100
2	3.55	35.5	3.23	32.3	3.18	31.8
3	0.76	7.6	0.74	7.4	0.82	8.2
4	0.54	5.4	0.54	5.4	0.34	3.4

constant at a five trace increment, while the temporal window length varied by intervals of half of a period (T). Therefore, the vertical offset of the fault, rather than the lateral resolution, will be emphasized within the coherency analysis.

The coherency models were then analyzed along time slices to view how the coherency of the fault changes with depth. To better emphasize the details of the coherency, an extraction of the coherency values along a line within three specific time slices for each model were analyzed. These time slices were selected through the peaks of the strong and weak reflectors and a noise-dominated location (Figure 4.5). Coherency values range from zero to one with one being complete coherency and zero being complete incoherency. Linear extractions of coherency along lines perpendicular to the fault were compared in order to identify the signature of the fault and of noise in order to determine the affects of noise on the coherency along different amplitude reflectors for various frequencies.

The work was completed using several software programs. Initially, the synthetic data set was created using Seismic UNIX (SU). The synthetic data were analyzed using the licensed coherency algorithms outlined by Marfurt et al. (1999) and currently owned by Paradigm Geophysical. The coherency data were then imported into Seisworks, a Landmark product for interpretation.

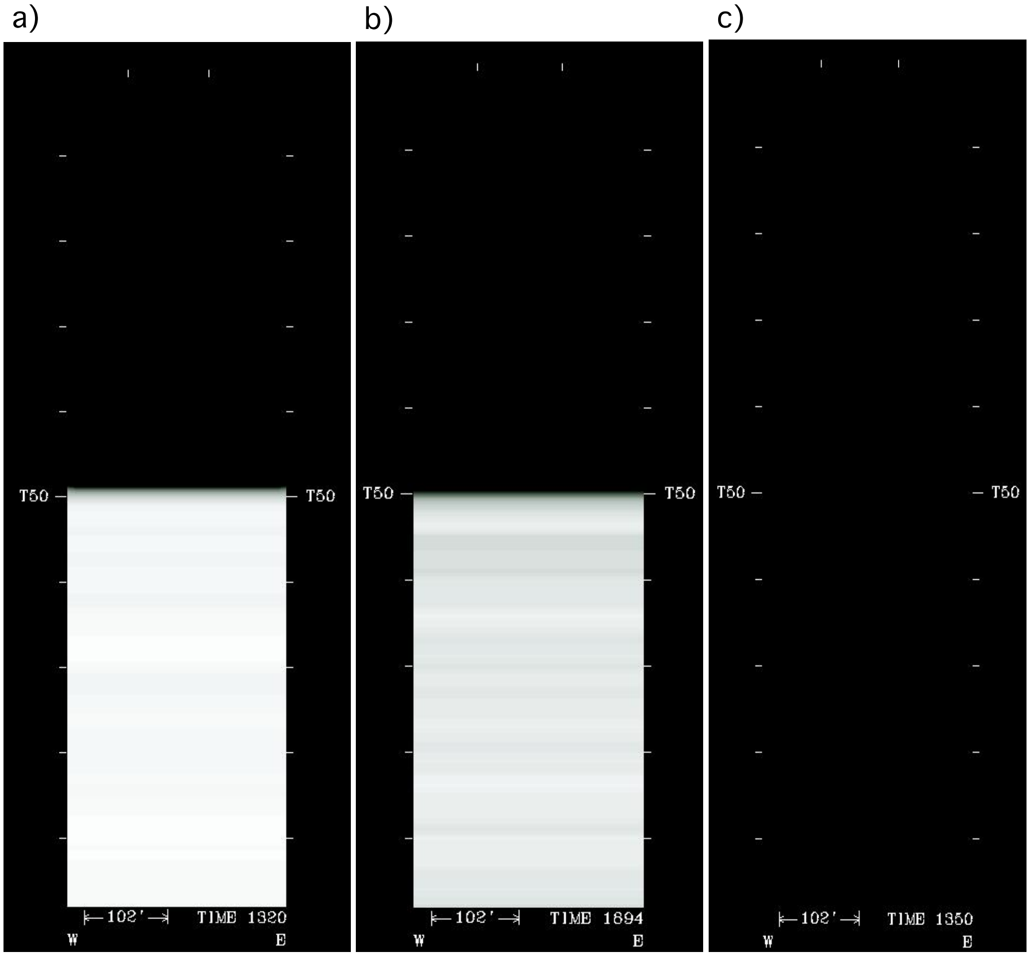

Fig. 4.5. 80 Hz Eigenstructure coherency time-slices a) 1320 ms: s/n=35 b) 1894 ms: s/n=8 c) 1350 ms: s/n<1.

4.2 Results and Interpretation

The application of the semblance and eigenstructure coherency algorithms to the synthetic seismic data sets illustrated the sensitivity of coherency upon variations in frequency content, signal-to-noise ratio and fault throw. The coherency values were also sensitive to the length of the processing temporal window. Through a comparison of these geophysical and geological parameters, the limits to which coherency can image faults within synthetic data were identified.

4.2.1 Temporal Window Analysis

Once the synthetic models were created, the only variables remaining were within the processing of the coherency algorithm. To concentrate on vertical resolution, the spatial sampling parameter remained constant (5 traces) for each simulation. Therefore, the temporal window length was the only parameter to vary. This was done to determine which window length would yield the most distinctive coherency difference with variation of the fault's throw while not decreasing the coherency of the reflector itself.

Direct comparisons of seismic traces near the faults in the models provide important insights into the results of the coherency analysis by illustrating the similarities in waveforms and the influence of noise. To this end, Figure 4.6b shows five traces surrounding the 5 m fault, within the 80 Hz model with an input signal-to-noise ratio of 10. Similarly, the five traces immediately adjacent to the left and to the right were also overlaid (Figure 4.6a & 4.6c). The overlay of traces was similarly completed for the model with an input signal-to-noise ratio of 100 (Figure 4.7) and repeated for the 50 Hz (Figures 4.8 & 4.9) and 20 Hz (Figures 4.10 & 4.11) models. The variations of the overlaid traces will be a result of either the fault or attenuation due to noise.

These overlays indicate that a lateral and vertical amplitude variation exists across the fault, which is more noticeable for the higher frequency models. As expected, noise will interfere with the signal amplitude thus making the distinction between noise and faulted reflectors difficult when the signal is weak. Therefore, determining the appropriate temporal window length is important in limiting the influence of noise on the coherency calculations. This will allow for the distinction between coherent noise and signal or incoherent noise and a fault to be more evident.

The temporal window length was set to several multiples of the period (T) of the

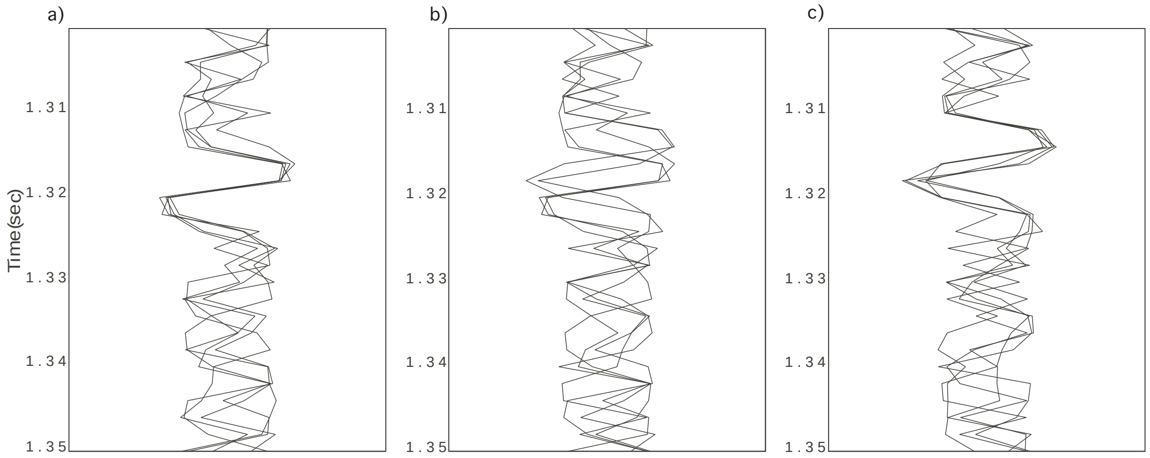

Fig. 4.6. a) 5-trace overlay to the left of the fault b) across the fault c) to the right of the fault for the 80 Hz wave with an input s/n=10.

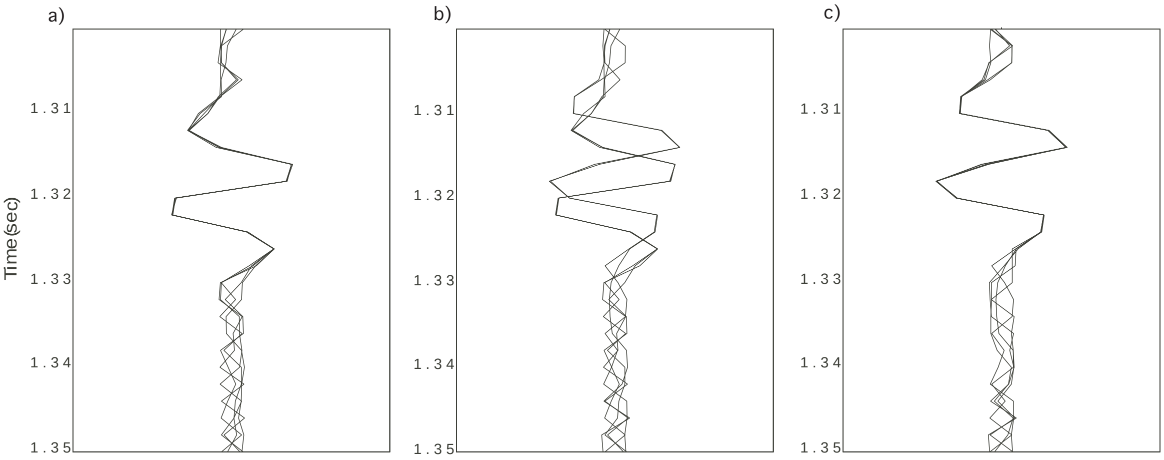

Fig. 4.7. a) 5-trace overlay to the left of the fault b) across the fault c) to the right of the fault for the 80 Hz wave with an input s/n=100.

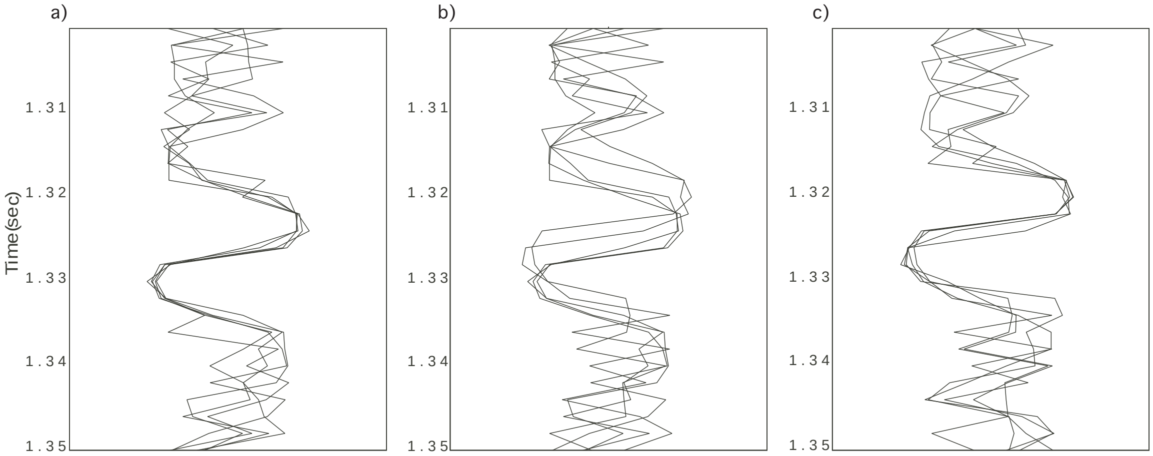

Fig. 4.8. a) 5-trace overlay to the left of the fault b) across the fault c) to the right of the fault for the 50 Hz wave with an input s/n=10.

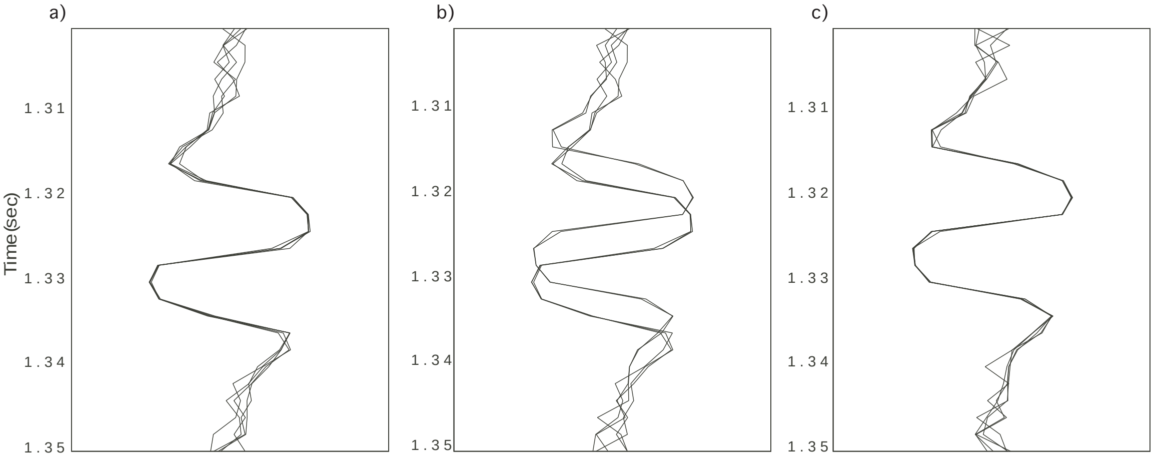

Fig. 4.9. a) 5-trace overlay to the left of the fault b) across the fault c) to the right of the fault for the 50 Hz wave with an input s/n=100.

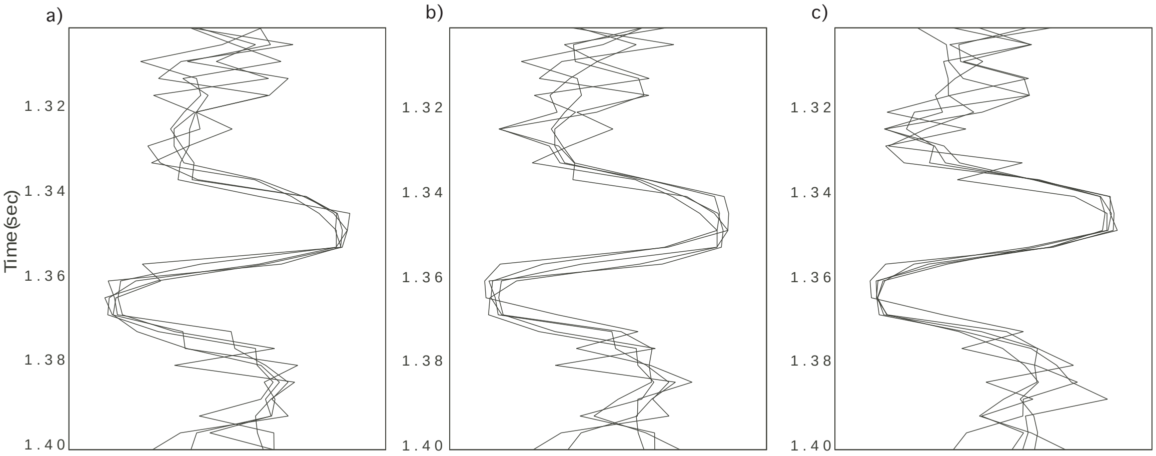

Fig. 4.10. a) 5-trace overlay to the left of the fault b) across the fault c) to the right of the fault for the 20 Hz wave with an input s/n=10.

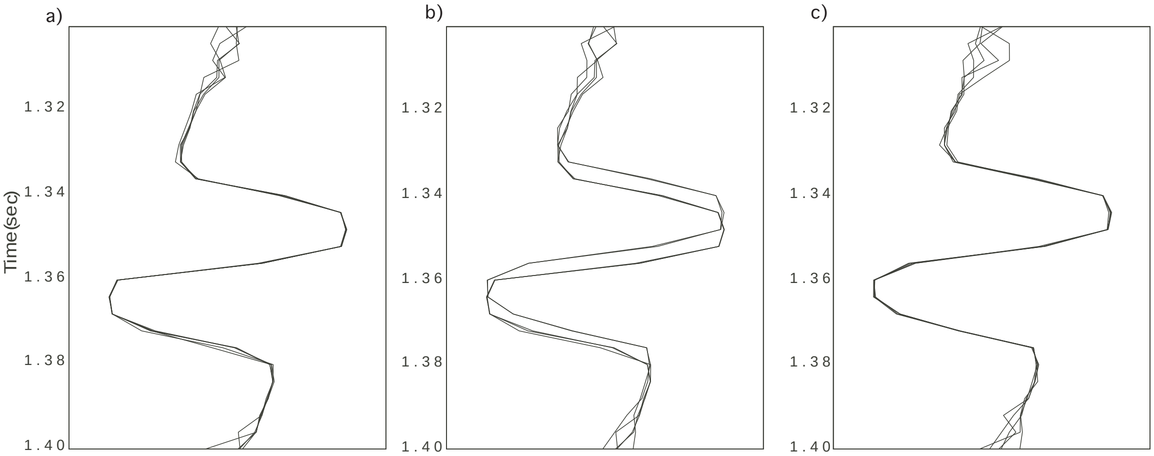

Fig. 4.11. a) 5-trace overlay to the left of the fault b) across the fault c) to the right of the fault for the 20 Hz wave with an input s/n=100.

wavelet (Δt, 0.5T, T, 1.5T, 2T and 3T) and was applied in the same way to both the semblance and eigenstructure algorithms upon the 80 Hz, 50 Hz and 20 Hz frequency models. A linear extraction of the coherency values along three specific time slices is shown for the 80 Hz (Figure 4.12), 50 Hz (Figure 4.13), and 20 Hz (Figure 4.14) models for the models with the input signal-to-noise ratio of 100.

Marfurt et al. (1999) showed that through an increase in the temporal window length of the coherency analysis on field seismic data, an increase in coherency can be obtained. In this case, the influence of noise on coherency was lessened. Marfurt et al. (1999) did not relate the temporal window length to the period of the signal or specify how sensitive coherency is to the signal-to-noise ratio. The results by Marfurt et al. (1999) are valid for a data set with a high signal-to-noise ratio; therefore, when the signal-to-noise ratio is low, an increased window length will allow for the noise to influence the coherency calculations more than with a smaller window. Through a comparison of the coherency using different temporal window lengths (for all models), coherency has been shown to decrease as the temporal window length increases (Figures 4.12, 4.13 & 4.14).

By increasing the window length slightly (from Δt to 0.5T), more of the signal can be sampled and the influence of the noise will decrease. However, if the temporal window length increases more than one period, the influence of noise (or signal from another reflector) becomes greater and affecting the coherency of the entire temporal window. The coherency decreases because the signal is present for only one period while the remaining time within the temporal window is measuring noise (or signal from another reflector). Therefore, a temporal window length of less than one period is desirable for detecting features below seismic resolution or distinct features smaller than the period of the signal (such as minor fractures or karst). Furthermore, when the window length is equal to one sample (Δt), coherent events tend to be spikier and incoherent noise tends to appear as false coherencies. This irregular pattern is due to the coherency calculations being more sensitive to slight similarities and dissimilarities from sample to sample such that noise may not be distinguishable from signal.

Similar patterns of coherency with variation in the temporal window length occur for weak and strong reflections alike. It can therefore be assumed that the variation in the temporal window length affects the coherency of all amplitudes similarly however, individual coherency values may differ based on differences in the signal-to-noise ratios.

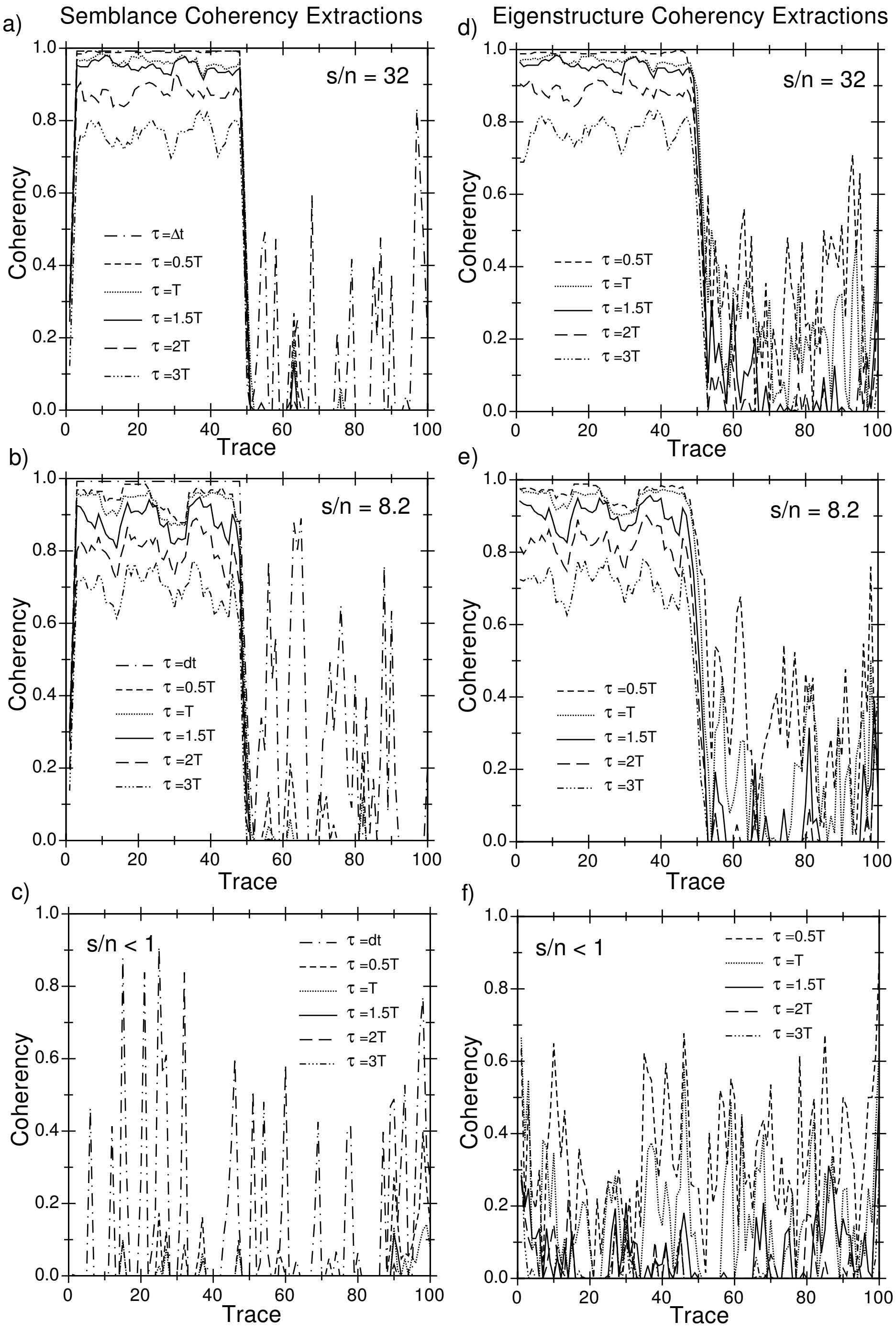

Fig. 4.12. Temporal window length analysis of the 80 Hz wave: Figures a-c are the semblance coherency extractions for the reflector with a) s/n=32 b) s/n=8.2 and c) s/n<1 (noise). Figures d-f are the eigenstructure coherency extractions for the reflector with d) s/n=32 e) s/n=8.2 and f) s/n<1 (noise). Figures a-f show the detailed variation of coherency across a faulted reflector.

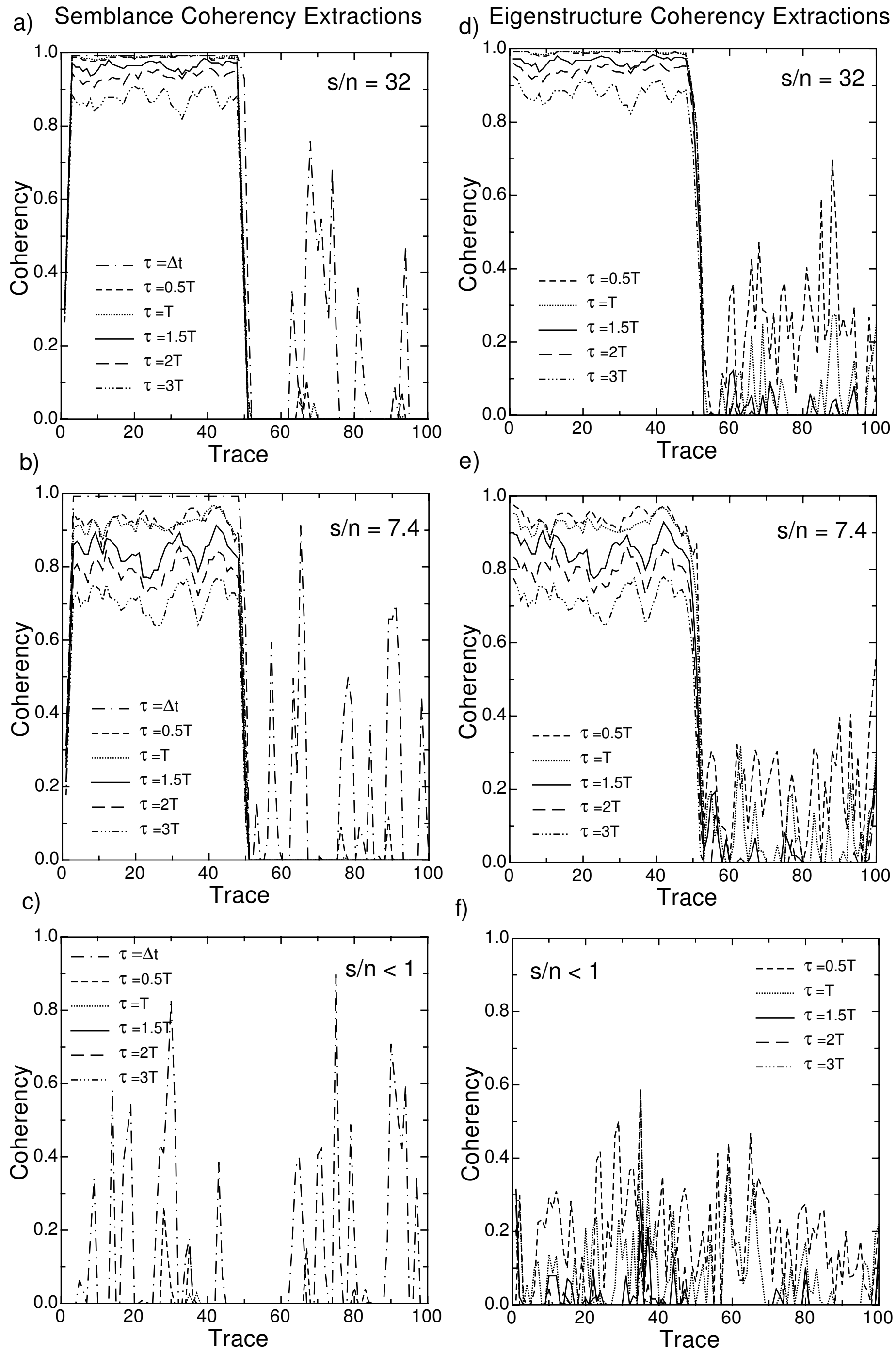

Fig. 4.13. Temporal window length analysis of the 80 Hz wave: Figures a-c are the semblance coherency extractions for the reflector with a) s/n=32 b) s/n=7.4 and c) s/n<1 (noise). Figures d-f are the eigenstructure coherency extractions for the reflector with d) s/n=32 e) s/n=7.4 and f) s/n<1 (noise). Figures a-f show the detailed variation of coherency across a faulted reflector.

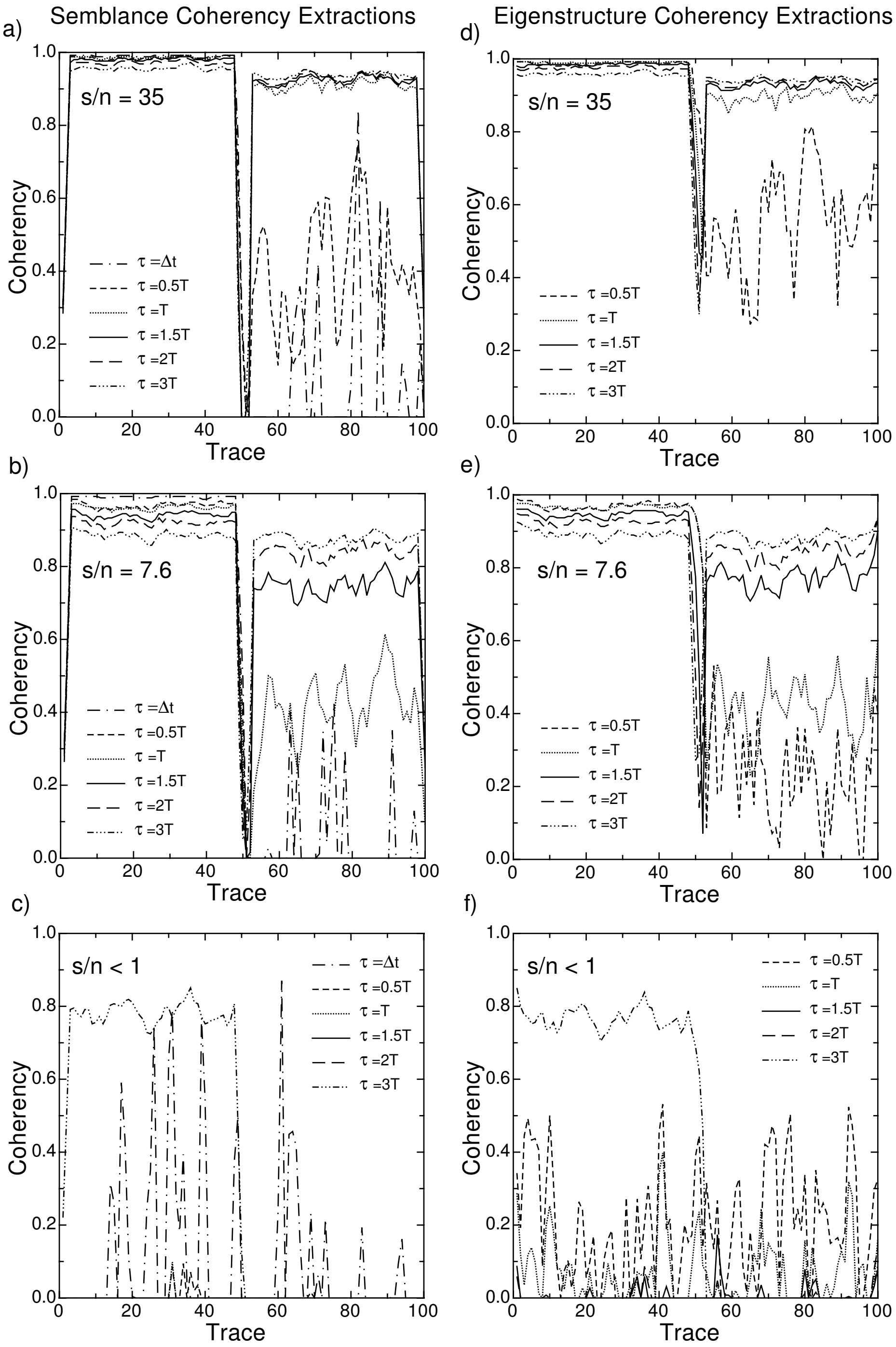

Fig. 4.14. Temporal window length analysis of the 80 Hz wave: Figures a-c are the semblance coherency extractions for the reflector with a) s/n=35 b) s/n=7.6 and c) s/n<1 (noise). Figures d-f are the eigenstructure coherency extractions for the reflector with d) s/n=35 e) s/n=7.6 and f) s/n<1 (noise). Figures a-f show the detailed variation of coherency across a faulted reflector.

4.2.2 Signal-to-Noise Ratio

Coherency for each model was computed by using the temporal window lengths of 0.5T and T. These temporal window lengths were chosen in order to maximize the vertical resolution of the coherency by lessening the influence of noise within the calculations. Examples of the coherency extractions through the faulted reflectors with an offset of 10 m (Figure 4.15) for the 80 Hz frequency are shown. Figure 4.15 shows the reflections with a signal-to-noise ratio that decreases from 32 to less than one. Similar coherency extractions are shown for the 50 Hz (Figure 4.16) and 20 Hz (Figure 4.17) frequencies respectively. Similar coherency extractions for the models with a 5 m offset are also shown (Figures 4.18, 4.19 & 4.20).

A seismic signal of a homogeneous reflector will be completely coherent in the absence of noise; however, this is hardly the case in the real world. Therefore, a variety of signal-to-noise ratios were applied to the models to approximate real seismic data. Noise will tend to have a similar coherency pattern independent of the amplitude or frequency content. This trend is most likely due to the normalization of the seismic data by the coherency algorithms. Therefore any similarity from trace to trace will be coherent while dissimilarities will be equally incoherent regardless of amplitude or frequency. Coherency extractions from the noise from each model illustrated nearly identical trends. Noise shows low coherence values with some spikes of higher coherent values in all models. False coherency of noise may be due to its random nature and similarities of noise from trace to trace. Although coherent spikes do occur, noise has an incoherent signature for the most part. These patterns are present along the coherency extractions.

Coherency is directly related to the signal-to-noise ratio. The eigenstructure algorithm was created to help attenuate the effects of noise on coherency. Although an increase in signal-to-noise ratio was shown to produce similar patterns within the semblance and eigenstructure coherency extractions, the eigenstructure algorithm produced overall higher coherency values with fewer incoherent spikes in the presence of noise. Semblance calculations allow for noise to be attenuated by the factor of $\sqrt{n}$. Therefore, the coherency of the input energy will be less sensitive to noise than through the use of the cross-correlation method. However, the semblance calculations are based upon a postulated reflector that best-fits the data within the analysis window (Marfurt et al., 1999) and thus the semblance from noise may possibly indicate an incorrect reflector as the best-fit. Although the influence of noise is decreased

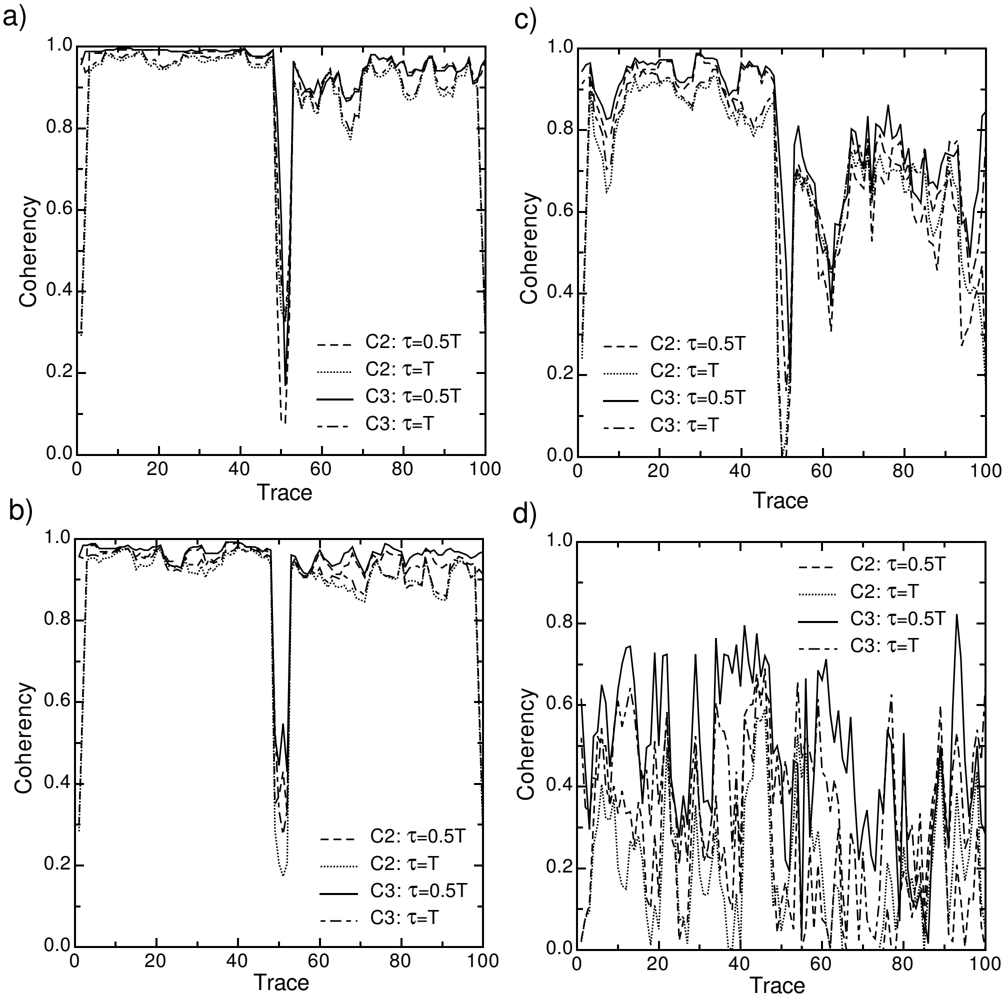

Fig. 4.15. Coherency extraction for the 80 Hz wave and a fault with a 10 m throw. a) Extraction of a reflection with s/n=32 b) reflection with s/n=8.2 c) reflection with s/n=3.2 d) reflection with s/n<1 (noise).

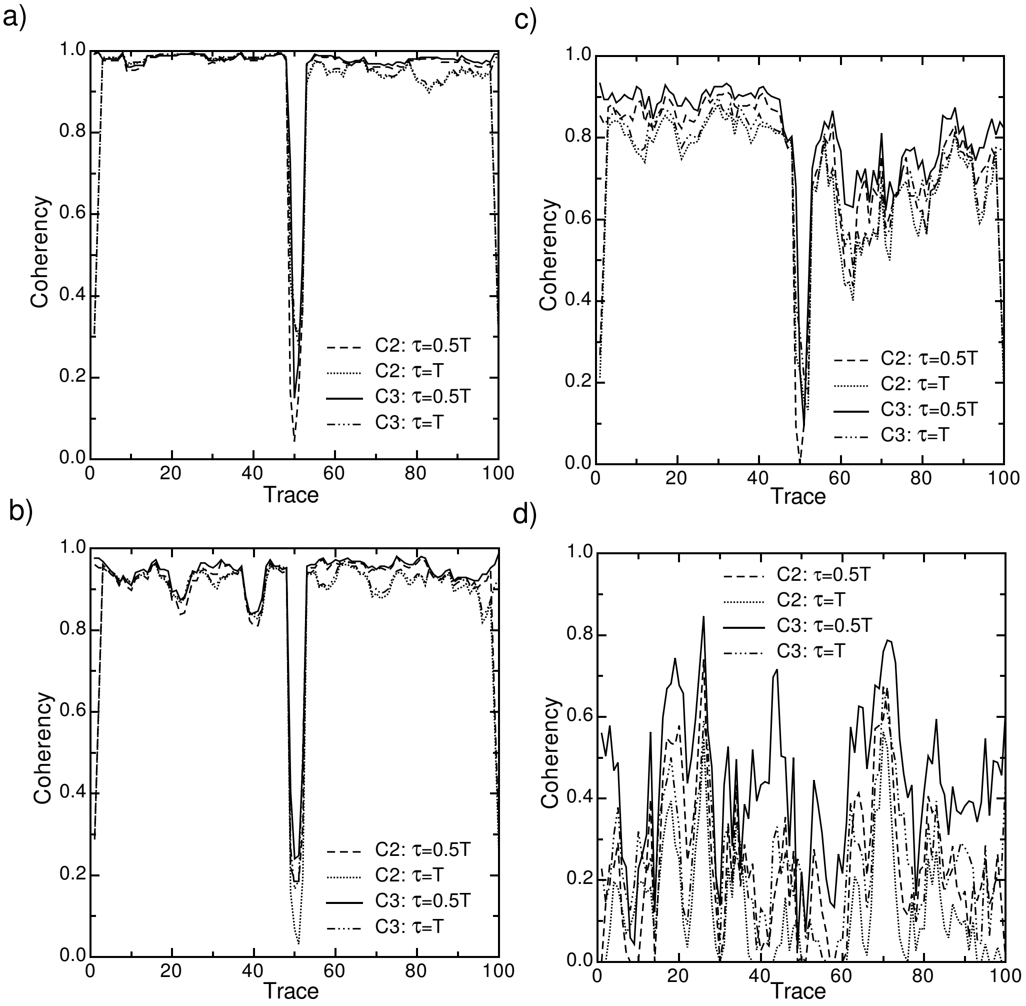

Fig. 4.16. Coherency extraction for the 50 Hz wave and a fault with a 10 m throw. a) Extraction of a reflection with s/n=32 b) reflection with s/n=7.4 c) reflection with s/n=3.2 d) reflection with s/n<1 (noise).

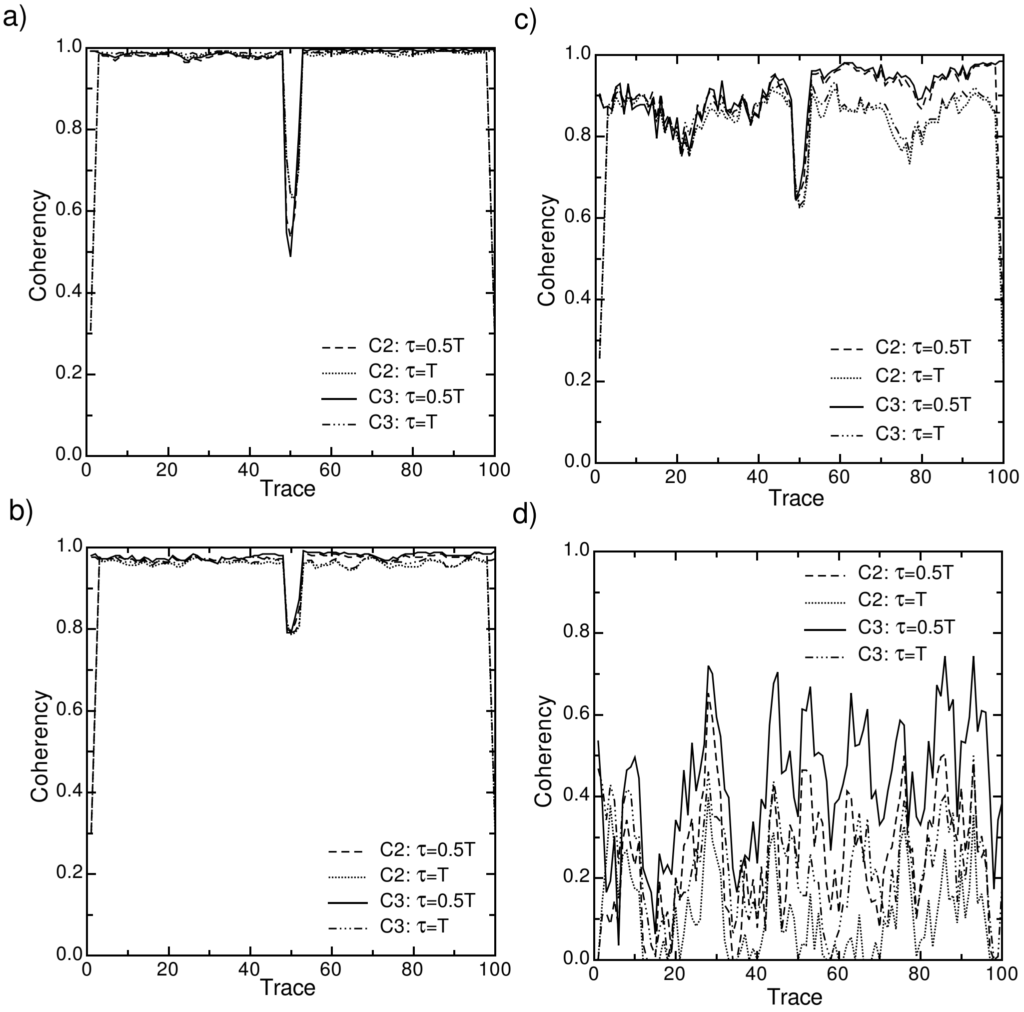

Fig. 4.17. Coherency extraction for the 20 Hz wave and a fault with a 10 m throw. a) Extraction of a reflection with s/n=35 b) reflection with s/n=7.6 c) reflection with s/n=3.5 d) reflection with s/n<1 (noise).

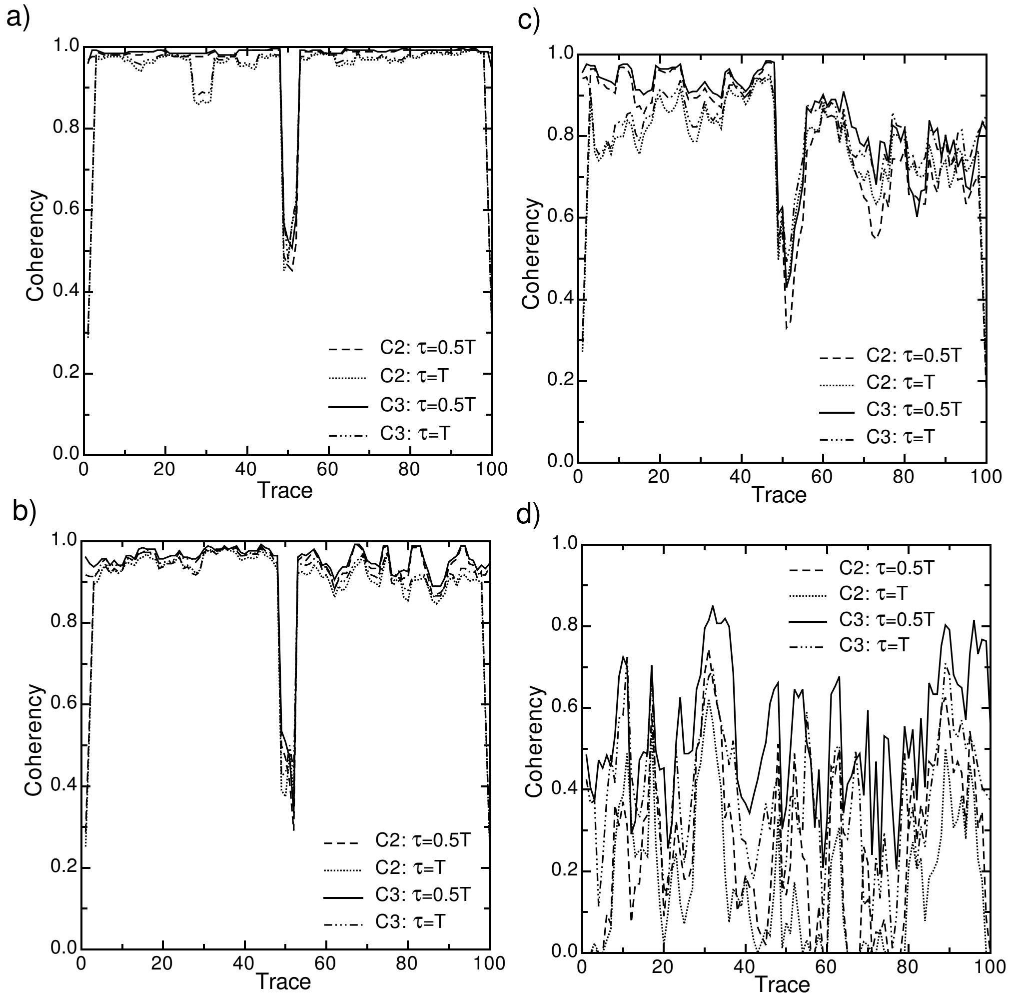

Fig. 4.18. Coherency extraction for the 80 Hz wave and a fault with a 5 m throw. a) Extraction of a reflection with s/n=32 b) reflection with s/n=8.2 c) reflection with s/n=3.2 d) reflection with s/n<1 (noise).

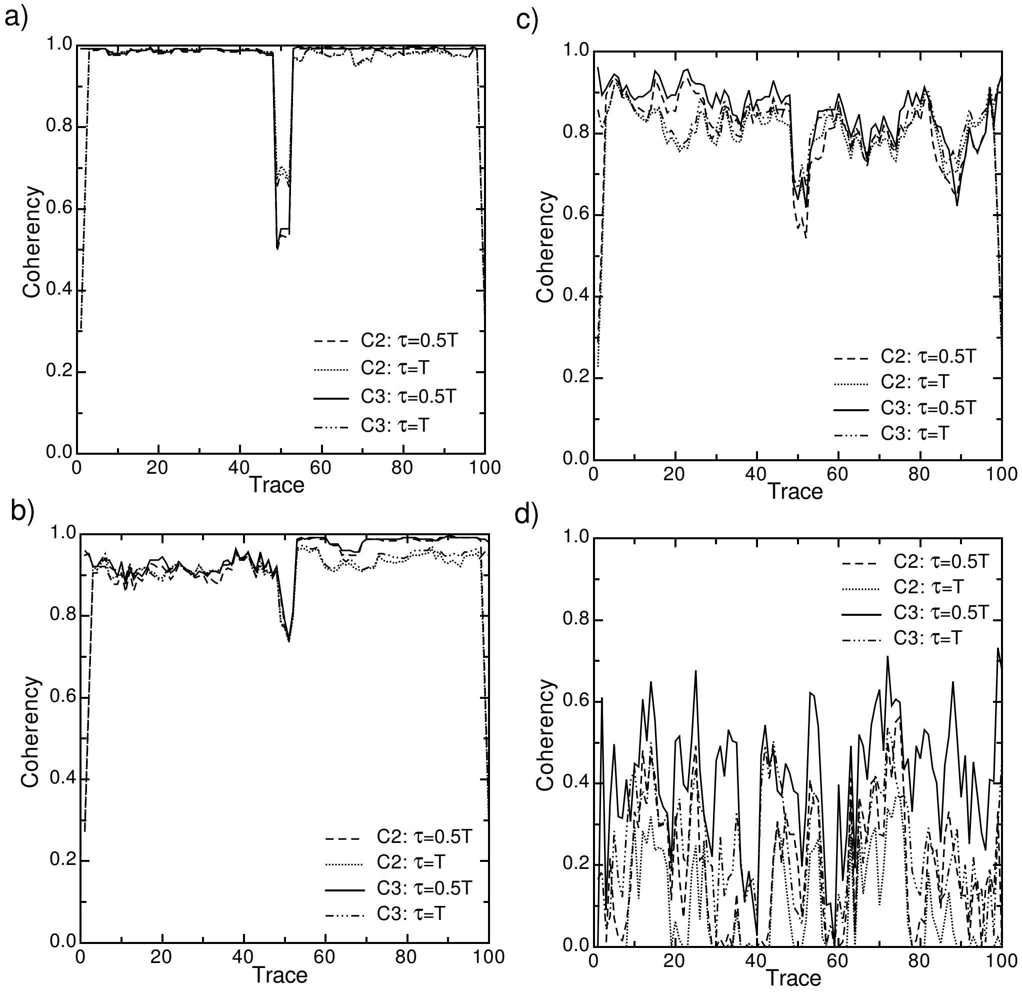

Fig. 4.19. Coherency extraction for the 50 Hz wave and a fault with a 5 m throw. a) Extraction of a reflection with s/n=32 b) reflection with s/n=7.4 c) reflection with s/n=3.2 d) reflection with s/n<1 (noise).

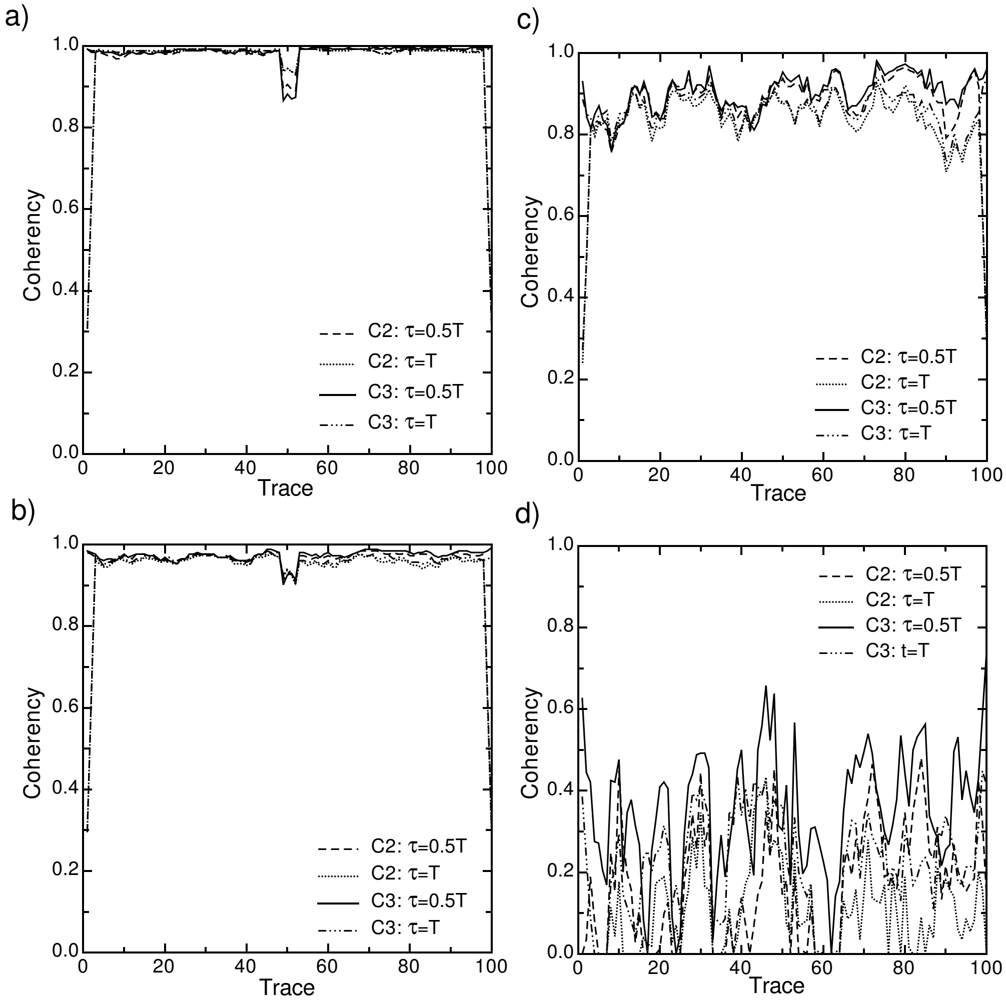

Fig. 4.20. Coherency extraction for the 20 Hz wave and a fault with a 5 m throw. a) Extraction of a reflection with s/n=35 b) reflection with s/n=7.6 c) reflection with s/n=3.5 d) reflection with s/n<1 (noise).

within the semblance calculation, noise still affects the best-fit dip/azimuth reflector that is used for the calculations.

Eigenstructures are a measure of the principle directions for the cross-plotted amplitudes within the temporal window. Random noise will typically be dispersed evenly about the eigenvectors and will therefore tend to be balanced by other noise. Therefore, noise has a limited influence on the coherency calculations of the C3 algorithm compared to the other coherency algorithms (C1 and C2). The eigenstructure coherency is therefore considered to be more efficient at attenuating noise from the coherency calculations. Figure 4.12 shows the coherency of noise for both the semblance (c) and eigenstructure algorithms (f). The semblance algorithm calculates noise as incoherent values, which can be clearly identified from signal. The ability of the eigenstructure algorithm to attenuate noise from the coherency calculations has made it somewhat difficult to distinguish between a coherent signal and false coherencies. Coherent noise may be mistakenly interpreted as a coherent signal in some instances when the data has a low signal-to-noise ratio. Semblance is more sensitive to noise and thus an irregular signal can easily be interpreted as noise. Therefore, the eigenstructure coherency will be more beneficial when identifying the coherency of a signal through a noise-dominated data set; while the use of both the semblance and eigenstructure coherencies can be used to identify noisy areas from false coherencies. The eigenstructure coherency was primarily used for this analysis to lessen the influence of noise on the coherency calculations.

Although noise increases the incoherence of a reflection, vertical displacement can be detected using coherency. Through variations of the synthetic model parameters, reflections with various signal-to-noise ratios were created (Table 4.1). Independent of the vertical throw of the fault, the coherency could only detect displacement of the reflector within the data that maintained a signal-to-noise ratio greater than 3. At the same time a fault with a small throw is imaged in a low frequency data set (e.g. 20 Hz), the reflector offset may have the typical coherency signature of noise (Figure 4.20). Therefore, it still may be difficult to distinguish a small-scale fault within low frequency data sets.

The long period of the 20 Hz wave within these data sets makes the subtle amplitude variations of the signal around a fault to appear more like the influence of noise rather than an isolated incoherent spike. Coherency may not recognize these minor amplitude variations on a long wavelet and may not show a strong incoherent trend typical of a fault. An increase in frequency will enhance the amplitude variations across the fault. This is due to the wavelength and period being shorter with a higher frequency signal and the wave's ability to detect a small feature. Also, within a given window, higher frequency waves will provide more information about the geophysical properties than will a low frequency wave. The higher frequency waves will have the ability to resolve smaller features, as the waves are sensitive to properties of the earth on a scale comparable to the wavelength. The wave is controlled by an average of properties over smaller scales, so the higher the frequency, the shorter the distance over which properties are averaged. Therefore, changes in the seismic properties associated to the presence of small-scale faults will be more distinct with higher frequency data.

The presence of a reflector is clear when the signal-to-noise ratio is greater than 3. It was therefore easy to determine the coherency pattern exhibited by a continuous reflector. Furthermore, when the signal-to-noise ratio was less than 1, the reflector could not be distinguished from the noise. Deviations from near complete coherency could be either due to the presence of a fault or noise. A fault tends to be an isolated valley (of low coherence) and span a width of the sample interval (Figure 4.15). Noise will exist throughout each coherency value and affect some locations more than others, resulting in a jagged appearance, causing most coherency values to become more incoherent (Figure 4.17). Therefore, a fault is interpreted as an isolated incoherent valley, distinctly different from the adjacent coherency values and from background noise.

The distinction between an incoherent spike due to a fault or noise may be difficult. A calculation of the mean coherency and standard deviation for the reflector in question will help to distinguish the difference. Any incoherent spike that has a change in coherency greater than the mean minus the standard deviation may be considered a fault (Figure 4.21). A 10 m fault (Figure 4.15) has a greater incoherent spike than a 5 m fault (Figure 4.18). Therefore, small-scale faults may not deviate far from the mean and possibly interpreted as noise. Although the use of the standard deviation will tend to eliminate the majority of questionable incoherent spikes, the interpreter should investigate many of the spikes that are close to the edge of the standard deviation error bars. This may also be true within field data when dealing with seismic traces adjacent to a fault that may behave coherently on both sides, such as a pure strike-slip fault.

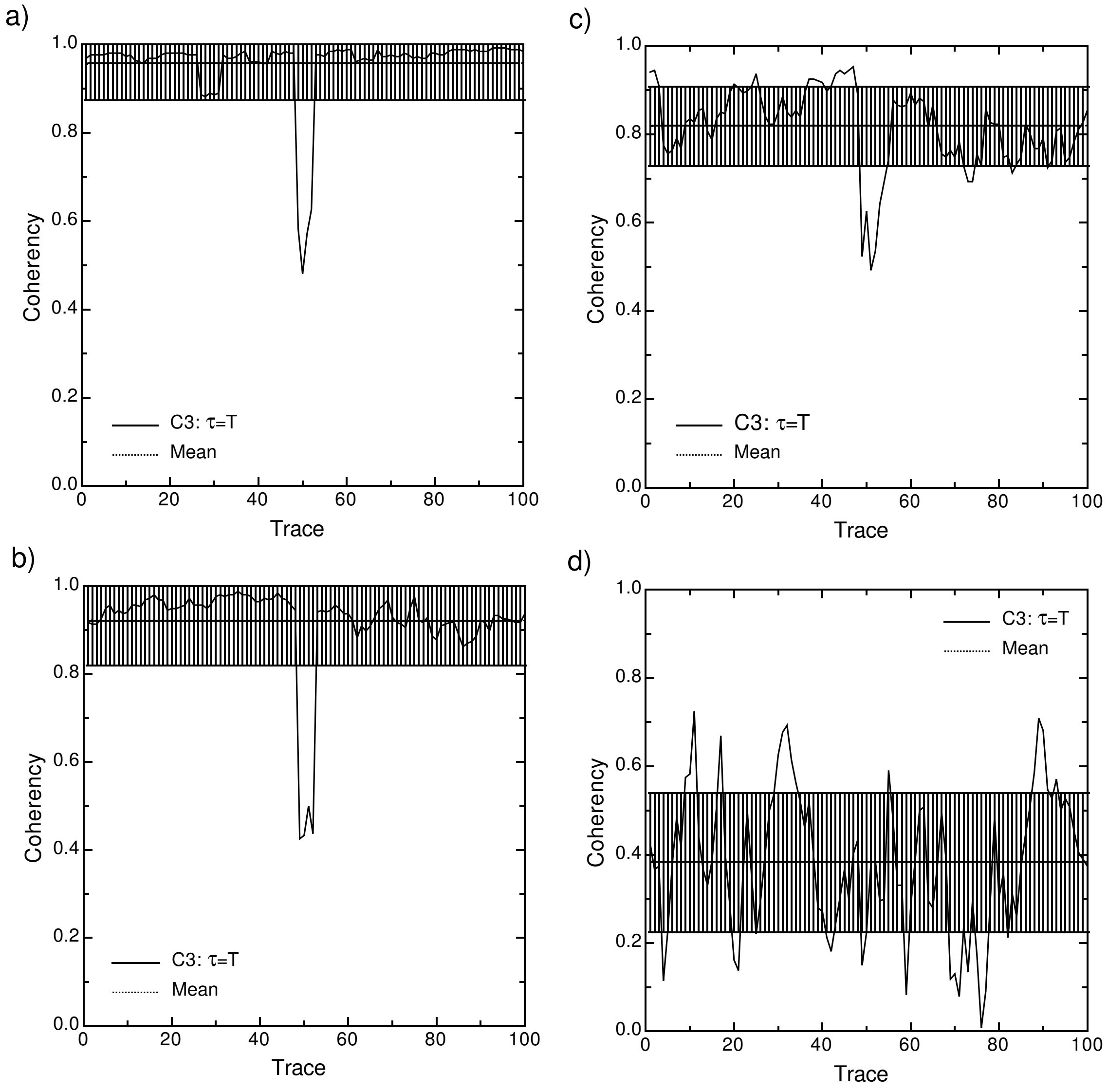

Fig. 4.21. Eigenstructure coherency extraction for the 80 Hz wave and a fault with a 5 m throw. The mean coherency and standard deviation from the mean are shown. a) Extraction of a reflection with s/n=32 b) reflection with s/n=8.2 c) reflection with s/n=3.2 d) reflection with s/n<1 (noise).

Through comparing the incoherent spikes and the standard deviation around the mean coherency value, a 5 m fault could be detected through each reflector that had a signal-to-noise ratio greater than 3 and for the most part, distinguished from noise (Figures 4.21, 4.22 & 4.23). Therefore, faults can be detected by coherency within relatively poor quality data. Two questions still remain. What is the minimum throw at which a fault can be detected using coherency? Also, what is the limit of signal-to-noise ratio that will allow coherency to image a fault, or reflector with some clarity?

4.2.3 Detectable Throw

Through a comparison of a coherency extraction through a faulted reflector (Figure 4.12a) and through noise (Figure 4.12b), a distinction between the coherency of a signal and the coherency of noise can be determined. The coherency of a reflector will change gradually with some isolated incoherent spikes, indicative of lateral changes in the rock properties, such as a fault or stratigraphic changes. The coherency of noise also changes randomly making it difficult to associate any variations within the rock properties from variations within noise.

Understanding the coherency results is difficult without knowledge of the ability by the algorithm to image features within data of various frequencies and signal-to-noise ratios. The ability to which seismic data can image a feature depends on the scale of that feature with respect to the input signal. To better understand what scale feature is being imaged, Table 4.2 shows the relationship of fault throw to the input signal's wavelength ($\Delta d/\lambda$) and two-way travel-time for the wave to pass through the fault to the signal's period (t/T). If a reflector is cut by a near vertical fault with a 10 m throw, a high frequency wave will detect the offset more easily than will a low frequency wave. This occurs because the period and wavelength decrease as the frequency of the input signal increases. Therefore, relating the throw of the fault to the input wavelength and the two-way travel-time to the period of the wave provides a new way to understand the limitations by coherency for detecting faults within different data sets.

The 10 m fault can be identified from the reflector and noise in the 80 Hz, 50 Hz and 20 Hz frequency data sets. However, an increase in frequency content allowed for the same magnitude fault to be imaged more coherently, most likely due to the faults

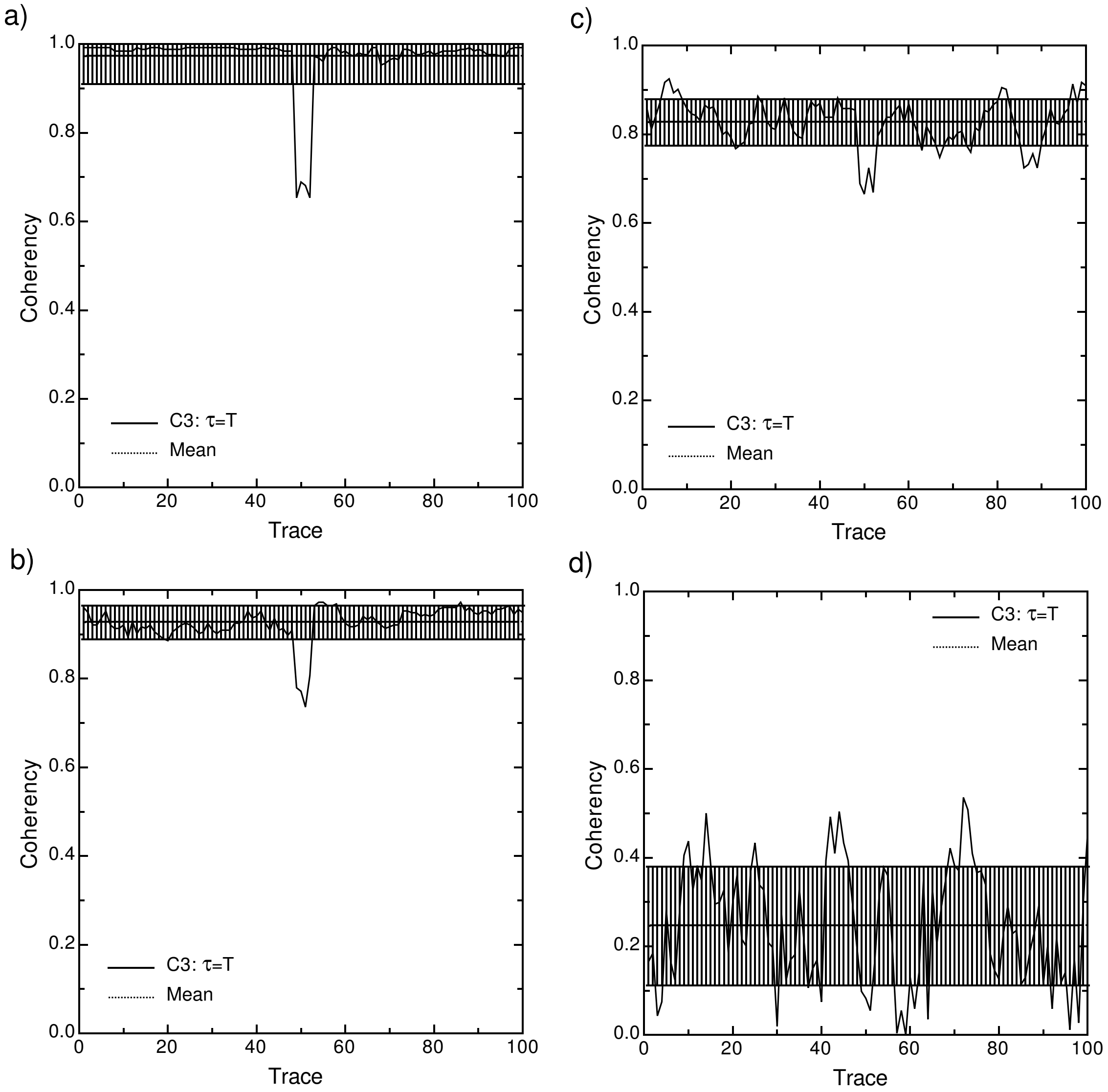

Fig. 4.22. Eigenstructure coherency extraction for the 50 Hz wave and a fault with a 5 m throw. The mean coherency and standard deviation from the mean are shown. a) Extraction of a reflection with s/n=32 b) reflection with s/n=7.4 c) reflection with s/n=3.2 d) reflection with s/n<1 (noise).

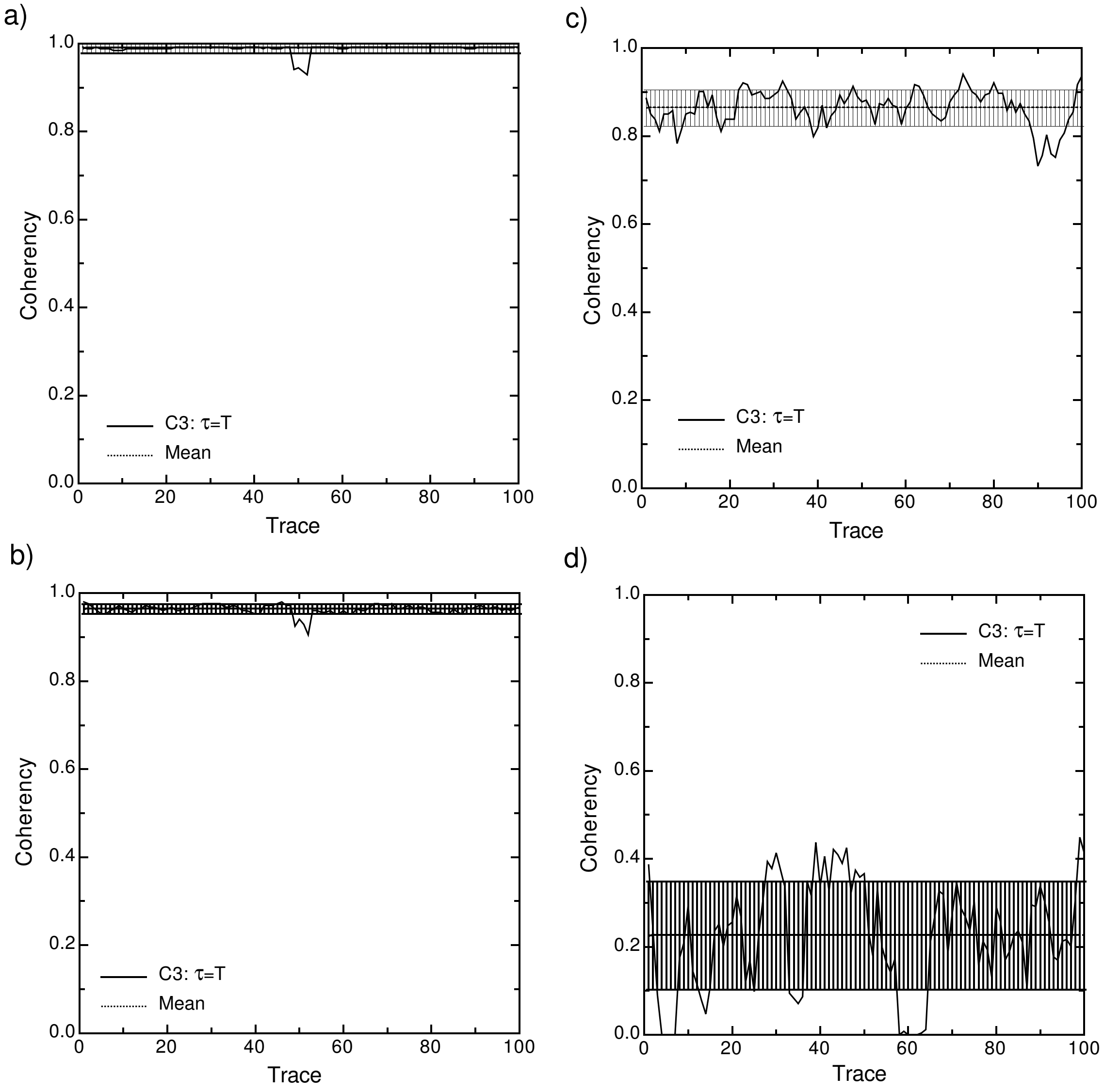

Fig. 4.23. Eigenstructure coherency extraction for the 20 Hz wave and a fault with a 5 m throw. The mean coherency and standard deviation from the mean are shown. a) Extraction of a reflection with s/n=35 b) reflection with s/n=7.6 c) reflection with s/n=3.2 d) reflection with s/n<1 (noise).

Table 4.2. Ratios for the throw-to-wavelength and two-way traveltime-to-period for the faults used for each model.

Throw	$\Delta d/\lambda$	t/T	$\Delta d/\lambda$	t/T	$\Delta d/\lambda$	t/T
(m)	20 Hz		50 Hz		80 Hz	
0	0.00	0.00	0.00	0.00	0.00	0.00
1	0.01	0.01	0.01	0.03	0.02	0.05
5	0.03	0.06	0.07	0.12	0.11	0.24
10	0.06	0.12	0.14	0.30	0.23	0.49
20	0.11	0.24	0.29	0.60	0.46	0.97
50	0.29	0.61	0.71	1.52	1.14	2.42
100	0.57	1.21	1.43	3.03	2.29	4.85

throw being closer in distance and time to a high frequency wavelength and period than to a low frequency wavelength and period. Similarly, the 5 m fault can also be identified from the reflector and noise in the 80 Hz and 50 Hz but not as clearly in the 20 Hz frequency data set.

Coherency can detect the 5 m fault within the 80 Hz and 50 Hz data sets as long as the signal-to-noise ratio is greater than 3 (Table 4.1). Within the 20 Hz data set, the 5 m fault can be detected as long as the signal-to-noise ratio was greater than 7 (Figure 4.23). The 5 m fault has a lower $\Delta d/\lambda$ and t/T value with the 20 Hz data set. Therefore, the detection of small-scale faults can be done when the signal-to-noise ratio increases. Coherency is more sensitive to noise for features with low $\Delta d/\lambda$ and t/T values. To obtain the best results for identifying the presence and throw of small-scale faults within poor quality data sets, the frequency content should be as high as possible.

A 1 m fault can not be identified from the reflector and noise in either the 80 Hz or 50 Hz data sets. Therefore, the limit at which a fault can be detected from the 20 Hz frequency data set is between 10 m and 5 m; both the 50 Hz and 80 Hz data set are between 5 m and 1m. These resolution limits are accurate for data sets with a signal-to-noise ratio greater than 3.

The $\Delta d/\lambda$ and t/T coefficients allow for one to understand the limits to which interpretation can be done with certainty. The $\Delta d/\lambda$ limit for the 80 Hz, 50 Hz and 20 Hz data sets where a fault could and couldnt be detected was between 0.1 and 0.05. Therefore, a fault that has a throw greater than 5% of the wavelength should be detected by coherency. Similarly, the t/T coefficient will also indicate for vertical resolution of coherency. The t/T limit for the 80 Hz, 50 Hz and 20 Hz data sets where a fault could and couldn't be detected was approximately 0.1. Therefore, a fault that has a two-way travel-time greater than 10% of the period should be detected by coherency. These limits hold true as long as the signal-to-noise ratio is greater than 3 for 50 Hz and 80 Hz frequencies and greater than 7 for 20 Hz frequency data sets.

Through tests of 80 Hz, 50 Hz and 20 Hz data sets that were subsampled at 1 msec intervals, coherency can detect a fault that has a throw at least 5% of the wavelength or two-way travel time at least 10% of the period. In general, small-scale faults will be able to be detect better within higher frequency data sets. If coherency can detect such faults, then coherency has the ability to detect a geophysical feature that might be less than one sample interval in time or thickness or below tuning. Although amplitude variations might be slight and easily overlooked using traditional interpretation methods, coherency can detect any lateral amplitude variations. Geophysical features smaller than the sampling interval can be detected by coherency most likely because the algorithms subsample the data at 1 msec intervals, thus improving the resolution.

Although coherency has the ability to detect small scale faults, interpretation is most accurate when coherency is used in conjunction with traditional mapping techniques. Through associating subtle amplitude features on 2D seismic lines with the coherency across the features, the distinction between noise and geology can be determined more accurately. These results indicate that data sets with poor signal-to-noise ratios can be interpreted with some certainty.

CHAPTER V

COHERENCY ANALYSIS OF FIELD DATA

The application of the semblance and eigenstructure coherency algorithms to the synthetic models yields results that will help to interpret the geophysical implications of most seismic data volumes. Variations in frequency content and signal-to-noise ratio and the affects on the limits of resolution for each coherency model have been investigated. Therefore, synthetic representations of most real-world geophysical models have been studied and the limits to which one can interpret faults with some certainty have been identified.

5.1 Methods

A field-seismic volume with a target interval between approximately 18,000 and 24,000 ft below the land surface was mapped. This horizon was chosen to validate the synthetic results because the seismic acquisition parameters were established for optimization at or above a depth of 16,000 ft. Therefore, the seismic target of this study is below optimal resolution and the signal-to-noise ratio was relatively low (2).

The field data provided by ConocoPhillips Inc. consists of a 3D seismic survey covering an area of 14 mi^2 and a total recorded time of 4000 ms. Post-stack processing was needed to effectively image and subsequently map the target. A 2-10 Hz, 40-50 Hz Butterworth-band pass filter and 250 ms automatic gain control were applied to the original data (Figure 5.1). All interpretation was done on the post-stack processed data. Figure 5.1 shows a seismic line (crossline C) centered on the horizon of interest to ConocoPhillips. The seismic data, which images a reservoir of the Hunton Group within the Anadarko Basin, provides a basic image of the subsurface. The Hunton horizon was identified using well-log picks and a synthetic seismogram and mapped along the associated peak to the synthetic well tie. A basic structural setting was interpreted through mapping the dominant faults using the seismic amplitude volume. After the application of the coherency volume, a clearer image of the structural setting reinforced the previous interpretation along with indicating the presence of more small-scale faults not easily identified using the seismic amplitude volume.

The small-scale faults were identified and mapped using the same procedures outlined for the synthetic models. Faults on the structural high were the focus of field data interpretation in order to provide possible hydrocarbon targets for ConocoPhillips.

5.2 Results and Interpretation

The coherency analyses of the synthetic models have been shown to provide improved guidelines to interpreting the structural settings of field data. Coherency has been traditionally used to provide a quick and easy structural interpretation (Bahorich and Farmer, 1995) however; it has now been shown to be able to provide information about the magnitude to which a fault offsets the reflectors. The coherency analysis has also provided greater confidence with interpreting a structural regime within a data set that has a poor signal-to-noise ratio. Therefore, a data set that has a poor signal-to-noise ratio was used to verify and validate the results for the synthetic models. The small-scale structural features at the crest of a structural high were mapped using coherency.

5.2.1 Geophysical Interpretation

Through creating a synthetic trace from a sonic log acquired in well 3 (Figure 5.2), the Hunton was determined to be a seismic peak. It was therefore mapped as the associated peak within well 3 and correlated to well ties within the rest of the seismic survey. During the time that the Hunton was mapped, the structural regime was initially interpreted using traditional mapping techniques. Offsets or distinct variations within the seismic amplitude were used to outline the clearly visible reverse and strike-slip faults that dominate the locality. The majority of these faults were high-angle, near vertical with offsets of a few hundred feet. The depth map of the Hunton (Figure 5.3) shows the relationship of the reverse faults (Northwest-Southeast trending) and the strike-slip faults (Northeast-Southwest trending) with the structural high, which contains several prolific hydrocarbon-producing wells. Although the structural regime was interpreted using traditional methods, a coherency analysis was employed in order to identify small-scale faults on the structural high to assist in determining the location for future wells in the producing area.

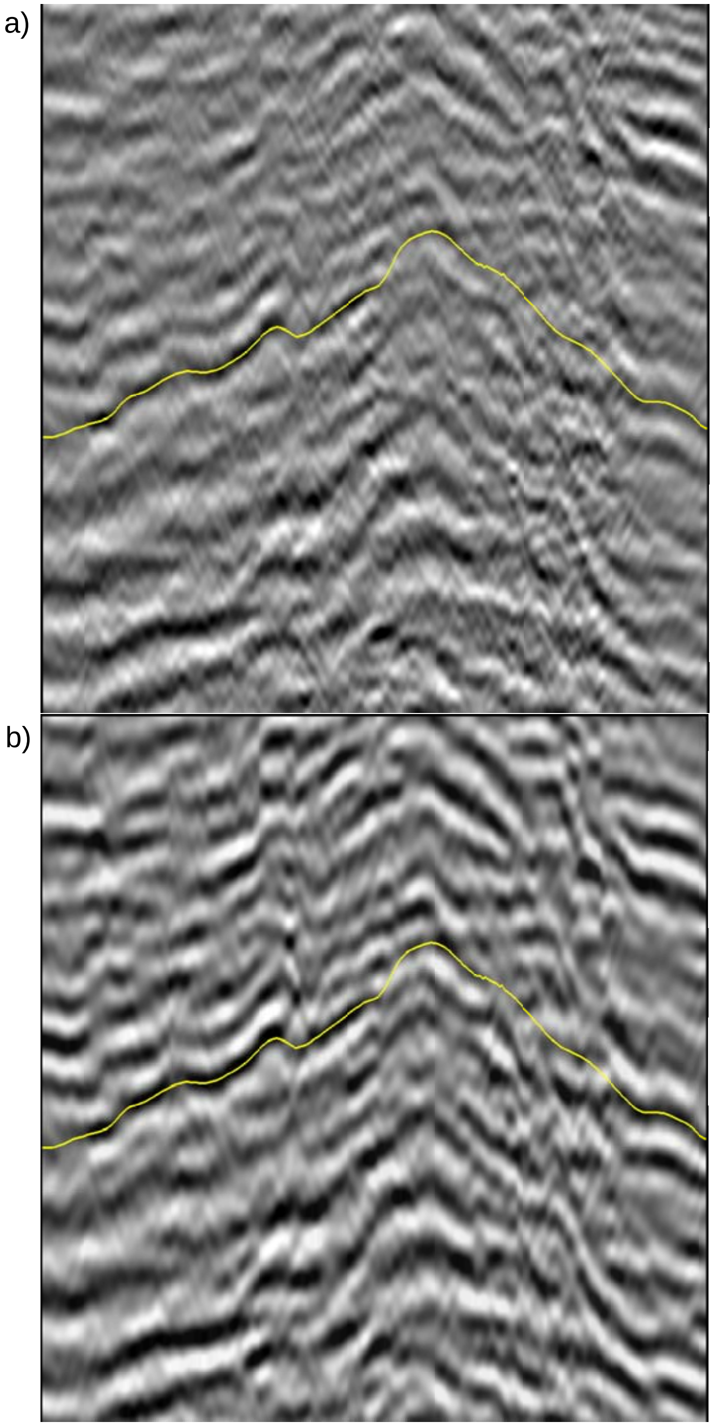

Fig. 5.1. Seismic sections of the a) Original processed field data b) Post-stack processed field data with a 2-10 Hz, 40-50 Hz band-pass filter and 250 ms agc. Highlighted in yellow is the horizon of interest to ConocoPhillips. The seismic sections represent a relative time of approximately 500 ms.

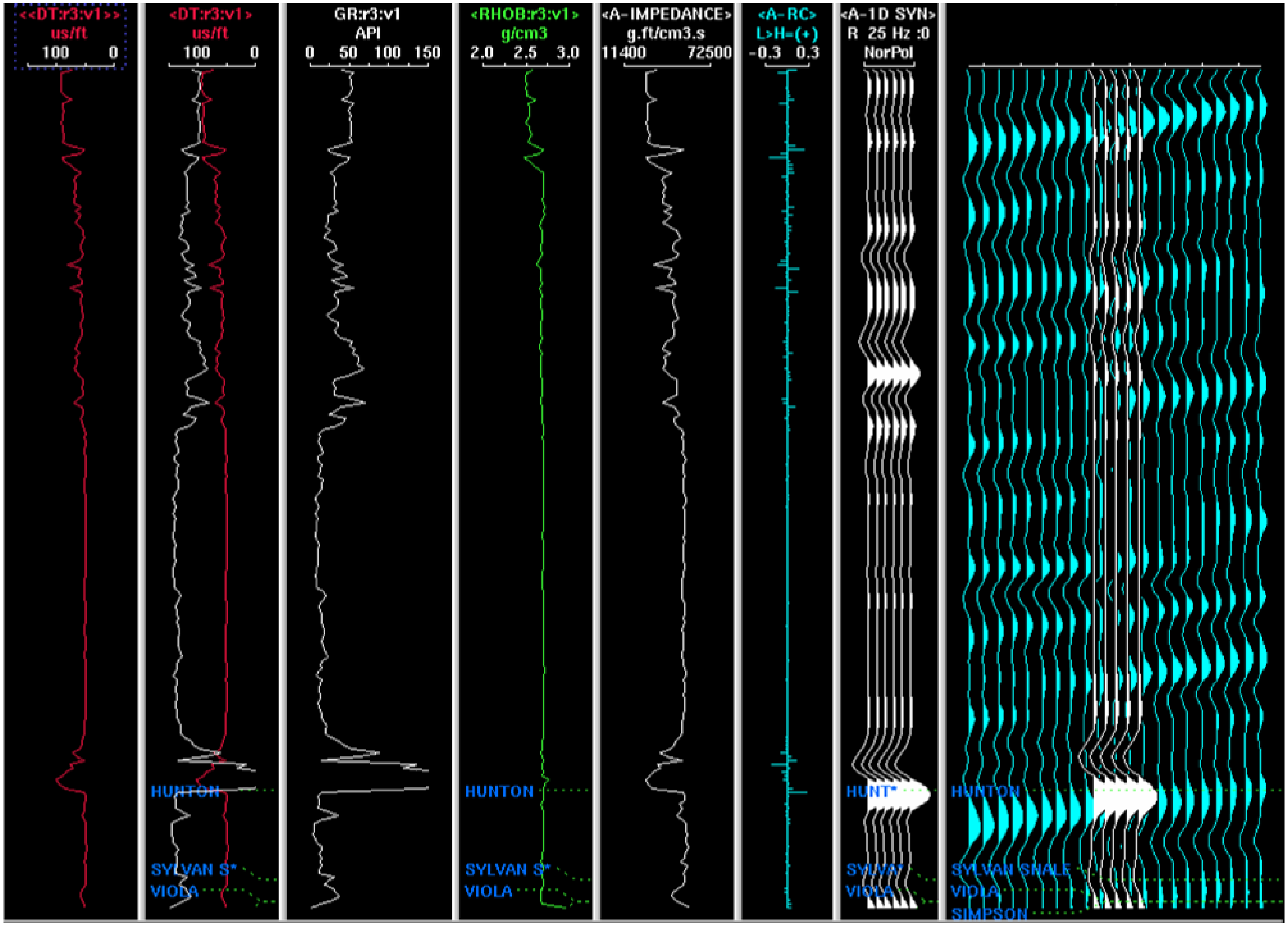

Fig. 5.2. Synthetic tie with well 3 used to correlate the Hunton Group within the seismic data.

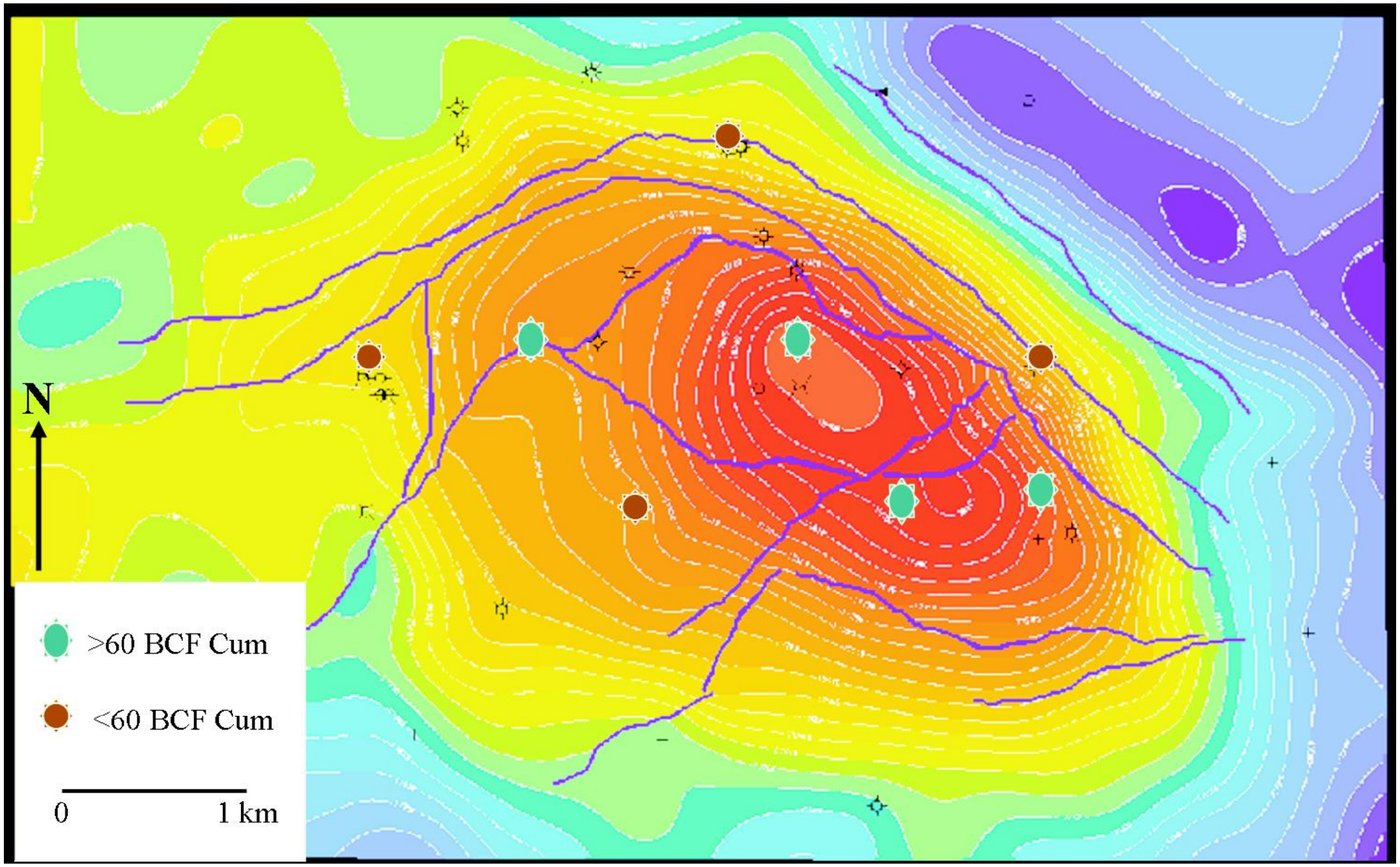

Fig. 5.3. Depth map of the Hunton horizon, with blue scaling to red from deeper to shallower depths. The wells and associate hydrocarbon production are labeled. The dominant faults easily identified using seismic section are displayed in blue.

5.2.2 Coherency Analysis

The field data initially had a signal-to-noise ratio of approximately 3. Following the poststack processing, the signal-to-noise ratio improved to approximately 8. The signal-to-noise ratio was computed through a comparison of the signal and noise within Figure 5.4. The dominant frequency was approximately 30 Hz while the noise had frequencies greater than 60 Hz. The central frequency corresponds to a wave with a period of 33 ms and a wavelength approximately 200 m. Based upon the coherency results for the synthetic data sets a fault with throw greater than 10 m or a two-way travel time greater than 3 ms should be detectable within this data set.

The coherency analysis for the field data was done in a similar fashion to the analysis of the synthetic data. The semblance and eigenstructure coherency algorithms were applied with temporal window lengths of 0.5T, T, 1.5T, 2T, 3T, 4T and 5T respectively. The frequency content of the field data suggests that the dominant frequency is approximately 30 Hz (Figure 5.4); therefore, the temporal window lengths were based upon the period of a 30 Hz wave. Following the coherency processing, the volumes were flattened along the Hunton horizon in order to understand the structural regime of the Hunton itself. Flattening can either be done prior to or following the coherency analysis. In this situation, where the data has a poor signal-to-noise ratio, the volumes were flattened following the coherency processing. If the volumes were flattened prior to the coherency processing, any mispicks of the horizon would produce coherency results that would be based on the signals from different reflectors rather than just the Hunton. Furthermore, flattening prior to the coherency calculation will in effect eliminate the throw of the faults present. Therefore, flattening was done following the coherency calculation in order to preserve the coherency values and view the horizon's incoherencies more clearly. Figures 5.5 & 5.6 show flattened semblance and eigenstructure coherency time slices through the Hunton horizon respectively. Both coherency maps show incoherent features however, the semblance map contains more random and linear features, associated with noise or processing artifacts. The eigenstructure coherency algorithm was not as sensitive to the processing artifacts as was the semblance algorithm. Therefore, the eigenstructure coherency was used for this analysis to lessen the influence of noise and poor processing on the interpretation. Figures 5.7 & 5.8 show a comparison of the seismic to the eigenstructure coherency sections for crosslines B and C. Vertical offset of reflectors within the seismic section correspond to vertical black liniments on the coherency sections.

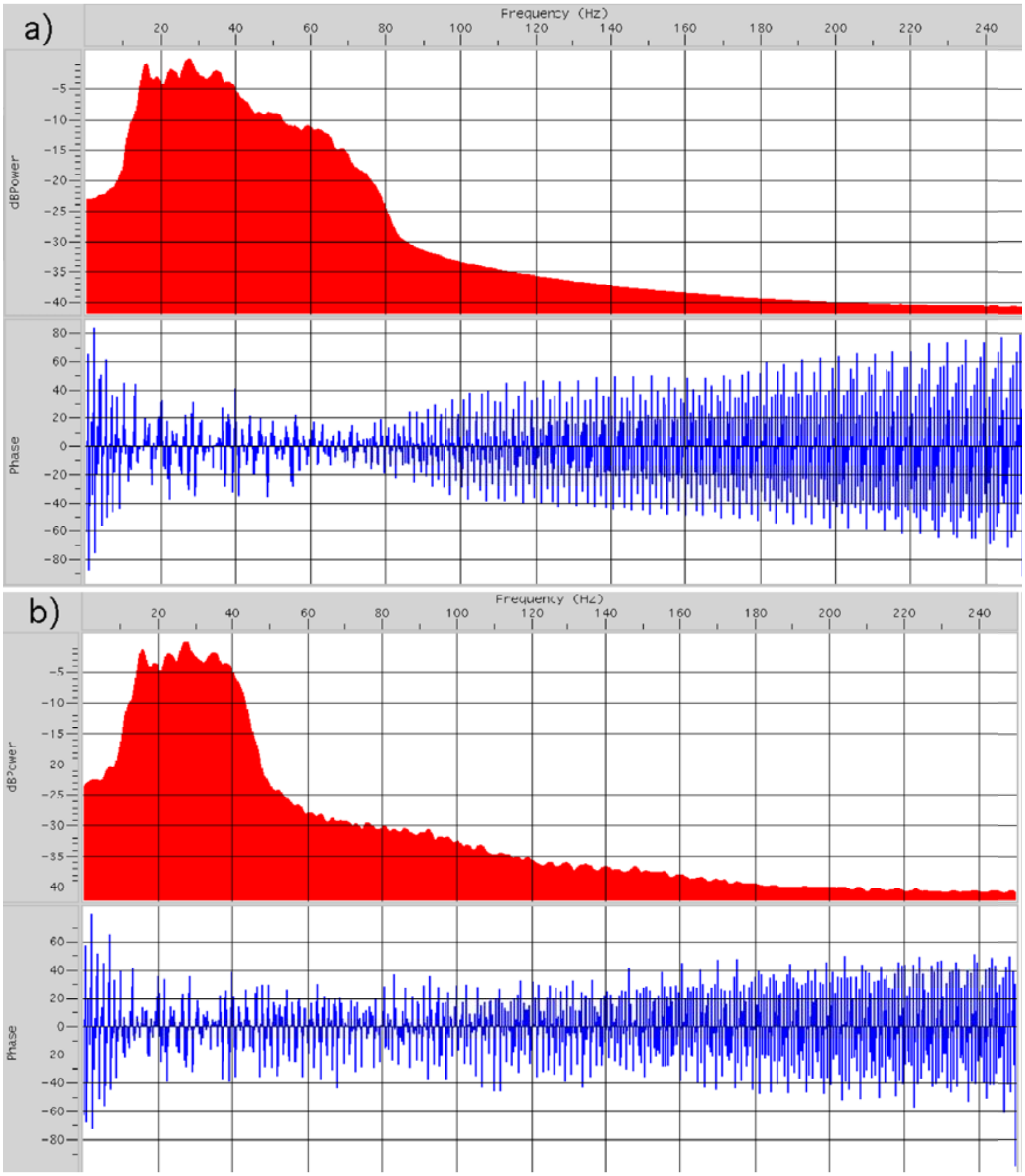

Fig. 5.4. Frequency and phase spectral analysis of the seismic data representing 500 ms surrounding the target horizon a) Original processed data with a s/n<3 b) Post-stack processed data with a s/n<8.

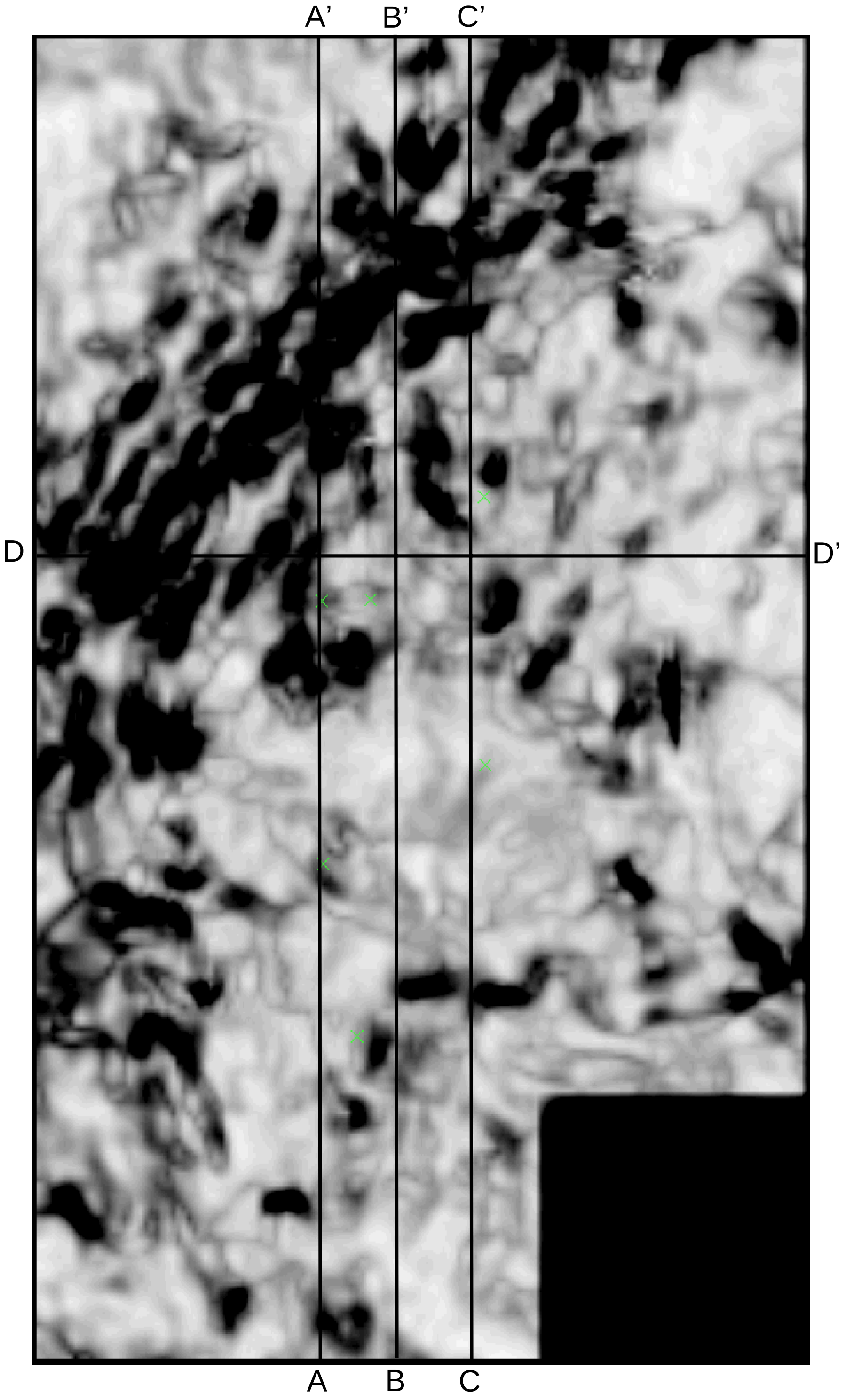

Fig. 5.5. Semblance coherency map flattened along the Hunton horizon. Flattening occurred following the coherency calculation.

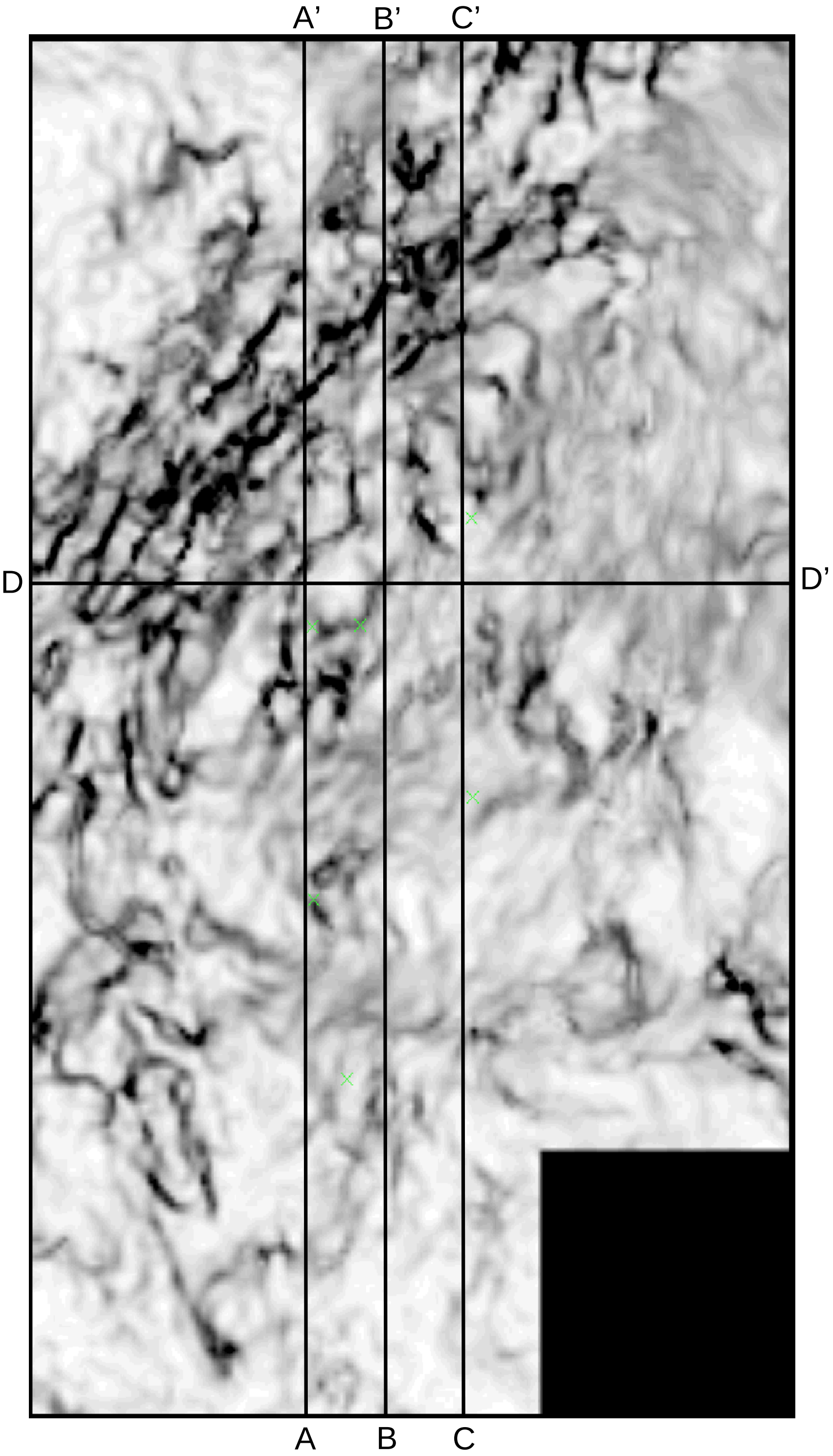

Fig. 5.6. Eigenstructure coherency map flattened along the Hunton horizon. Flattening occurred following the coherency calculation.

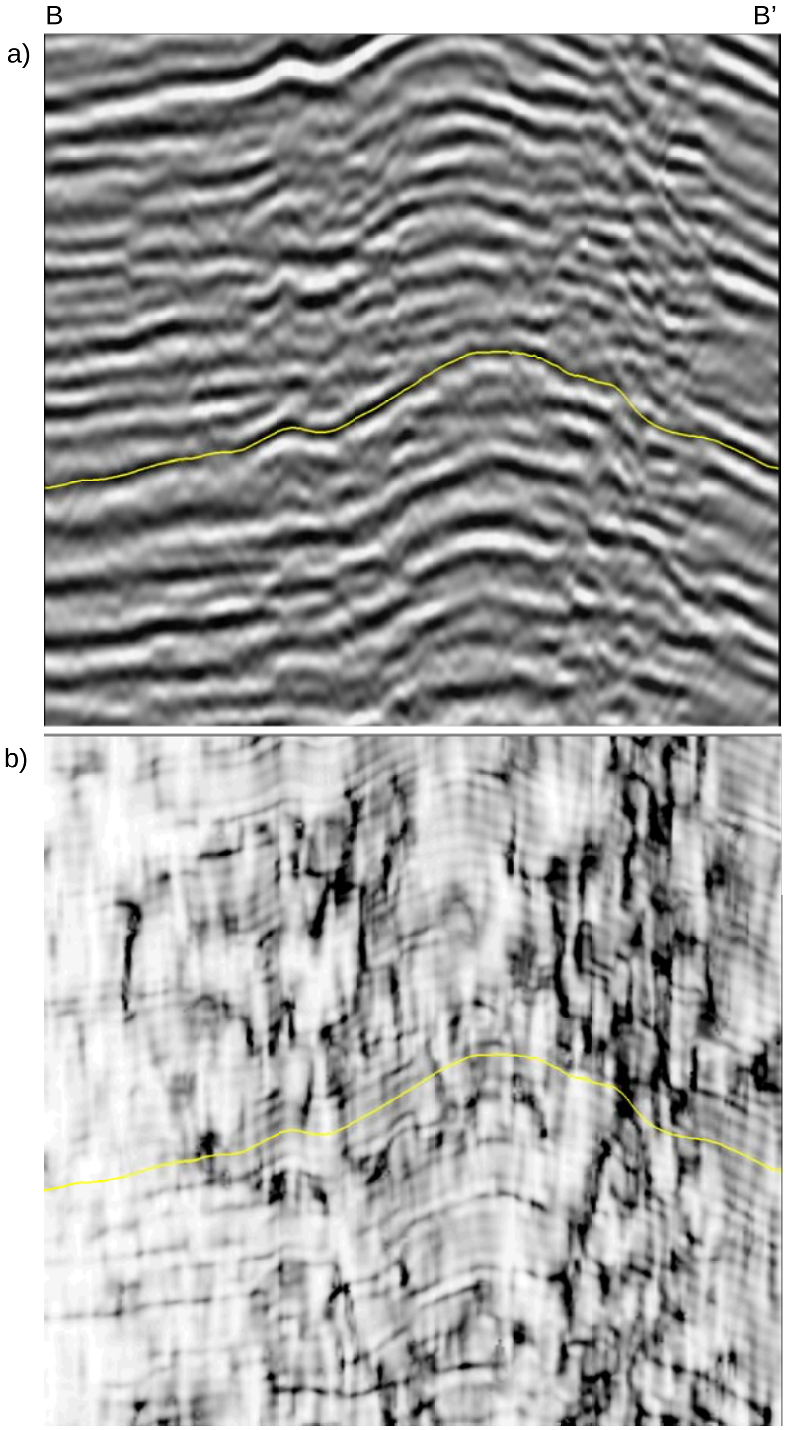

Fig. 5.7. a) Seismic section of crossline B. b) Eigenstructure coherency section of crossline B. The sections represent a time of 500 ms. The Hunton is highlighted in yellow.

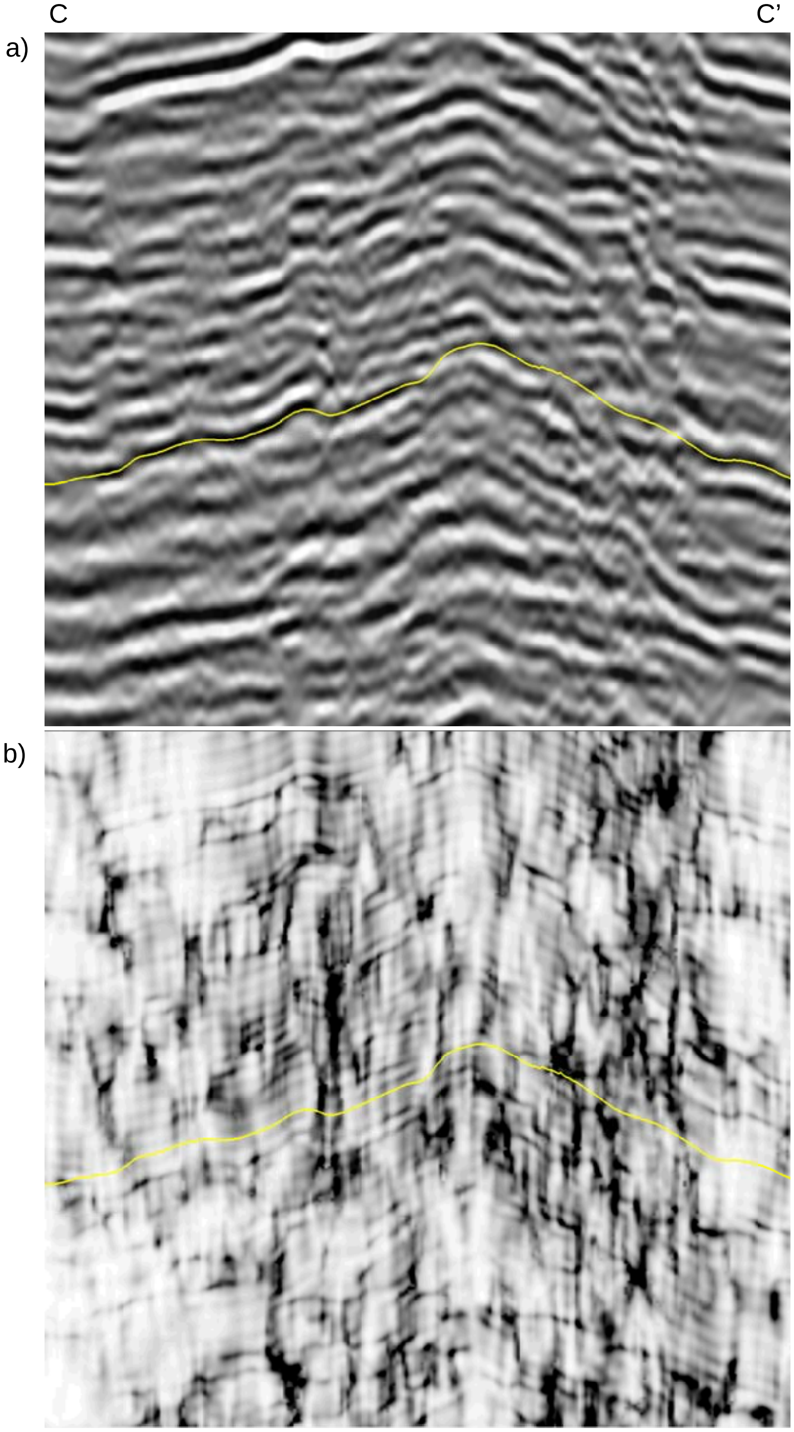

Fig. 5.8. a) Seismic section of crossline C. b) Eigenstructure coherency section of crossline C. The sections represent a time of 500 ms. The Hunton is highlighted in yellow.

The best way to determine if there are any small-scale faults that might be overlooked using traditional interpretation methods was to take coherency extractions along lines and crosslines on the flattened-time slice over the structural high. These coherency extractions illustrated the location of both the large and small-scale incoherent events. A comparison of the coherency extractions from the data volumes created, using different temporal window lengths, showed that coherency decreased when the temporal window length increased (Figures 5.9 & 5.10). Although coherency values were different between the volumes, the large incoherent spikes typically were pervasive throughout the extractions. Some of the small-scale incoherent events however disappeared. This evidence supports the temporal window length analysis for the synthetic seismic data sets.

To investigate the small-scale features of the structural high, the coherency extractions for the volumes with temporal window lengths of 0.5T and T were interpreted. Although both temporal window lengths showed similar incoherent spikes, the shorter, 0.5T window produced more spikes that tended by influence by noisy sections. Therefore, the majority of the coherency analysis was done using the coherency volume with a temporal window length equal to one period in an attempt to minimize false coherent spikes.

Coherency extractions for crossline A, B and C and line D show the location of the incoherent spikes (Figure 5.11). A zone within each crossline shows several large incoherent spikes. These spikes also extend past the standard deviation range from the mean coherency of the line indicating that the incoherency is most likely due to geology rather than noise. These spikes have been interpreted as the primary deformation zone (PDZ) for the structural high and have an orientation similar to the regional structural trends. Through an examination each line through this area, high-angle reverse faults with throw of 500-800 ft can be interpreted. These faults can be easily identified through a comparison of the seismic section to the coherency section of the PDZ along crossline A (Figure 5.12). The trace-to-trace incoherencies along the structure of crossline A (Figure 5.13) can be better illustrated by flattening the seismic data along the Hunton horizon (Figure 5.14). Crossline B (Figures 5.15, & 5.16 & 5.17) and crossline C (Figures 5.18, & 5.19 & 5.20) also have similar faults. These faults are clearly noticeable using traditional interpretation methods and therefore will be used as a comparison and validation technique for the small-scale fault analysis.

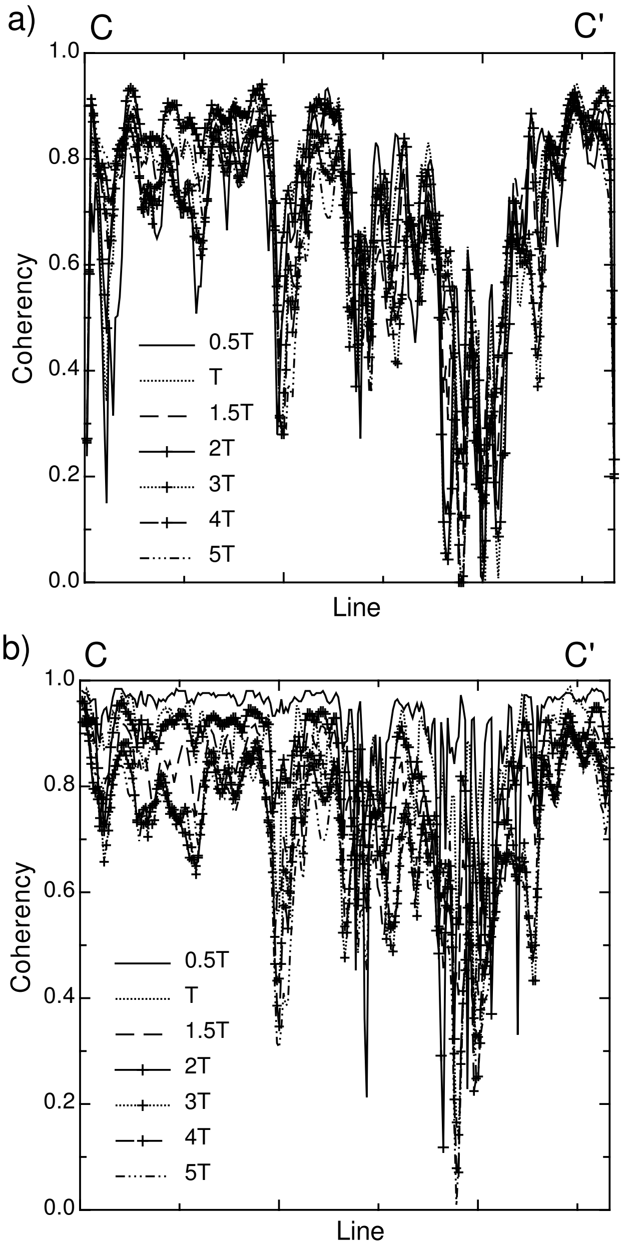

Fig. 5.9. Temporal window analysis of the a) Semblance coherency b) Eigenstructure coherency for a crossline C.

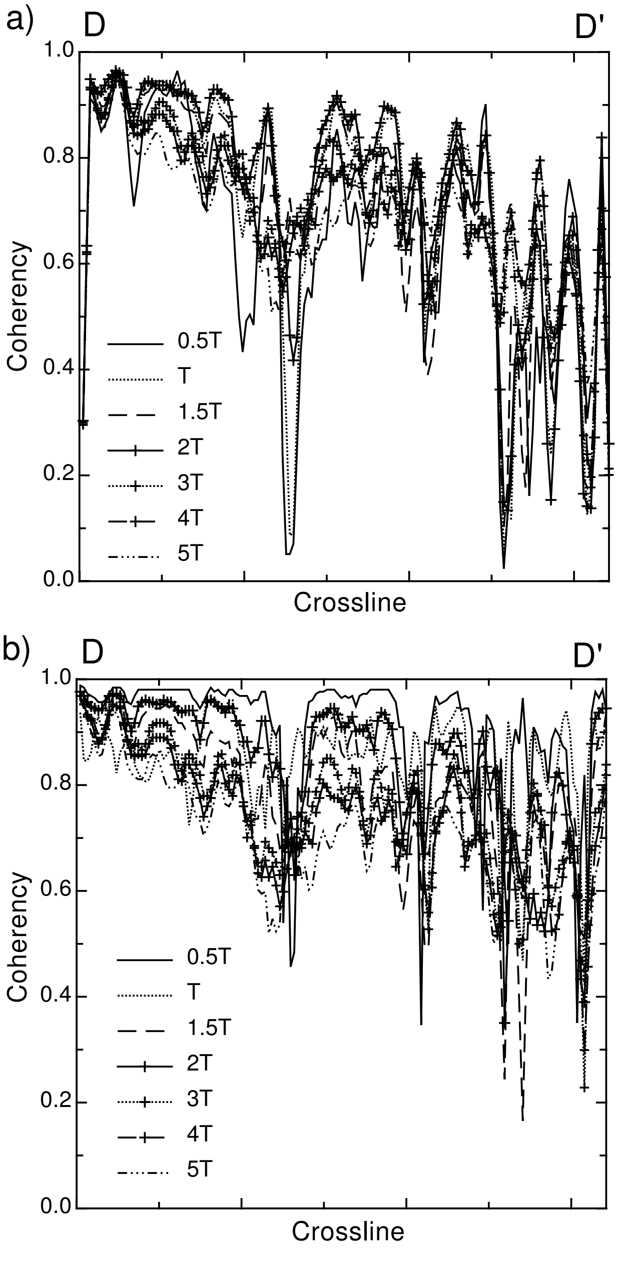

Fig. 5.10. Temporal window analysis of the a) Semblance coherency b) Eigenstructure coherency for line D.

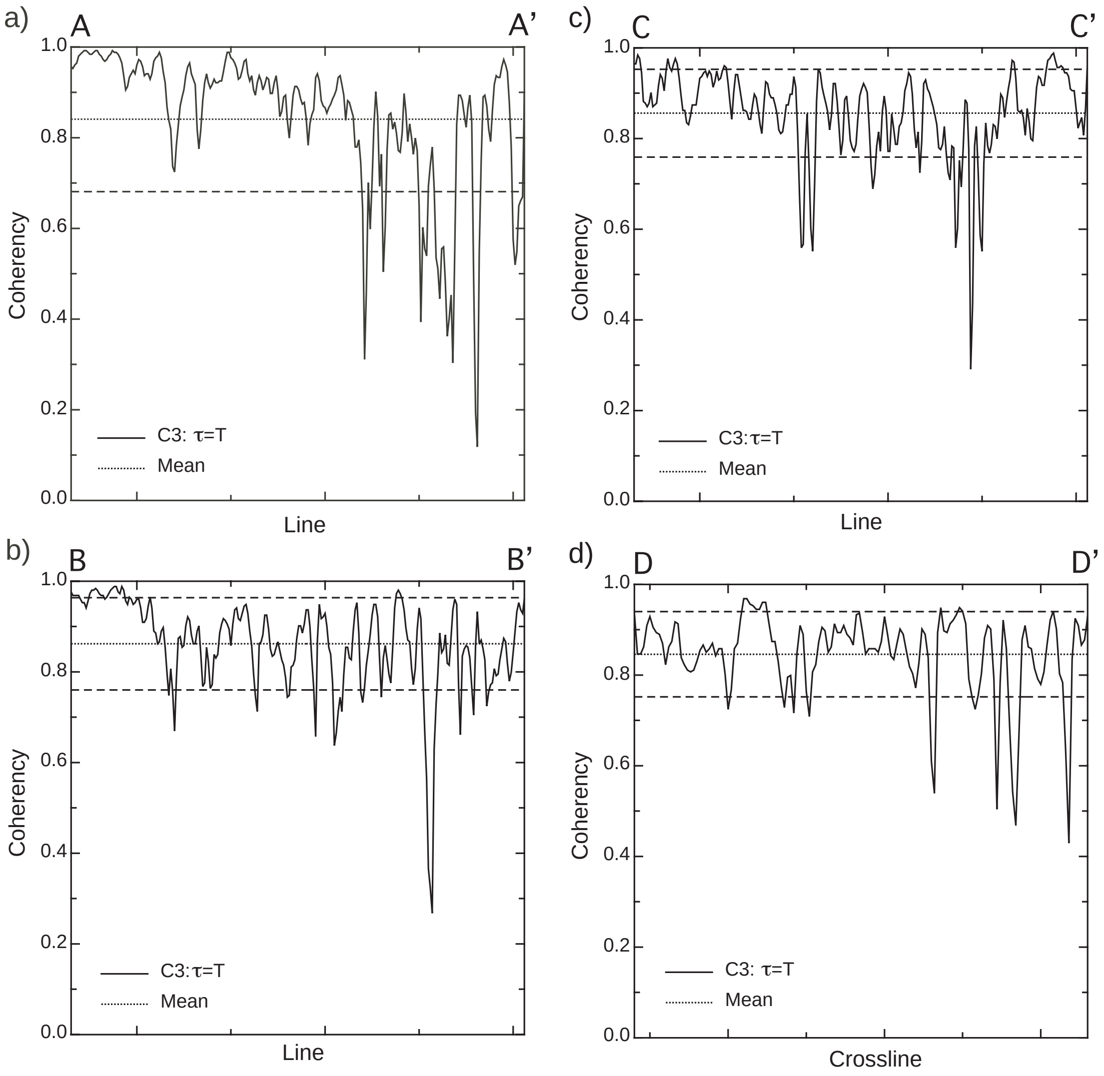

Fig. 5.11. Eigenstructure coherency extraction along a) crossline A b) crossline B c) crossline C d) line D.

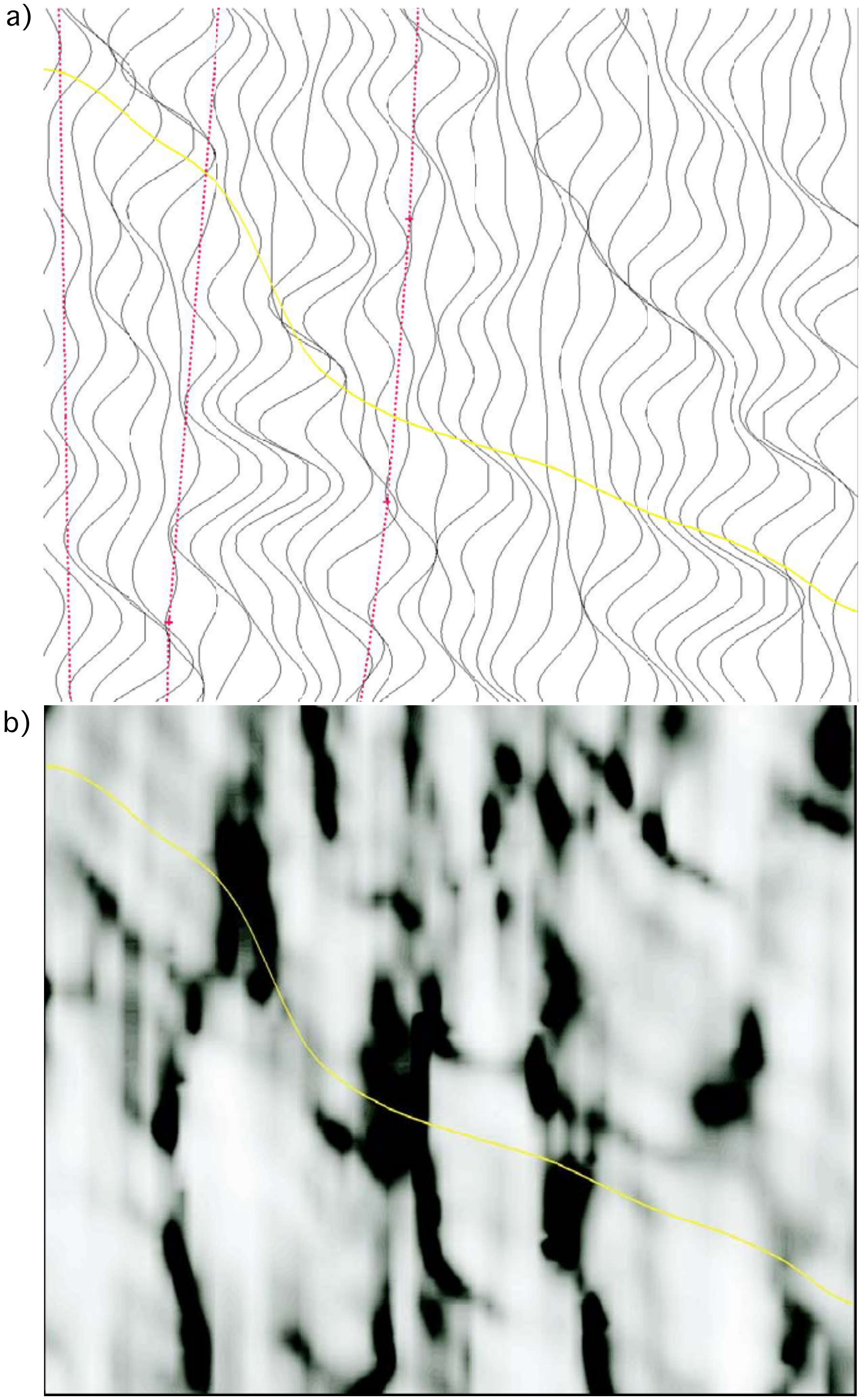

Fig. 5.12. a) Seismic section of the primary deformation zone along crossline A. b) Eigenstructure coherency section for the primary deformation zone along crossline A. The seismic section represents a relative time of 250 ms.

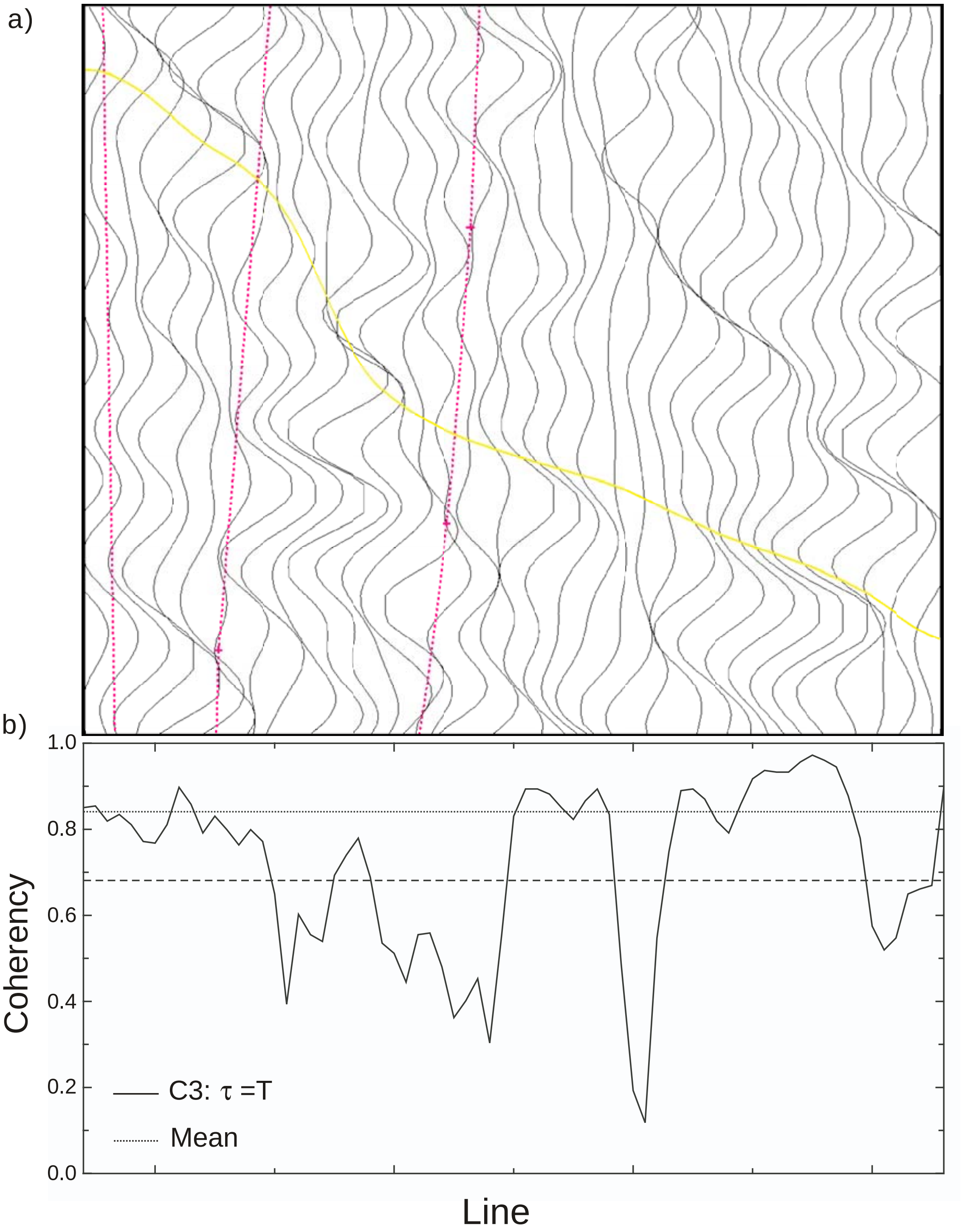

Fig. 5.13. a) Seismic section of the primary deformation zone along crossline A. b) Eigenstructure coherency extraction for the primary deformation zone along crossline A. The seismic section represents a relative time of 250 ms.

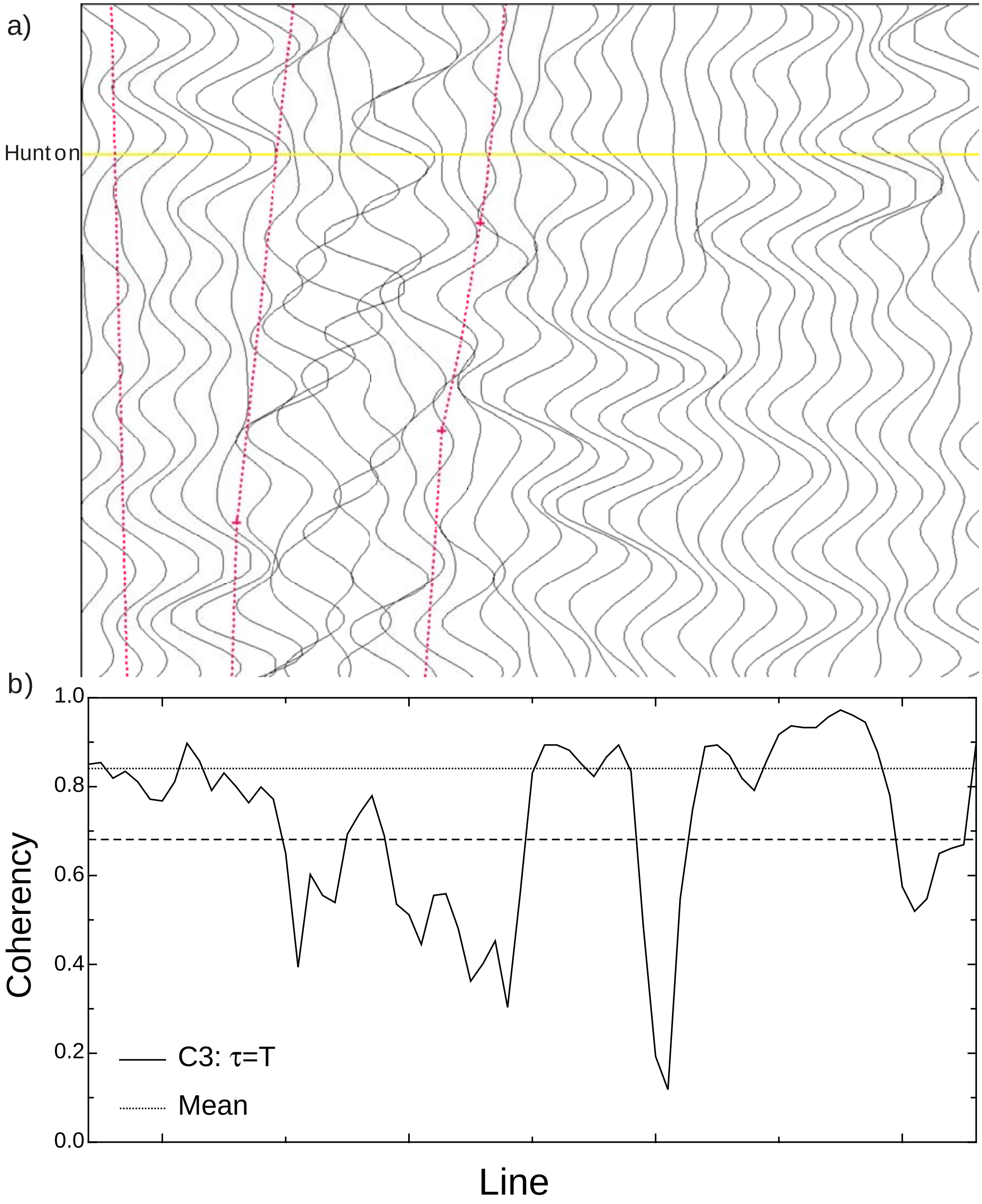

Fig. 5.14. a) Seismic section of the primary deformation zone along crossline A, flattened along the Hunton. b) Eigenstructure coherency extraction for the primary deformation zone along crossline A. The seismic section represents a relative time of 250 ms.

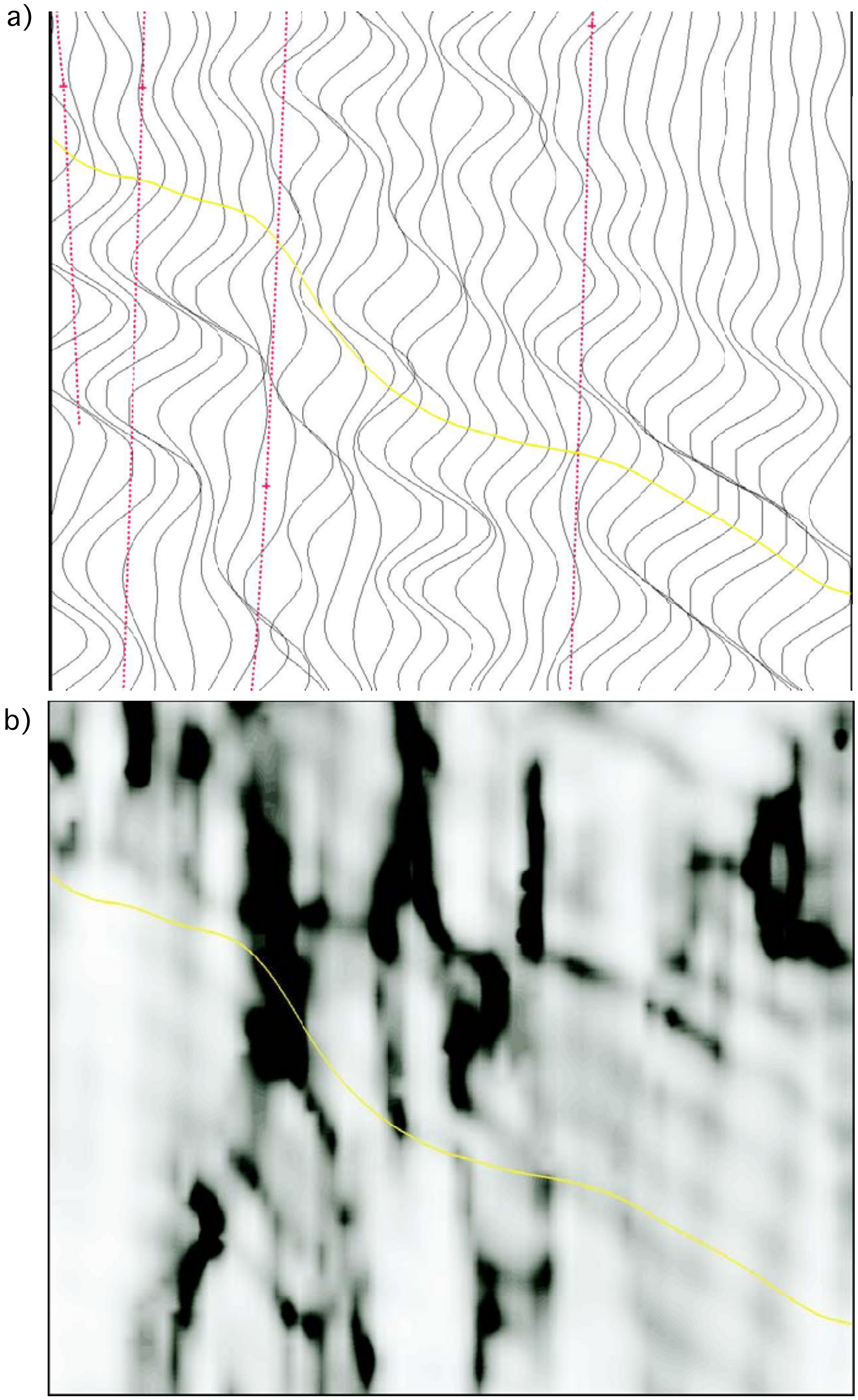

Fig. 5.15. a) Seismic section of the primary deformation zone along crossline B. b) Eigenstructure coherency section for the primary deformation zone along crossline B. The seismic section represents a relative time of 250 ms.

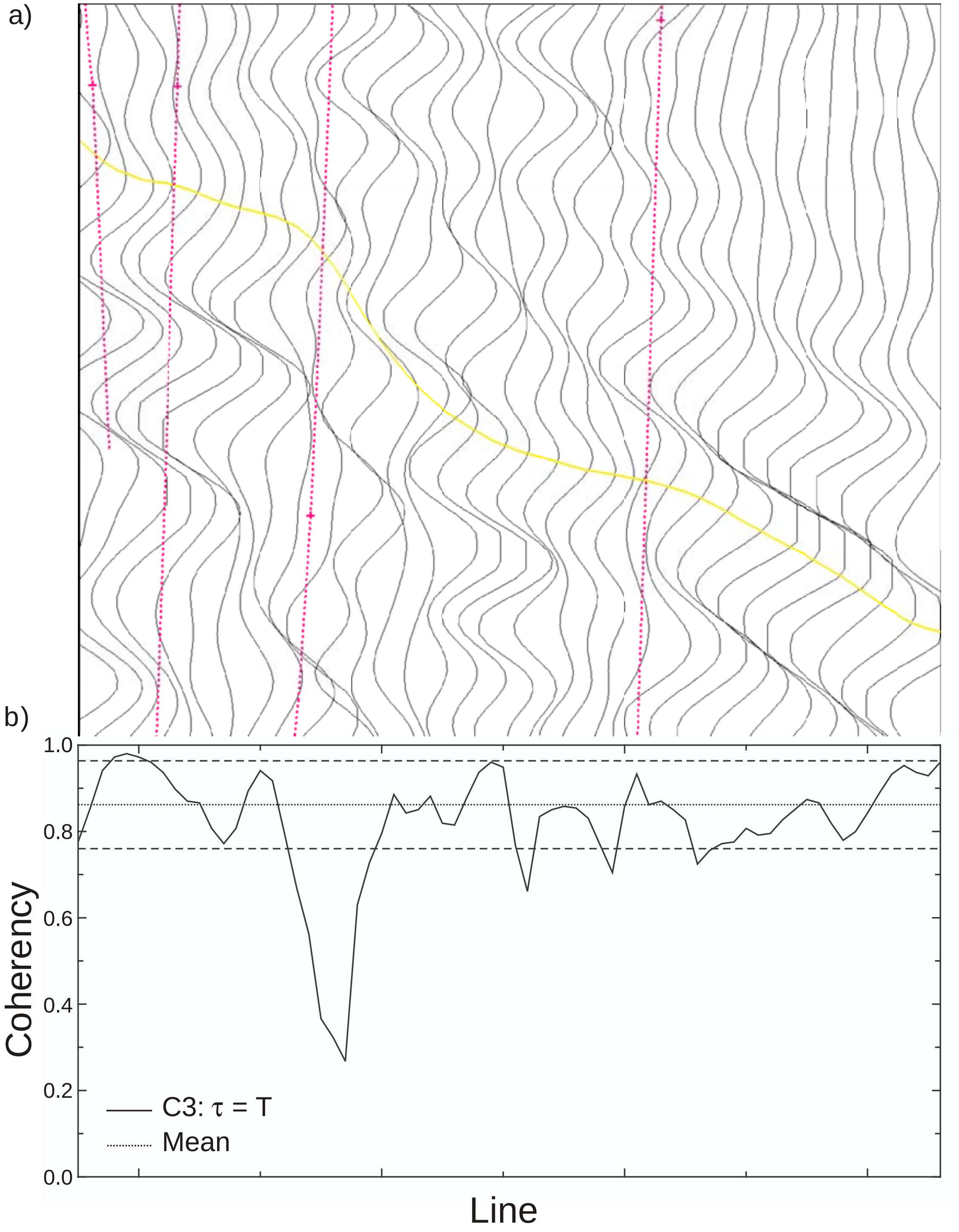

Fig. 5.16. a) Seismic section of the primary deformation zone along crossline B. b) Eigenstructure coherency extraction for the primary deformation zone along crossline B. The seismic section represents a relative time of 250 ms.

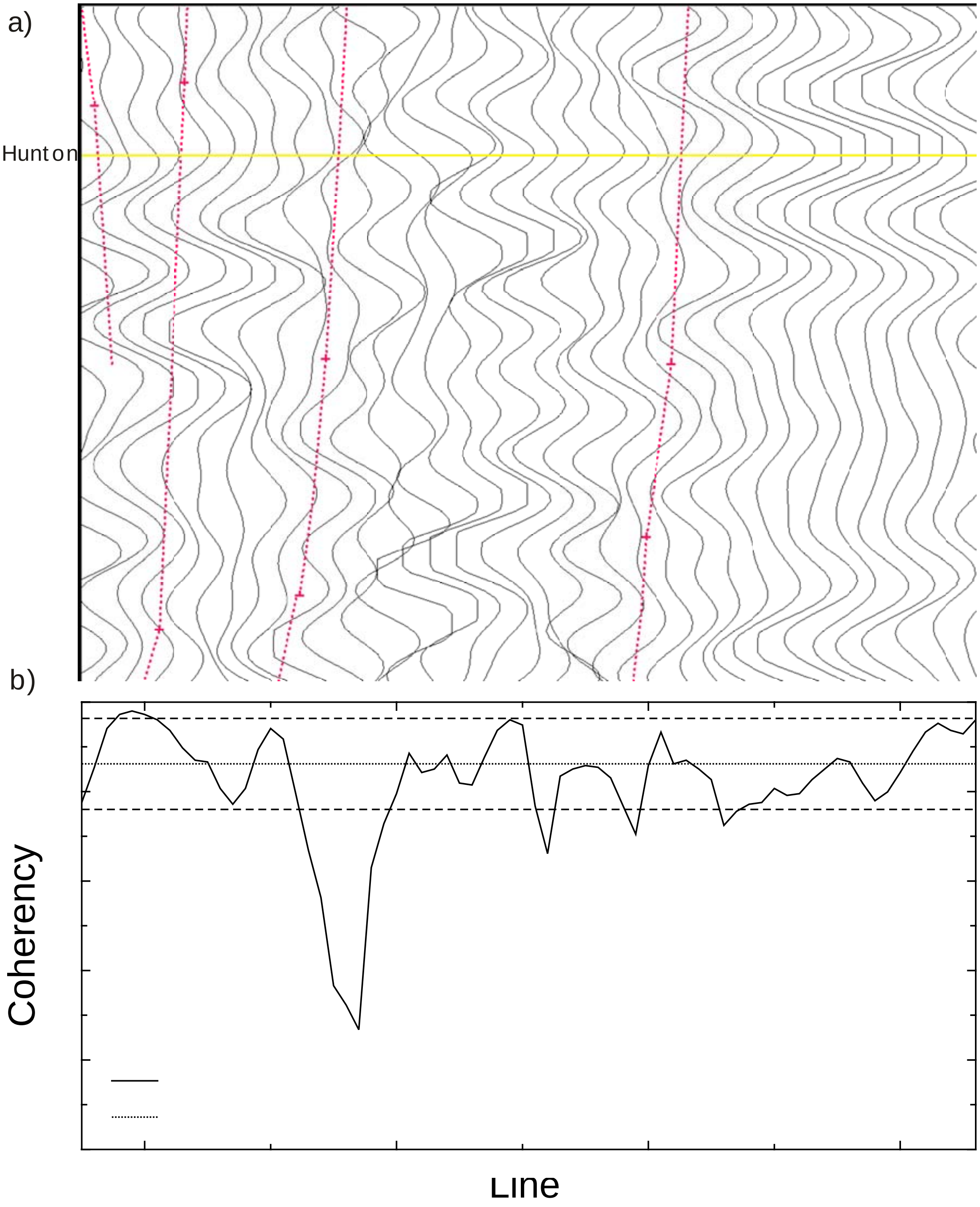

Fig. 5.17. a) Seismic section of the primary deformation zone along crossline B, flattened along the Hunton. b) Eigenstructure coherency extraction for the primary deformation zone along crossline B. The seismic section represents a relative time of 250 ms.

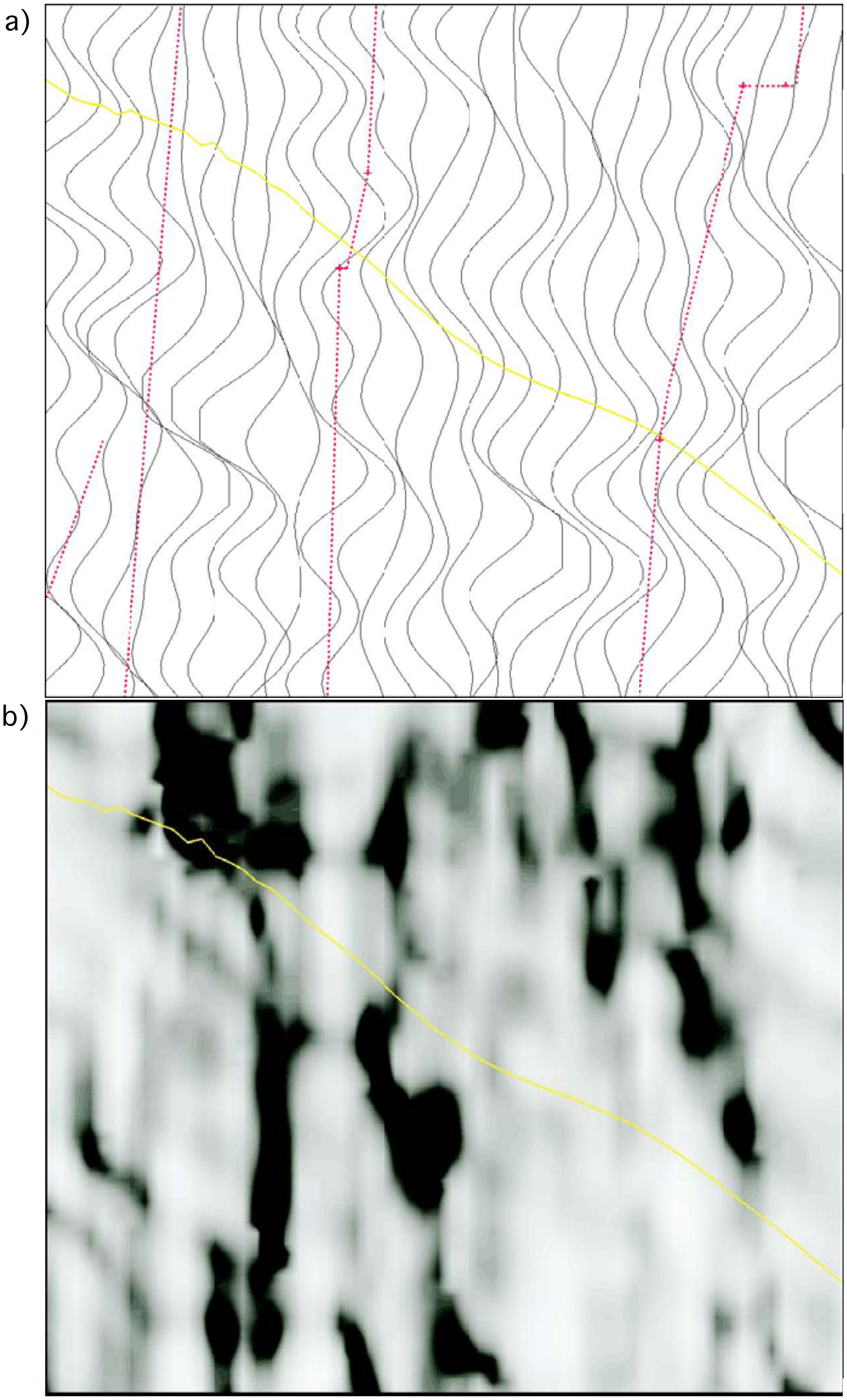

Fig. 5.18. a) Seismic section of the primary deformation zone along crossline C. b) Eigenstructure coherency section for the primary deformation zone along crossline C. The seismic section represents a relative time of 200 ms.

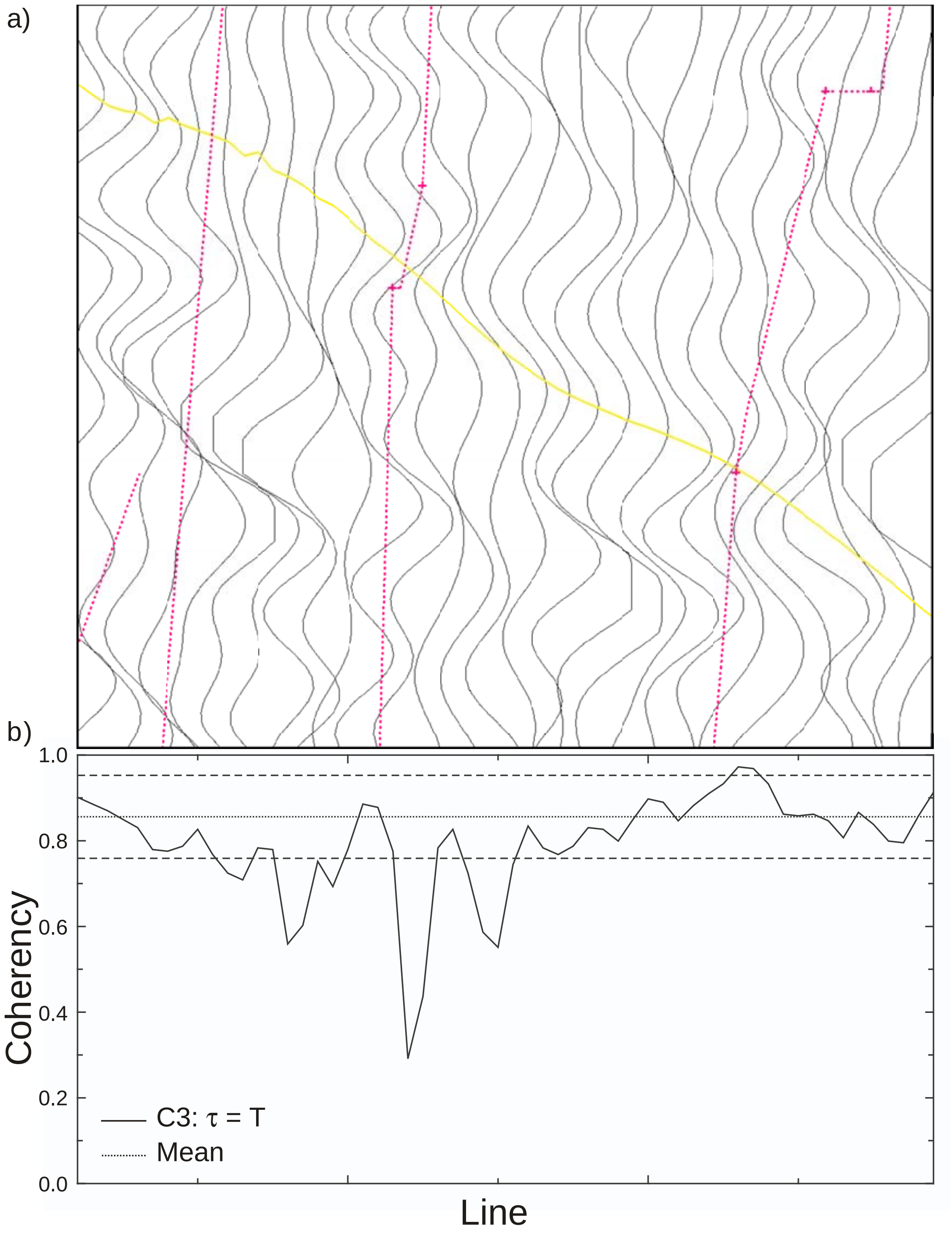

Fig. 5.19. a) Seismic section of the primary deformation zone along crossline C. b) Eigenstructure coherency extraction for the primary deformation zone along crossline C. The seismic section represents a relative time of 200 ms.

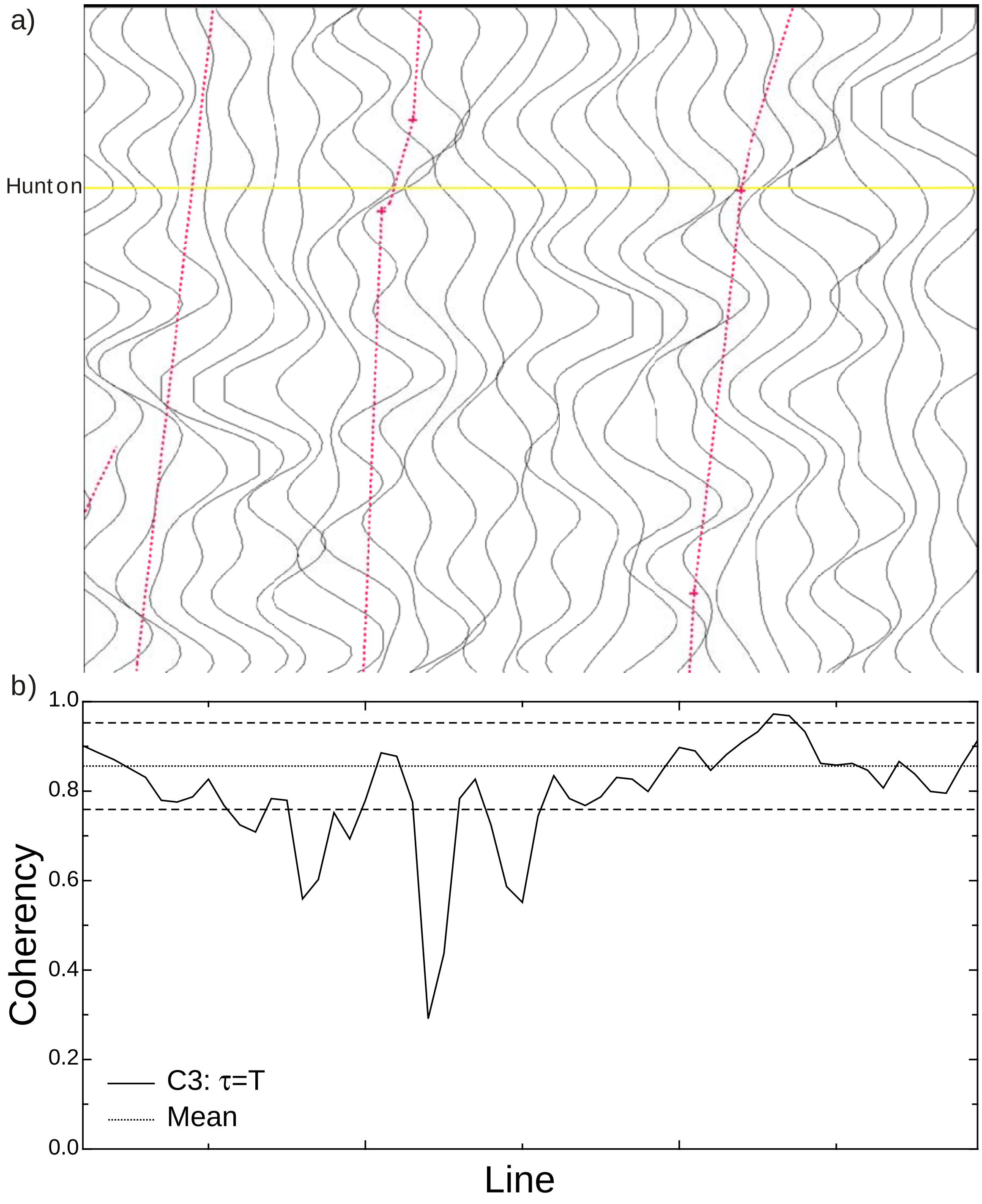

Fig. 5.20. a) Seismic section of the primary deformation zone along crossline C, flattened along the Hunton. b) Eigenstructure coherency extraction for the primary deformation zone along crossline C. The seismic section represents a relative time of 200 ms.

Through an examination of the structural high on the seismic and coherency sections along crossline A (Figure 5.21), vertical offset of reflectors can be associated with linear incoherencies. The trace-to-trace incoherencies along the structural high of crossline A (Figure 5.22) can be better illustrated by flattening the seismic data along the Hunton horizon and comparing the seismic data to a coherency extraction of the same area (Figure 5.23). Many small-scale faults with throw>10 m were interpreted. Crossline B (Figures 5.24, 5.25 & 5.26) and crossline C (Figures 5.27, 5.28 & 5.29) also have similar small-scale faults.

The faults identified from the correlation of the seismic sections and the coherency do not have the same coherency patterns as do the faults within the PDZ. The small-scale faults have incoherencies that do not always extend past the standard deviation range from the mean coherency, making it difficult to distinguish the incoherencies due to geology rather than noise. To determine if the incoherencies are real or noise induced, traditional interpretational methods were used. The incoherent spikes were correlated to subtle amplitude anomalies within the 2-D seismic lines and mapped laterally. Crossline A (Figure 5.23) shows several of the incoherent spike and the associated amplitude anomaly on the 2-D line. Crosslines B (Figure 5.26) and C (Figure 5.29) also show these and other faults. Through correlating coherency spikes to amplitude anomalies on many lines, fault planes were identified and mapped. Many of these faults can also be interpreted using lines. Lines, due to the orientation to the structural regime, were used primarily to identify the strike-slip faults. Line D (Figures 5.30, 5.31 & 5.32) shows several strike-slip faults not easily identified on crosslines A, B and C. Strike-slip faults were difficult to identify because of their low-throw and more coherent nature compared to the reverse faults.

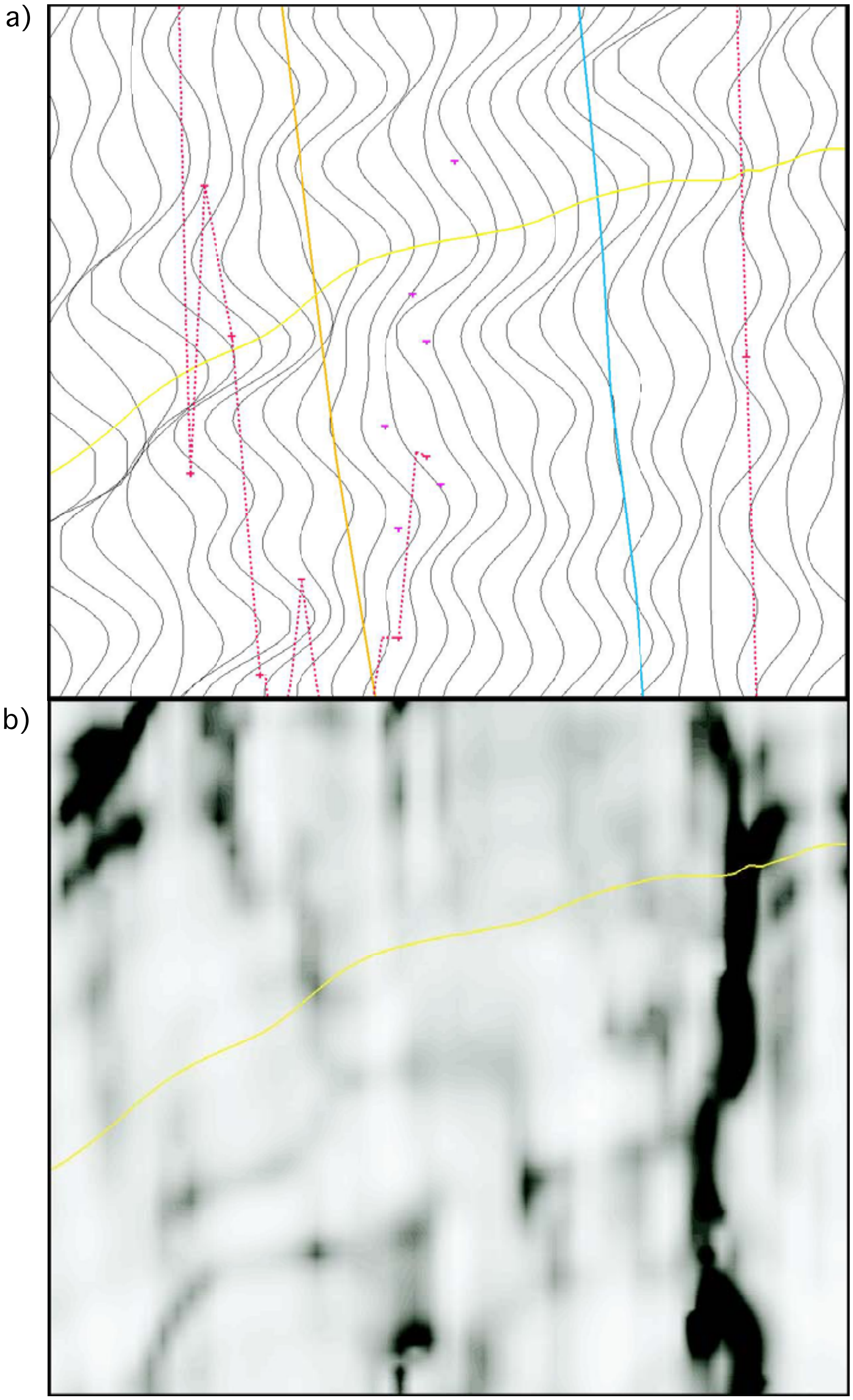

Fig. 5.21. a) Seismic section of the structural high along crossline A. b) Eigenstructure coherency section for the structural high along crossline A. The seismic section represents a time of 250 ms.

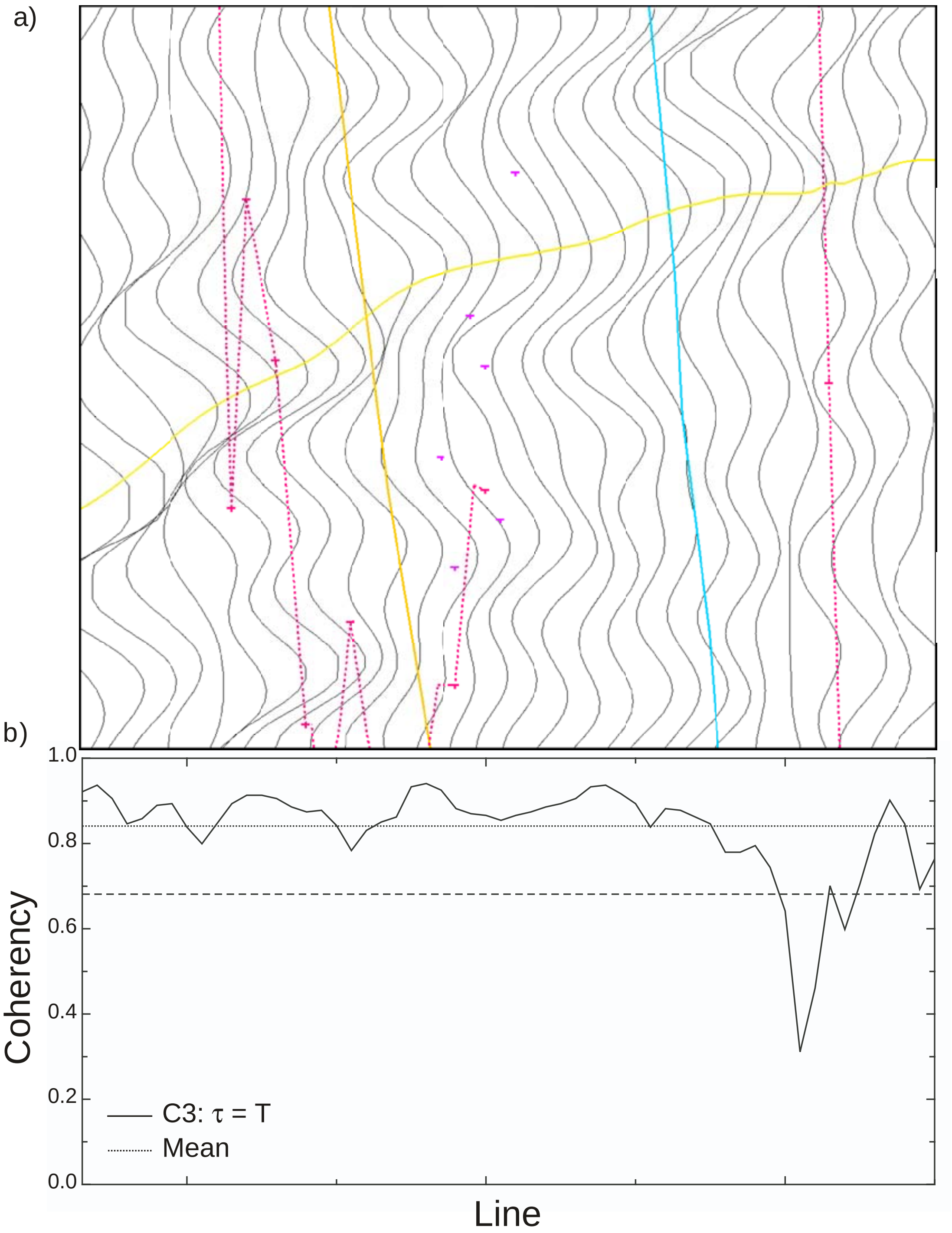

Fig. 5.22. a) Seismic section of the structural high along crossline A. b) Eigenstructure coherency extraction for the structural high along crossline A. The seismic section represents a time of 200 ms.

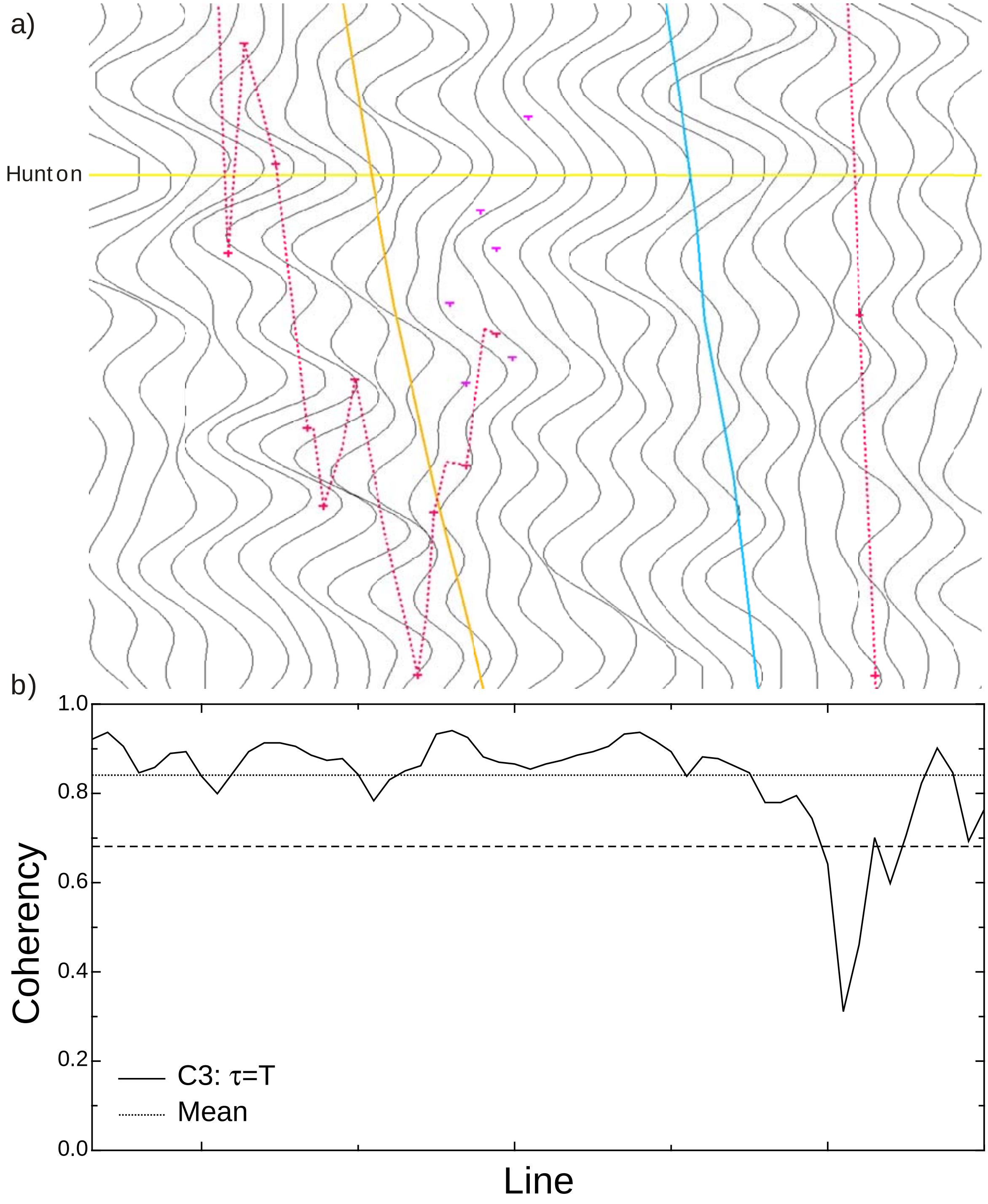

Fig. 5.23. a) Seismic section of the structural high along crossline A, flattened along the Hunton. b) Eigenstructure coherency extraction for the structural high along crossline A. The seismic section represents a relative time of 200 ms.

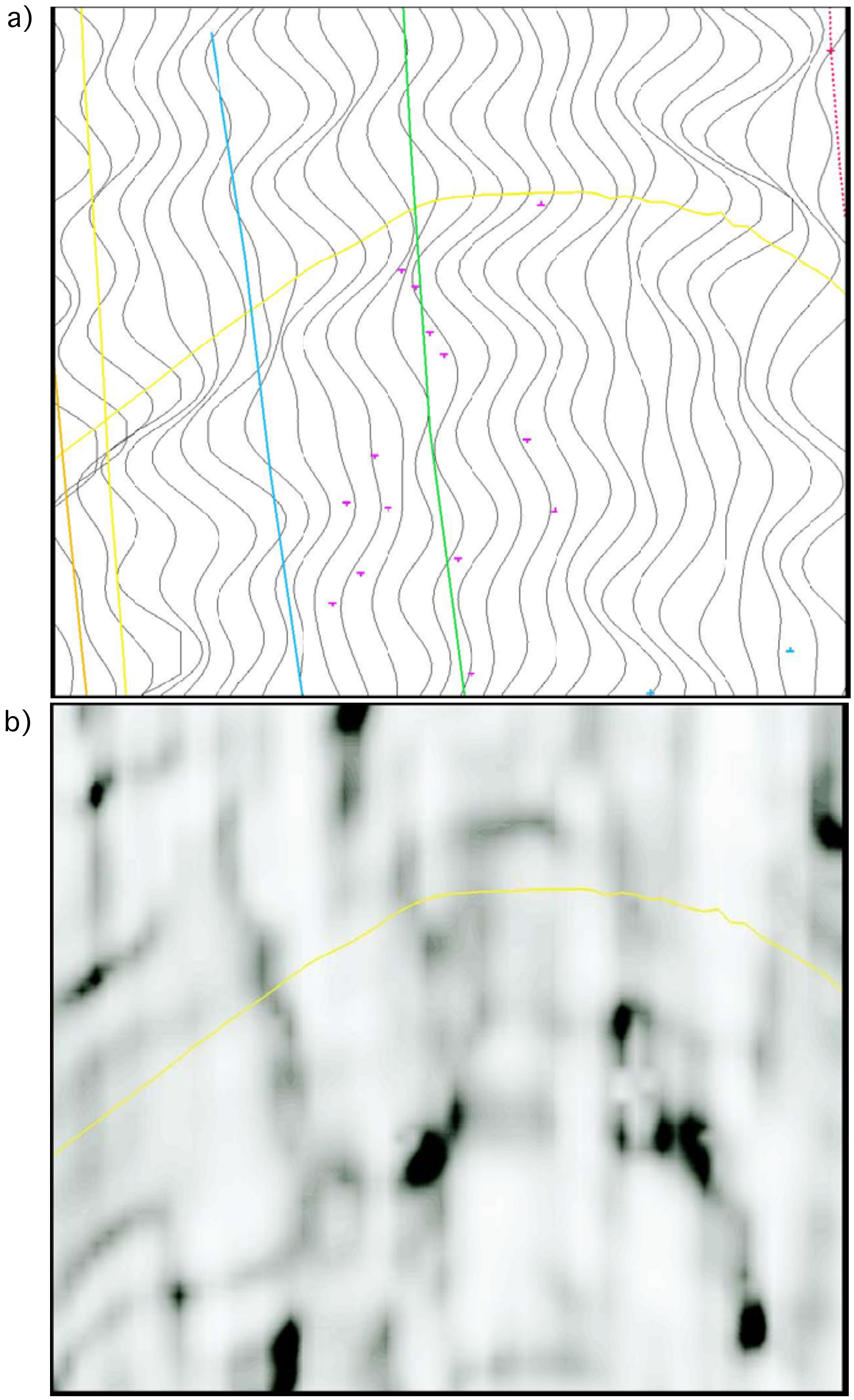

Fig. 5.24. a) Seismic section of the structural high along crossline B. b) Eigenstructure coherency section for the structural high along crossline B. The seismic section represents a time of 250 ms.

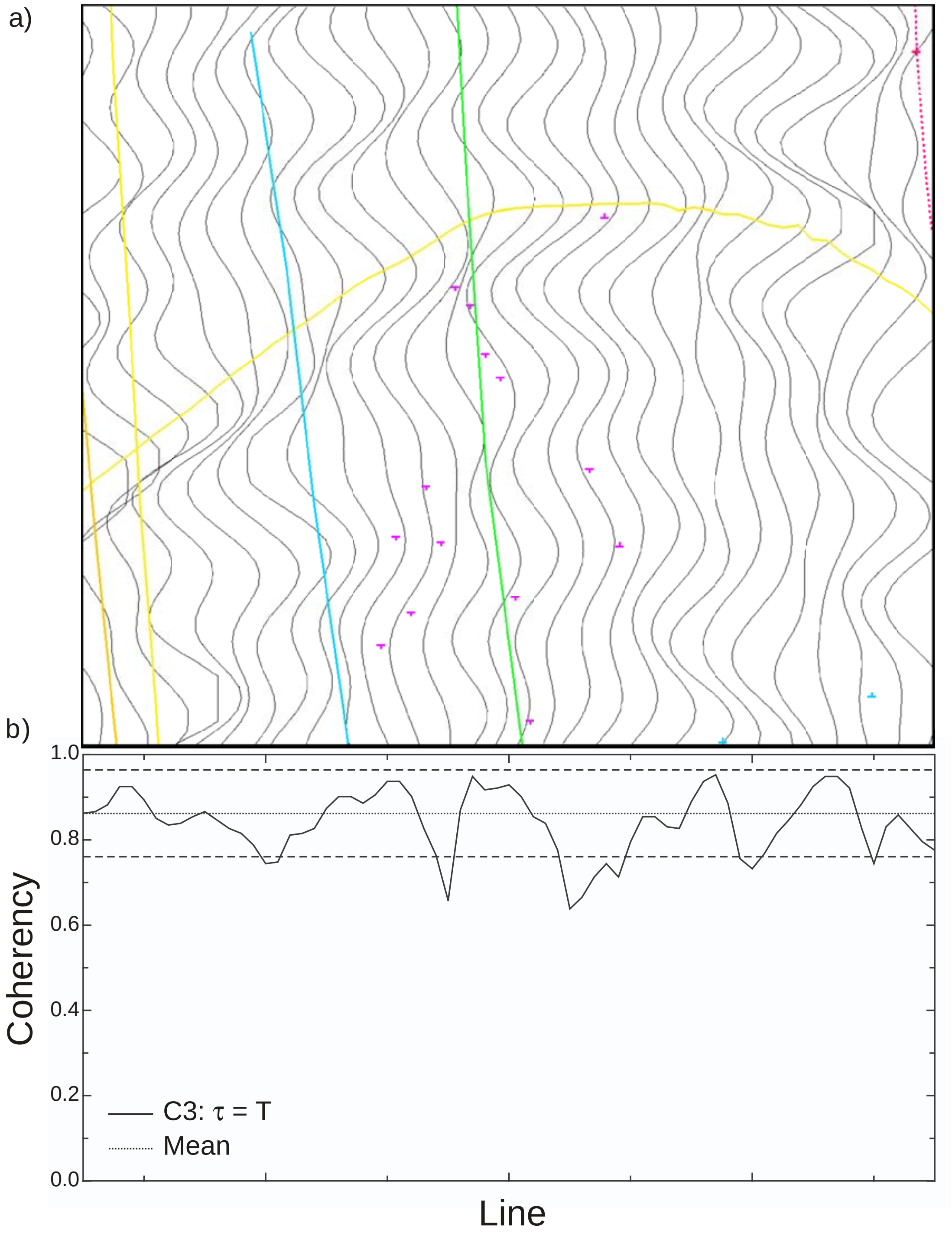

Fig. 5.25. a) Seismic section of the structural high along crossline B. b) Eigenstructure coherency extraction for the structural high along crossline B. The seismic section represents a time of 200 ms.

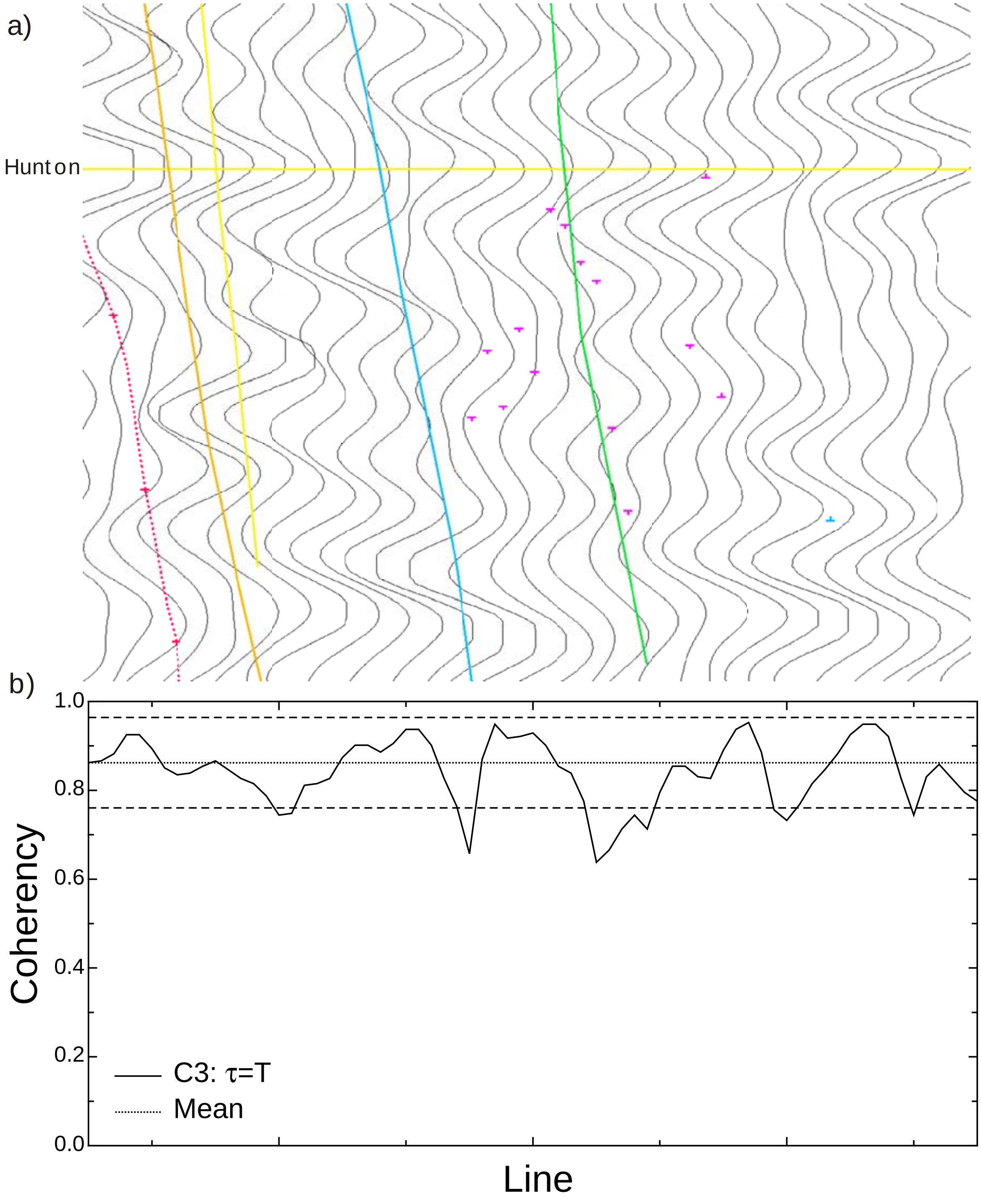

Fig. 5.26. a) Seismic section of the structural high along crossline B, flattened along the Hunton. b) Eigenstructure coherency extraction for the structural high along crossline B. The seismic section represents a relative time of 200 ms.

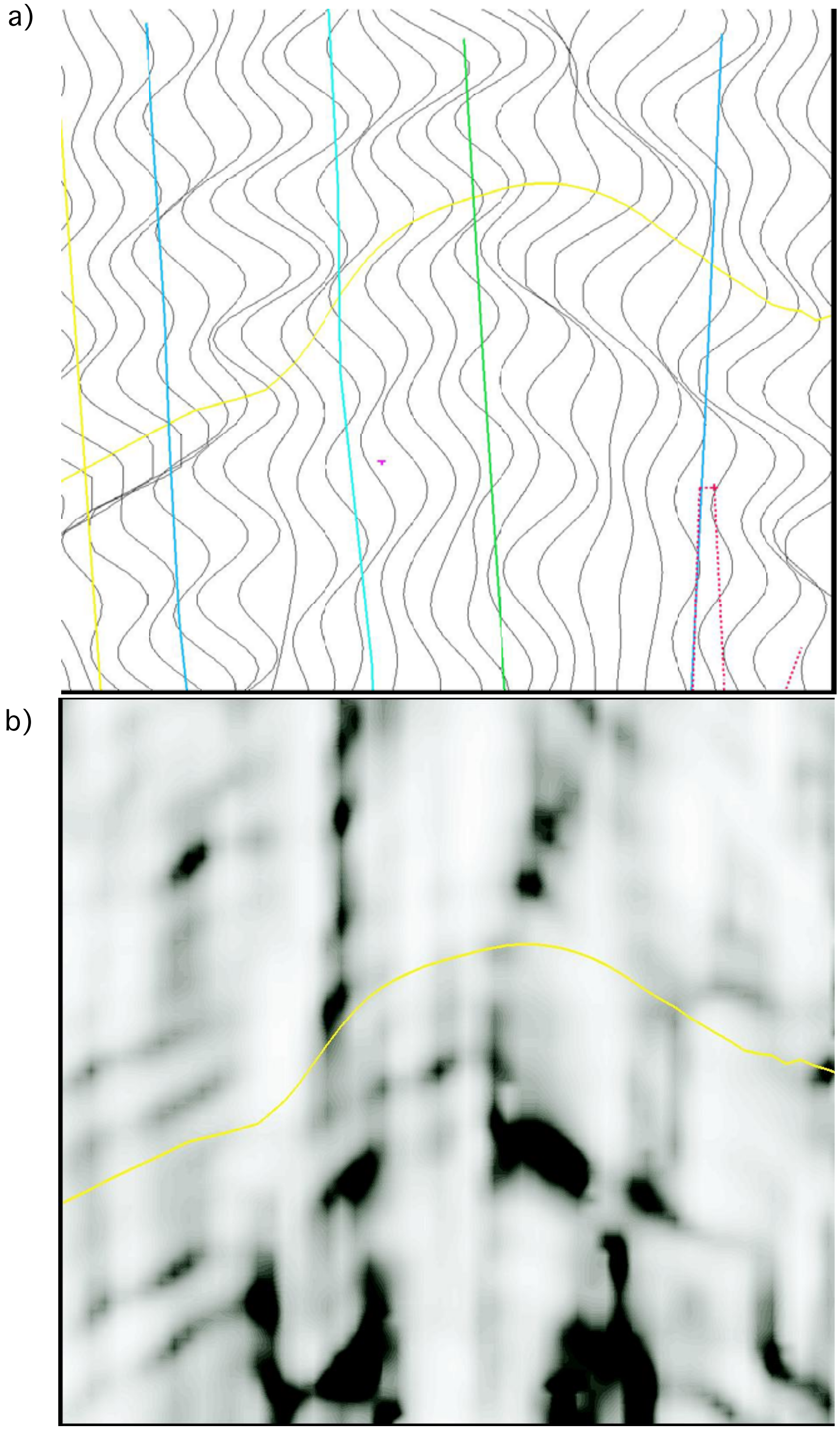

Fig. 5.27. a) Seismic section of the structural high along crossline C. b) Eigenstructure coherency section for the structural high along crossline C. The seismic section represents a time of 200 ms.

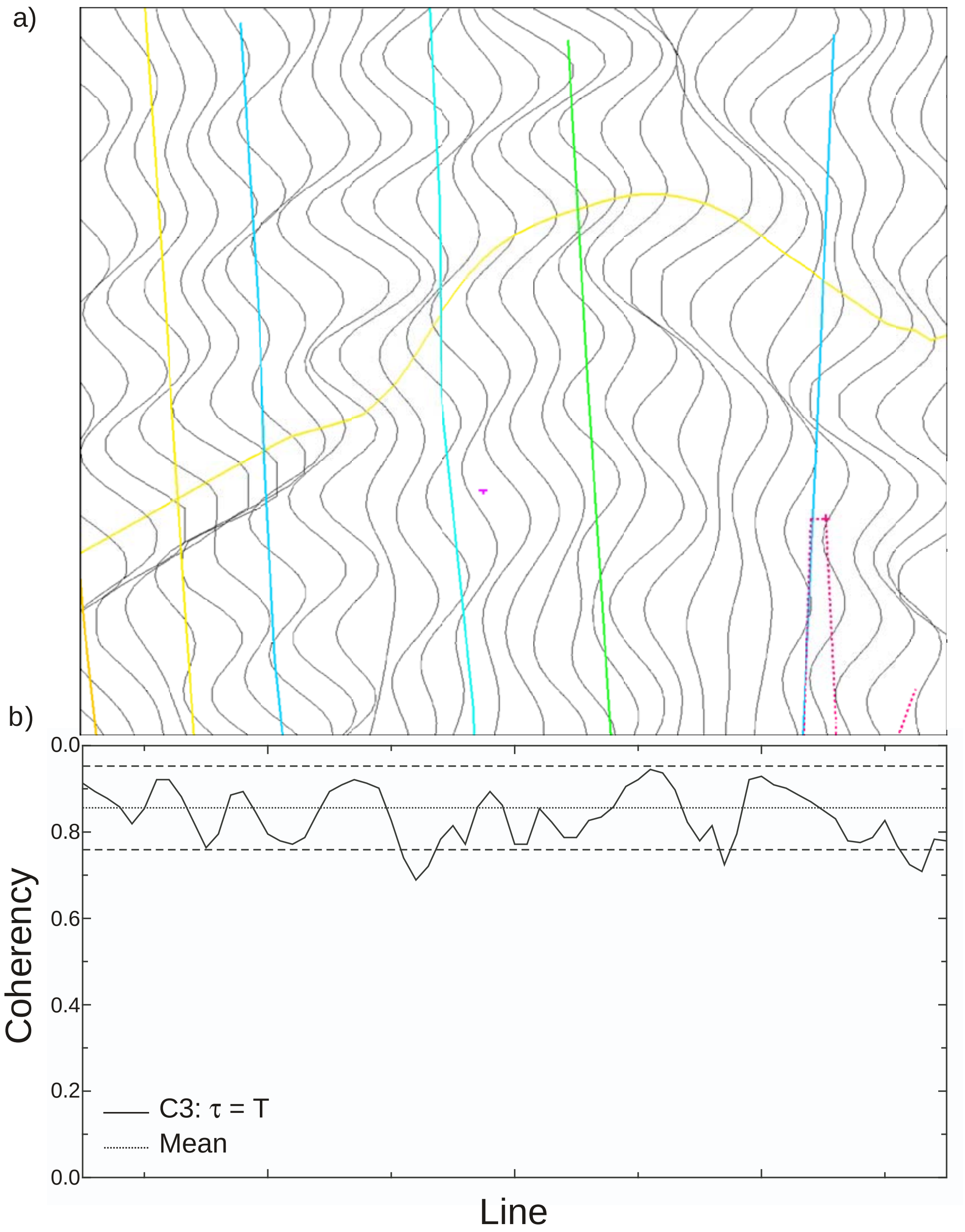

Fig. 5.28. a) Seismic section of the structural high along crossline C. b) Eigenstructure coherency extraction for the structural high along crossline C. The seismic section represents a time of 200 ms.

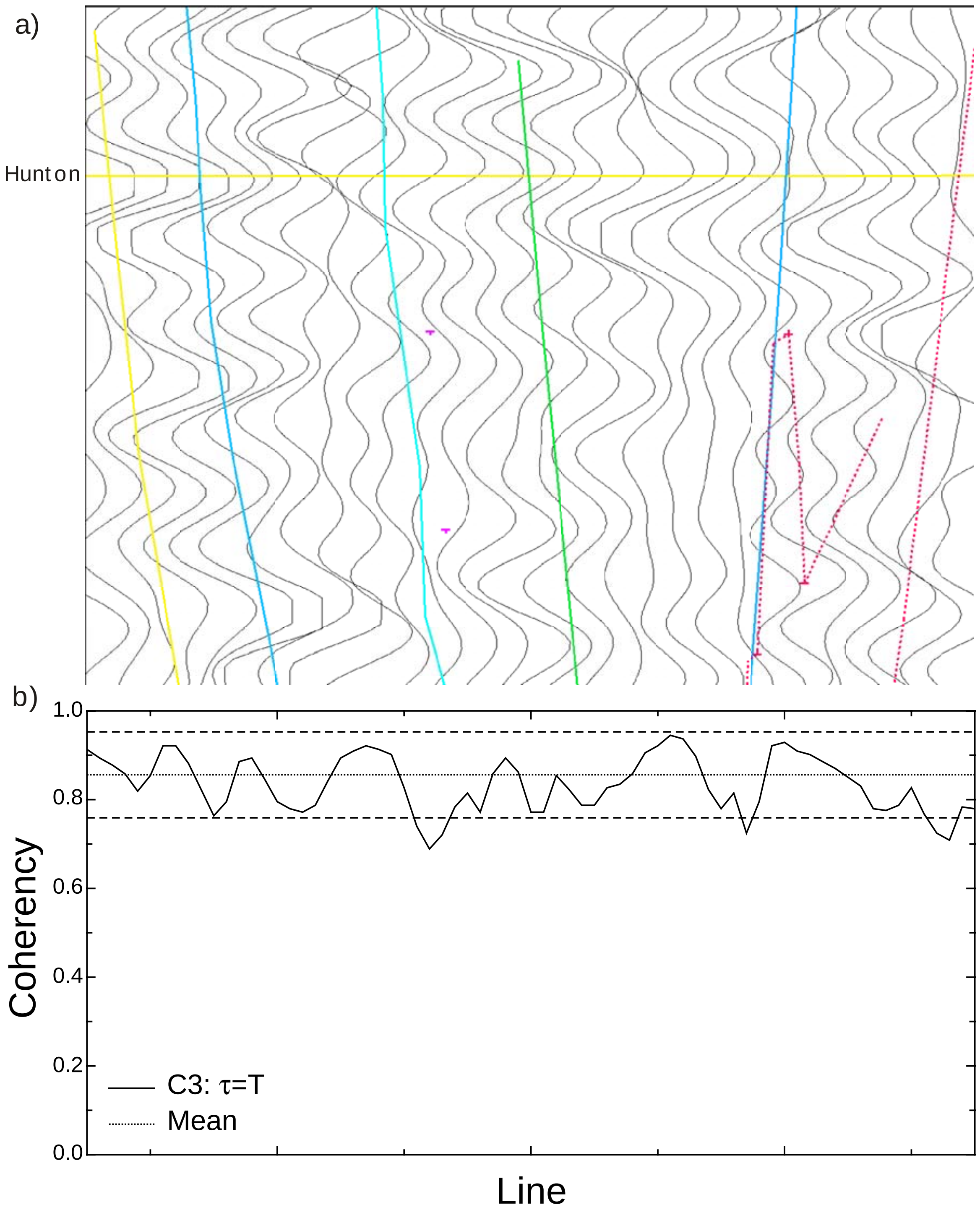

Fig. 5.29. a) Seismic section of the structural high along crossline C, flattened along the Hunton. b) Eigenstructure coherency extraction for the structural high along crossline C. The seismic section represents a relative time of 200 ms.

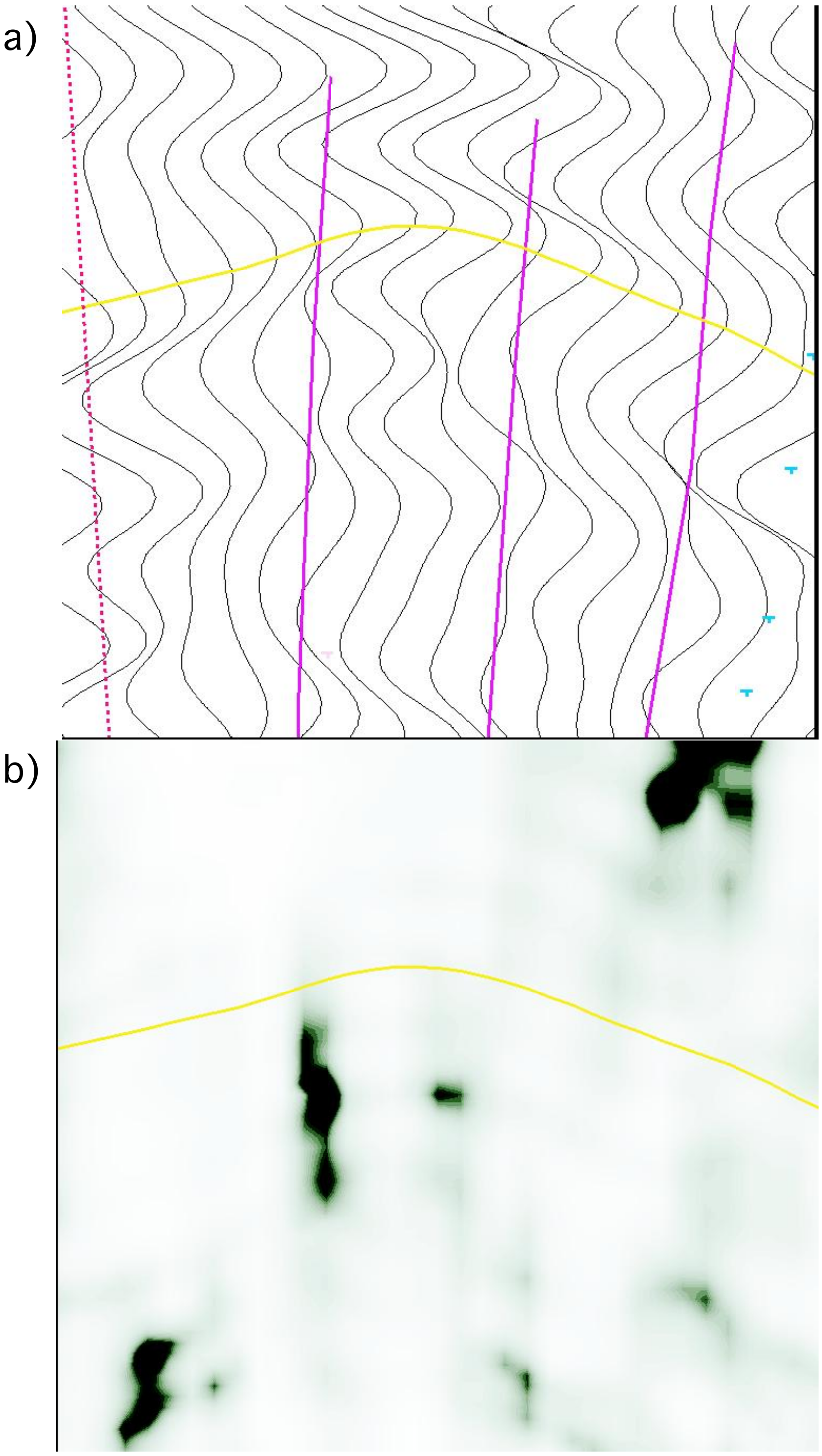

Fig. 5.30. a) Seismic section of the structural high along crossline D. b) Eigenstructure coherency section for the structural high along crossline D. The seismic section represents a time of 250 ms.

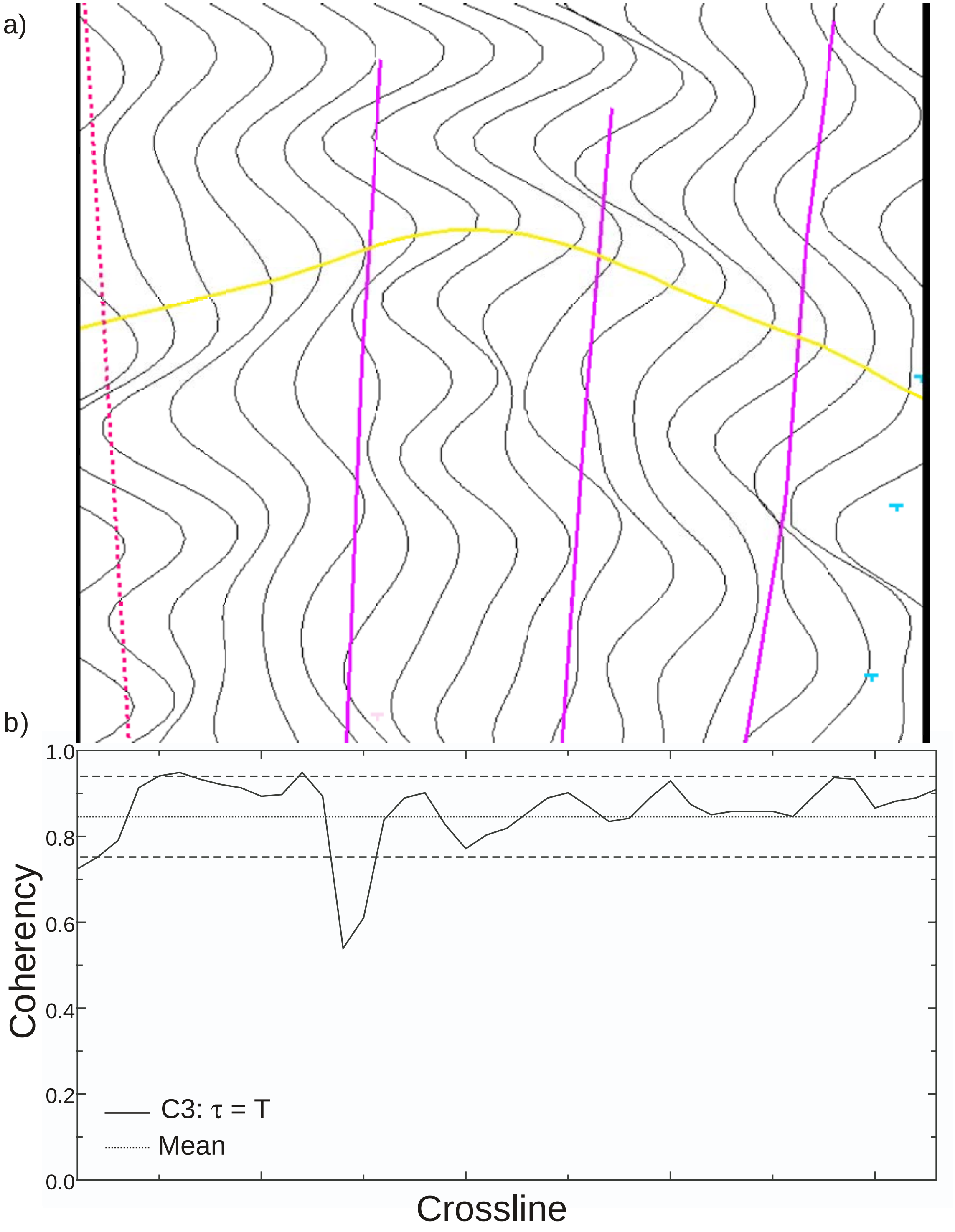

Fig. 5.31. a) Seismic section of the structural high along crossline D. b) Eigenstructure coherency extraction for the structural high along crossline D. The seismic section represents a time of 250 ms.

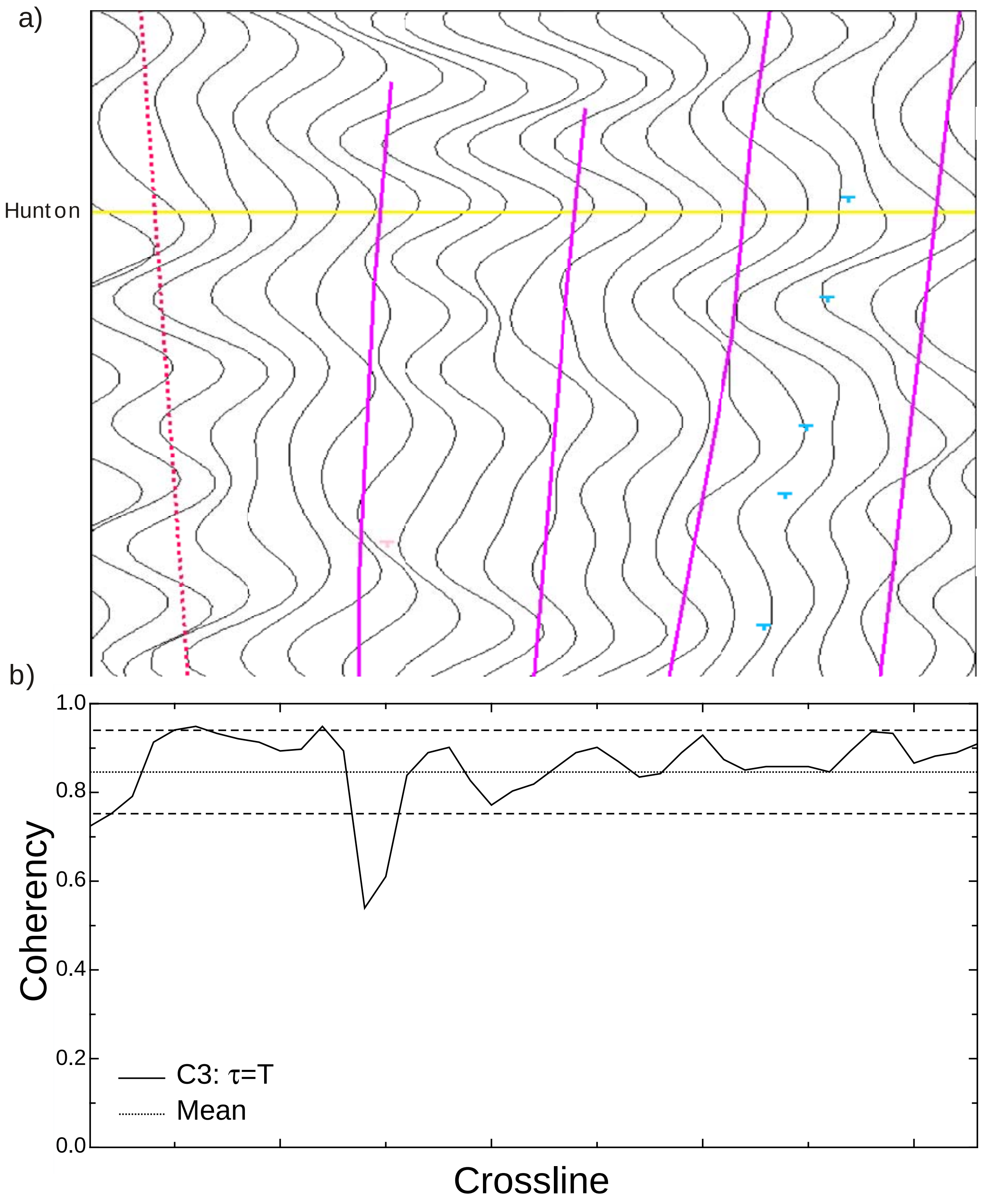

Fig. 5.32. a) Seismic section of the structural high along line D, flattened along the Hunton. b) Eigenstructure coherency extraction for the structural high along line D. The seismic section represents a relative time of 250 ms.

The structural interpretation of the Hunton (Figure 5.33) was shown to be dominated by a main reverse fault system (faults trending NW-SE). These faults were offset by many strike-slip faults (faults trending NE-SW). The red faults within Figure 5.33 are interpreted as the large-scale faults, easily identified using traditional interpretation methods. The pink faults are the small-scale strike-slip faults on the structural high. The other faults correspond to small-scale reverse faults on the structural high. The throw of the small-scale faults on the structural high was determined to have a magnitude greater than 10 m. These throw values were estimated according to the coherency limitations identified by this research. The exact throw of the faults is not known and can not easily be determined without core data. Based upon the large-scale faults identified within the area, the strike-slip faults have very little throw while the reverse faults have a larger, but undeterminable throw. These faults are expected to be present because they fit the local and regional trend. They are also on the structural high, which should have many fractures due to the folding and tectonics that occurred during the Mississippian-Pennsylvanian time. Future considerations for hydrocarbon production should consider the faults that have been identified and mapped on the structural high of the Hunton Group. These faults have small throw (compared to the regional fault system) and could enhance production considerably if a well is positioned properly.

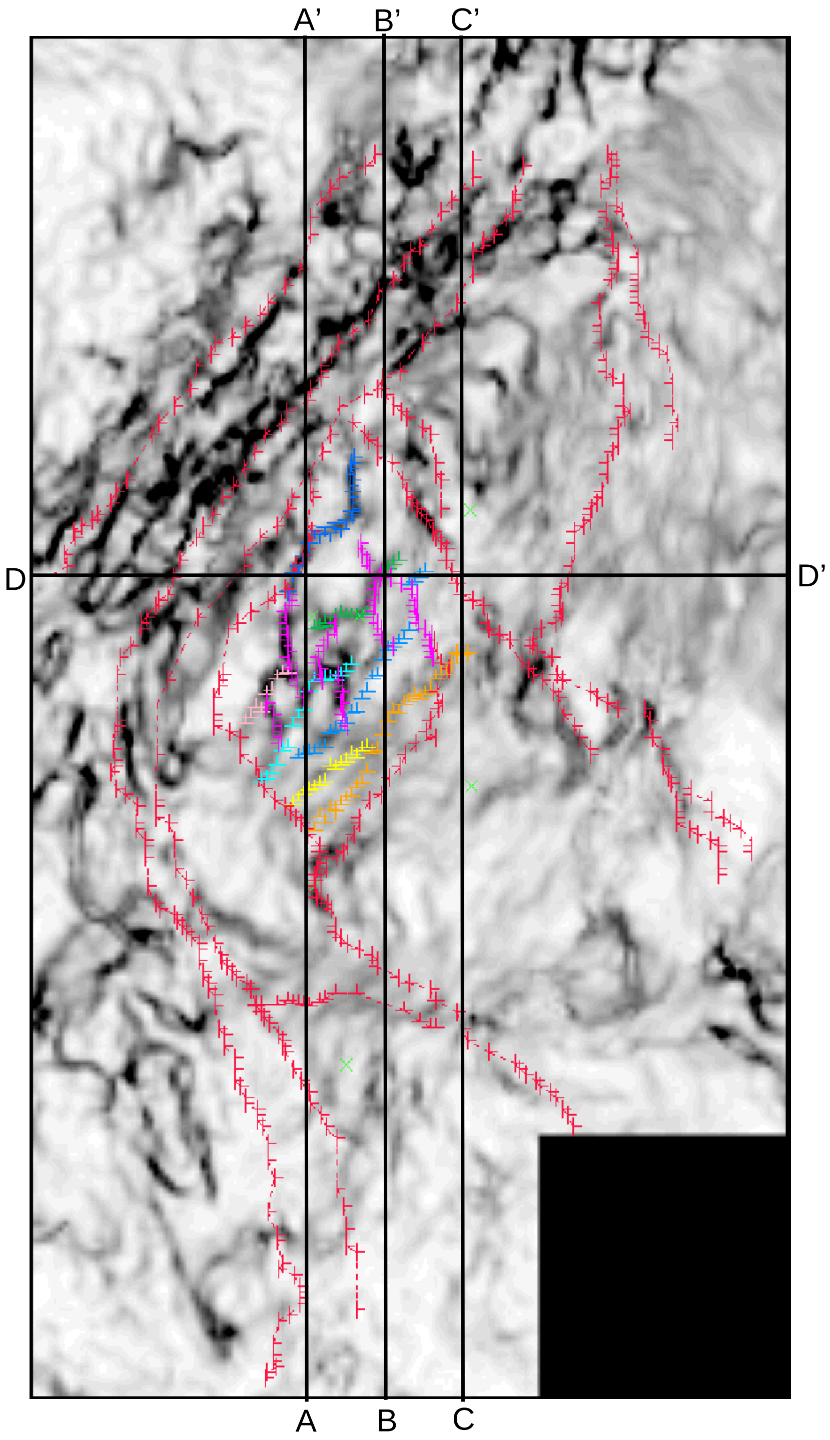

Fig. 5.33. Structural interpretation of reverse and strike-slip faults on the horizon of interest. Faults in red are large-scale and easily identified on the seismic sections. The multi-colored faults in the center of the map are small-scale and interpreted through the coherency analysis.

CHAPTER VI

CONCLUSIONS

Coherency has been used to quickly outline and identify the structural settings of synthetic and field data sets. The analytical and geophysical methods used to explore the limitations of coherency at identifying small-scale faults proved successful. Data sets with various frequencies and signal-to-noise ratios were used to set the limits to which faults can be imaged by coherency.

The temporal window length was found to be sensitive to the signal-to-noise ratio. An increase in the temporal window length was shown to correspond to a decrease of coherency within low signal-to-noise data sets. These findings are contrary to other published works (Bahorich et al., 1995) and provide evidence that poor quality data sets can be imaged and investigated by adjusting the processing parameters to fit the interpretation objectives.

The limits to which a fault can identified depended upon the quality and parameters of the data set. A fault can be identified by coherency as long as the traveltime-to-period ratio is greater than 10% or the throw-to-wavelength is greater than 5%. These parameters hold true as long as the signal-to-noise ratio was above 3. The findings of this research also suggest that one might be able to detect a geophysical feature that might be less than one sample interval in time or thickness. Coherency might then be able to image features that are thought to be below seismic resolution.

Although coherency has the ability to detect small scale faults, interpretation is most accurate when coherency is used in conjunction with traditional mapping techniques. Through associating subtle amplitude features on 2D seismic line with the coherency across this feature, the distinction between noise and geology can be determined more accurately.

The Hunton Group was mapped locally using the coherency technique outlined in this paper. Small-scale faults that were initially overlooked as noise were identified. The fault's orientations fit the regional setting of the Anadarko Basin and can provide future consideration to ConocoPhillips Inc. These results indicate that data sets with poor signal-to-noise ratios can be interpreted with some certainty, possibly changing the methods for which one interprets poor quality seismic data, such as sub-salt environments.

Future work can deal with including dipping reflectors, dipping faults and heterogeneous layers within the geophysical model. A larger variety of frequencies and smaller signal-to-noise ratios could also be used to better understand the limitations of coherency modeling. The stratigraphic implementations of coherency could also be investigated by using the same methods employed here and also the affects of adjusting the spatial sampling parameter within the coherency processing stage. Furthermore, the ability for coherency to distinguish processing artifacts from reflectors or noise will be an important topic in the future.

REFERENCES

Al-Shaieb, Z., and Puckette, J., 2001, The Hunton Group: Sequence stratigraphy, facies, dolomitization, and karstification, *in* Johnson, K. S., Ed., Oklahoma Geological Survey, Circular 105: Oklahoma Geological Survey, 17–29.

Amsden, T. W., 1975, Hunton Group (Late Ordovician, Silurian, and Early Devonian) in the Anadarko Basin of Oklahoma: Oklahoma Geological Survey, Bulletin 122: Oklahoma Geological Survey.

Bahorich, M. S., and Farmer, S. L., 1995, 3-D seismic discontinuity for faults and stratigraphic feature: The coherence cube: The Leading Edge, **14**, 1053–1058.

Blubaugh, P. E., 1999, Hydrodynamics of the Hunton Group Anadarko Basin, Oklahoma and Texas Panhandle, pt. 1: Shale Shaker, **49**, 61–80.

Gersztenkorn, A., and Marfurt, K. J., 1999, Eigenstructure-based coherence computations as an aid to 3-D structural and stratigraphic mapping: Geophysics, **64**, 1468–1479.

Johnson, K. S., 1989a, Geological Evolution of the Anadarko Basin, Anadarko Basin Symposium, 1988, *in* Johnson, K. S., Ed., Oklahoma Geological Survey, Circular 90: Oklahoma Geological Survey, 3–12.

——— 1989b, Geology of the Southern Midcontinent, *in* Johnson, K. S., Ed., Special Publication 89-2: Oklahoma Geological Survey, 12–20.

Lawrence, P., 1988, Seismic attributes in the characterization of small-scall reservoir faults in Abqaiq Field: The Leading Edge, **7**, 521–525.

Li, Y., Downton, J., and Goodway, B., 2003, Recent application of AVO to carbonate reservoirs in the Western Canadian Sedimentary Basin: The Leading Edge, **22**, 670–674.

Mandal, B., and Mitchel, B. J., 1986, Complete seismogram synthesis for transversely isotropic media: Geophysics, **59**, 149–156.

Marfurt, K. J., and Lynn, R. L., 2000, 3-D broad-band estimates of reflector dip and amplitude: Geophysics, **65**, 304–320.

Marfurt, K. J., Lynn, R. L., Farmer, S., and Bahorich, M. S., 1998, 3-D seismic attributes using a semblance-based coherency algorithm: Geophysics, **63**, 1150–1165.

Marfurt, K. J., Sudhaker, V., Gersztenkorn, A., Crawford, K. D., and Nissen, S. E., 1999, Coherency calculations in the presence of structural dip: Geophysics, **64**, 104–111.

Morgan, W. A., 1982, Silurian reservoirs in upward-shoaling cycles of the Hunton Group, Mt. Everette and Southwest Reeding Fields, Kingfisher County, Oklahoma: Phillips Petroleum Co.

Neves, F. A., Al-Marzoug, A., Kim, J. J., and Nebrija, E. L., 2003, Fracture characterization of deep tight gas sands using Azimuthal Velocity and AVO seismic data in Saudi Arabia: The Leading Edge, **22**, 469–475.

Perry, W. J., 1987, Tectonic evolution of the Anadarko Basin Region, Oklahoma, *in* Perry, W. J., Ed., U.S. Geological Survey Bulletin 1899-A: US Geological Survey, A1–A19.

Peyton, L., Bottjer, R., and Partyka, G., 1998, Interpretation of incised valleys using new 3-D seismic techniques: A case history using spectral decomposition and coherency: The Leading Edge, **17**, 1294–1298.

Pippin, L., 1968, Panhandle-Hugoton Field, Texas-Oklahoma-Kansas: The First Fifty Years: Phillips Petroleum Co.

Shen, F., Zhu, X., and Toksoz, N. M., 2002, Effects of fractures on NMO velocities and P-wave Azimuthal AVO response: Geophysics, **67**, 711–725.

Sheriff, R. E., and Geldart, L. P., 1995, Exploration Seismology: Cambridge University Press.

Skirius, C., Nissen, S., Haskell, N., Marfurt, K., Hadley, S., Ternes, D., Michel, K., Regular, I., D'Amico, D., Deliencourt, F., Romero, T., D'Angelo, R., and Brown, B., 1999, 3-D seismic attributes applied to carbonates: The Leading Edge, **18**, 384–393.

Wigger, S., Bailey, J., Larson, M., and Wallace, M., 1997, Ha'py Field: A Pliocene bright spot example from the Nile Delta, Egypt: The Leading Edge, **16**, 1827–1829.

VITA

David Benjamin Barnett

Permanent address

46 Underwood St.
Belchertown, MA 01007
979-218-5569

Education

M.S., May 2005, Texas A&M University, Department of Geology and Geophysics. Major: Geophysics.

M.S., August 2002, Wright State University, Department of Geology. Major: Hydrogeology

B.S., June 2000, Union College, Department of Geology. Major: Geology.